Electronic transport studies of highly-polarized compensated ferrimagnetic thin films: Mn_2Ru_xGa

Ajay Kumar Jha

School of Physics

University of Dublin

A thesis submitted in part-fulfillment of the requirements for the degree of

Doctor of Philosophy

February 2022

Declaration

This thesis is submitted by the undersigned for examination for the degree of *Doctor of Philosophy* at the University of Dublin. I declare that this thesis has not been submitted as an exercise for a degree at this or any other university. It is entirely my own work, apart from the joint effort mentioned in the acknowledgements and in the text.

I agree to deposit this thesis in the University's open access institutional repository or allow the library to do so on my behalf, subject to Irish Copyright Legislation and Trinity College Library conditions of use and acknowledgement.

Ajay Kumar Jha

Dedicated to: My parents and friends...

Acknowledgements

This thesis would not have been possible without the constant help, guidance, and endless patience of many individuals. So, this is the moment for me to give a special thanks to all who have helped me immensely and whose valuable support could never be overstated.

Firstly, I am extremely thankful to my thesis supervisor Prof. Plamen Stamenov. He has been very helpful in every aspect of my research work. He has led me into the vast and interesting field of magnetism and spin-electronics with his great patience and impeccable leadership. He also provided me more than enough time to learn the new things on my own pace so that I can develop a deeper understanding of subjects. I am also very thankful of him to provide me the opportunity to attend several national and international conferences and summer schools in course of my Ph.D. journey. I am deeply grateful to him for whatever I have accomplished in my academic career so far and will accomplish in the future.

I would like to thank my co-supervisor Prof. J.M.D. Coey for teaching and guiding me with his great knowledge and skills. He has provided me several opportunity to work on topics beyond the work presented in this thesis. I would also like to acknowledge the support from Dr. Karsten Rode. This work would not have been completed without his guideline and skills.

I am grateful to many group members of Magnetism and Spin Electronics. I would like to acknowledge the support from Dr. Munuswamy Vanketasan for helping me to in the magnetometry measurements. I am thankful to Dr. Zsolt Gercsi for his help with cryostat and advice on various interesting topics on magnetism.

I am also grateful to Dr. Gwenael Atcheson for his constant support on a number of tools within our lab. Many thin-film samples were prepared by him, which played a central role in this study. I am thankful to equally helpful post-doc member of group, Dr. Jean Besbas, Dr. Niclas Teichert, Dr. Anup Kumar and Dr. Yangkun He.

I would like to thank all the current and past members of my group for all the help and support they have provided. My PhD journey was made pleasant by the friendly environment of the group.
I am grateful to many technical and non-technical staffs of CRANN and School of Physics for being very helpful at countless occasions.

Finally, I am thankful to my parents for their constant love and support.

Summary

Modern day information technologies not only rely on miniaturization and densification of data processing and data storage, but also on fast data transmitters and receivers. Current CMOS based technologies are limited to tens of GHz read and write speeds, at least for ambient temperature operation. Alternative approaches come from areas like spin electronics, using different principles and material sets. Here we build an approach relying on highly spin-polarized low-moment magnetic materials as the active building blocks in switching and oscillation devices.

One particular material class, which has been predicted in 1995 by val Leuken: the zero moment half metals (ZMHM) could potentially offer solutions for achieving high-frequency operation magnetic devices, well into the THz region. Despite the early prediction, the potential of ZMHMs was not realized experimentally until 2014, with $\mathrm{Mn_2Ru_xGa}$ (MRG) being the first known prototype. Narrow-band ferromagnetic resonance, well above 0.2 THz, where the central frequency is determined by the anisotropy field within the material, has already been demonstrated in the Mn-Ga family. Tantalizing prospects emerge, for the realization of spintronic oscillators and switchers, operating well into the THz region, by exploiting higher-order anisotropy effects and non-linear excitation, relying on either high galvanic current densities and spin-transfer or spin-orbit torques, or on optical excitation, using ultra-short laser pulses.

Here we deploy a number of primarily electronic transport-based techniques to shed light over all essential effective parameters necessary for device design using MnGa-based materials, including junction transport in superconductor-ferrimagnet dynamically-formed contacts, anomalous Hall effect in lithographically defined bars at both low and high current densities. The basic spintronics theory is introduced first, before details are provided on the theoretical framework for the analysis of specialized measurement data, such as point contact Andreev reflection (within the modified Blonder-Tinkham-Klapwijk formalism) and spin-orbit torque, within the sub-lattice macrospin approximation.

A separate chapter is dedicated to the description of the measurement techniques, methodologies and equipment used in this work, including examples from the literature, before going into discussing experimental and modelling efforts in three complementary directions: systematic investigation of the Fermi-level polarization as a function of the composition in the MRG-family of materials, an exhaustive determination of the effective low-frequency dynamics and quasi-statics torque parameters, and the changes in these in the high-current density transport regime. The investigation of the possibilities of Fermi level engineering of MRG films, primarily by tuning electronic pressure, (using the Mn/Ru ratio in the films), is presented first. It highlights the importance of electronic pressure (via a combination of substrate-induced strain and chemical pressure) in MRG for the achievement of very high Fermi level spin-polarization ($> 63\%$ has been observed). Here the quantification of spin-polarization is done by means of point contact Andreev reflection (PCAR) spectroscopy.

A detailed analysis of the magnetocrystalline anisotropy of MRG samples by means of the spontaneous or anomalous Hall effect (AHE) follows. In MRG, the AHE is sensitive towards the out of plane component of the magnetization of primarily one of the two spin sub-lattices, which contributes most of the DOS at the Fermi level. It also allows for the determination of the torque acting on the same. This is rather useful in thin epitaxial films, of low-moment materials, where the conventional bulk techniques (such as SQUID magnetometry) run out of sensitivity. A new methodology is proposed for the comprehensive determination of the anisotropy constants in thin film with substantial AHE, which relies on obtaining data for different field rotations, conducted at varying field strengths. In MRG, the out of plane anisotropy constants are determined as follows: $K_1 = 4.0 \times 10^4$ J m^{-3} ($K_1/M = 0.655\,\mathrm{T}$), $K_2 = 2.54 \times 10^4$ J m^{-3} ($K_2/M = 0.416\,\mathrm{T}$) and in-plane effective anisotropy constant is evaluated as $K_3 = 3.48 \times 10^3$ J m^{-3} ($K_3/M = 0.057\,\mathrm{T}$), all by fitting the anomalous Hall resistance to a consistent set of torque models, under the macrospin approximation. First order reversal curves (FORCs) and a classical Preisach hysteresis (hysterons) model are deployed in the modelling of the hysteretic response of the structures and assert the validity of the macrospin approximation and help to determine effective magnetic viscosity parameters.

The measurements of current induced spin orbit torques in single-layer MRG films are presented and discussed last. The effective spin-orbit field is high, without the need to involve any heavy metal over-layers, with values in excess of 5×10^{-12} TA^{-1}m^2 at low current density and 75×10^{-12} TA^{-1}m^2 at a current density of only $j = 2.5 \times 10^{10}$ Am^2. The high values of the observed intrinsic spin-orbit torques in MRG suggest alternative approaches to the realization of spintronic oscillators for the upper GHz and the THz bands, relying on high current densities conducted in-plane, within essentially all-metal micronic-size structures, rather than perpendicular-to-plane through critical tunnel barriers, within nano-pillars.

In the conclusions of this thesis we argue that highly-polarized compensated ferrimagnets may indeed hold the right combination of high effective torques, low precession moments, low damping and high resonance frequencies to put spin electronics back into the beyond CMOS race.

Contents

List of Figures

List of Tables

1

Introduction

1.1 Introduction to magnetism

While the phenomenon of magnetism was known from the ancient times, it has been only explained after the discovery of quantum mechanics. Magnetism is caused by the quantum-mechanical behavior of predominantly electrons. In fact, magnetism continues to be the testing ground to our understanding of complex quantum and statistical physics both theoretically and experimentally.

1.1.1 Classification of (spontaneous) magnetic order

Spontaneous magnetism is a collective behavior of electrons,[1] where spin and orbital moment of electron participate during the interactions. These mutual interactions lead to breaking the momentum symmetry of the system, which results in the ordered ground states. A simplified Hamiltonian of the interacting electrons can be written as:

$$\mathrm{H} = -\frac{1}{2}\sum_{i,j} J_{i,j}\mathbf{S}_i \cdot \mathbf{S}_j + \sum_i g\mu_0\mu_B \mathbf{H} \cdot \mathbf{S}_i \, , \tag{1.1}$$

where, $\mathbf{S}_i$ is the moment on the i^{th} atom, g is the gyromagnetic ratio, μ_0 is the permeability of free space, μ_B is the Bohr magneton and $\mathbf{H}$ is the applied magnetic field. $J_{i,j}$ is the exchange constant, if $J_{i,j} > 0$ it is lower energy if i^{th} and j^{th} moments are aligned, on the other hand if $J_{i,j} < 0$ then antialigned moments lower the energy. The value of $J_{i,j}$ drops rapidly as the separation between moments increases. In a

---

[1] Although, magnetism of nuclei does exist, it is much smaller (factor of $\sim$ 2000) than the electronic moment.

system where only neighboring moments are assumed to interact with the same strength, equation 1.1 can be rewritten as (Heisenberg Hamiltonian);

$$\mathrm{H} = -\frac{1}{2}J\sum_{\langle i,j\rangle_{nn}} \mathbf{S}_i \cdot \mathbf{S}_j + g\mu_0\mu_B\sum_i \mathbf{H}\cdot\mathbf{S}_i\,. \tag{1.2}$$

- **Ferromagnets:** If $J > 0$ then moments will try to stay aligned together developing a macroscopic magnetization ($M > 0$), see figure 1.1.

- **Antiferromagnets:** If $J < 0$ then it is favorable for nearest neighbor magnetic moments to align antiparallel to each other. If moments on the neighboring sites are equal in magnitude then the net magnetization collapses ($M = 0$) but yet it has magnetically ordered states. It may be realized in a magnetic system, where two sub-lattices have equal and opposite magnetic moments.

- **Ferrimagnets:** A ferrimagnet can be regarded as an antiferromagnet with two unequal sub-lattices. The unequal sub-lattices are due to nonequivalent chemical composition and/or crystal environments. In this case, two sub-lattices are not equal therefore material has a net magnetization ($M > 0$). Due to the different crystallographic environment, each sub-lattice has different temperature dependency, therefore net magnetization itself has a complicated temperature dependency. If one sub-lattice dominates at low temperature and another at high temperature, then the net magnetization may collapse and change sign at a temperature known as the compensation temperature (T_{comp}).

Most oxides with a net magnetic moment are ferrimagnets. One of the famous examples is yttrium-iron garnet (YIG), $\mathrm{Y_3Fe_5O_{12}}$. Here Ye^{3+} shows $4d^0$ state, so no magnetic contribution from it. However, Fe^{3+}, $3d^5$, ions occupy two different crystallographic sites, one at the octahedral site and another at the tetragonal site with neighbouring oxygen. These two sites are antiferromagnetically coupled so that the net moment is $5\mu_B$. Another oxide family, which shows ferrimagnetic properties is ferrite, with formula $\mathrm{DO\cdot Fe_2O_3}$, where D is the divalent cation such as Co^{2+}, Mn^{2+}, Fe^{2+}, Ni^{2+} or Zn^{2+}. Here D^{2+} occupies the tetrahedral sites (say A) and Fe^{3+} takes the octahedral sites (say B) of spinel structure. In inverse spinel structure Fe^3+

and D^{2+} occupy the site A and site B respectively, and their moments are antiferromagnetically coupled so that total magnetic moment of sample is given by D^{2+} ions only.

Note that the compensation temperature of ferrimagnetic materials depends on the relative strength of intralattice and interlattice exchange constants. The Hamiltonian for a ferrimagnetic system with lattice indices A and B can be written as:

$$\mathrm{H} = -\frac{1}{2}\sum_{i,j} J^{A}_{i,j}\mathbf{S}^{A}_{i}\cdot\mathbf{S}^{A}_{j} - \frac{1}{2}\sum_{i,j} J^{B}_{i,j}\mathbf{S}^{B}_{i}\cdot\mathbf{S}^{B}_{j} - \frac{1}{2}\sum_{i,j} J^{AB}_{i,j}\mathbf{S}^{A}_{i}\cdot\mathbf{S}^{B}_{j} + \sum_{i} g\mu_0\mu_B\mathbf{H}\cdot\mathbf{S}_{i}\,, \tag{1.3}$$

where, $J^{A}_{i,j}$ and $J^{B}_{i,j}$ are intralattice ferromagnetic exchange constants at site A and B respectively. $J^{AB}_{i,j}$ is the interlattice exchange constant. The net magnetic moment $M = M_A + M_B$, in general, shows a complicated temperature dependency, due to a relative strength of $J^{A}_{i,j}$, $J^{B}_{i,j}$ and $J^{AB}_{i,j}$.

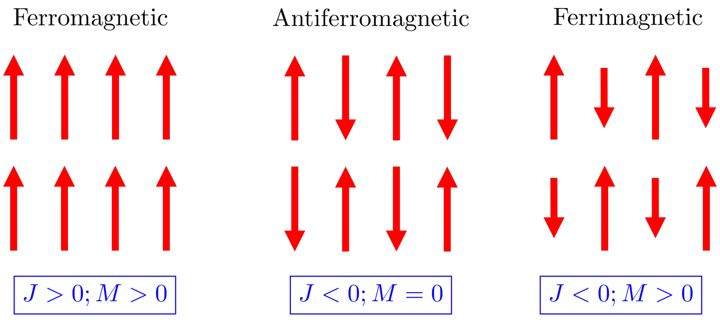

Figure 1.1: An illustration of various spontaneous magnetic systems. In the case of positive exchange constant $J > 0$, moments align parallel to each other developing a net macroscopic magnetization ($M > 0$). This is a ferromagnetic state. On the other hand, $J < 0$ leads to an antiparallel moment configuration. In case of neighboring sites have equal moments, the net magnetization collapses ($M = 0$). This is an antiferromagnetic state. However, a ferrimagnetic state is realized when $J < 0$ and neighboring sites have unequal moments.

Figure 1.2 shows two different situations, a magnetic compensation point is not realized if $|J^{AB}_{i,j}| \gg |J^{A}_{i,j}|, |J^{B}_{i,j}|$, while the compensation can be seen in a situation when $|J^{B}_{i,j}| \gg |J^{AB}_{i,j}|, |J^{A}_{i,j}|$. Most of the ferrites samples come under the first situation, where no realistic compensation is realized. On the other hand $Gd_3Fe_5O_{12}$ has compensation temperature $\approx 290\,\mathrm{K}$ as it falls under the second condition.

Most Oxide ferrimagnets are electrical insulators, which makes them useful for many applications such as in a high frequency circuits. This is because conventional ferromagnets are a lossy media for high frequency applications.

There are many metallic ferrimagnetics alloys of rare earths (RE) and transition metals (TM), such as GdFeCo [19], $TbCo_5$ [20], $DyCo_5$ [21]. In addition, a number of Heusler alloys such as Mn_2Ru_xGa [22], $Mn_{1.5}V_{0.5}FeAl$ [23], Mn_3Al [24], also show ferrimagnetic properties. The Transport properties of a ferrimagnetic sample often show a change in the sign of corresponding coefficients for a temperature above and below the compensation point, such studies on highly ordered Mn_2Ru_xGa thin-films are presented in the chapter 4.

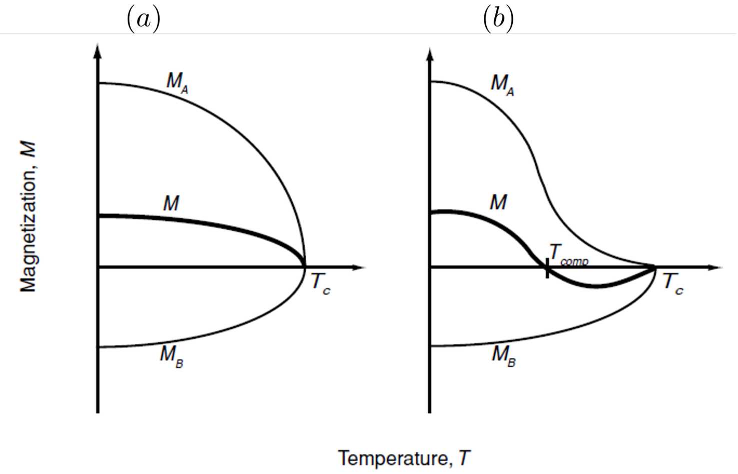

Figure 1.2: A typical temperature dependence of the sub-lattice magnetization of a ferrimagnet, (a) when $|J_{i,j}^{AB}| \gg |J_{i,j}^{A}|, |J_{i,j}^{B}|$, no magnetic compensation is realized, (b) a compensation point (T_{comp}) is achieved when $|J_{i,j}^{B}| \gg |J_{i,j}^{AB}|, |J_{i,j}^{A}|$. The graphs are after Coey [1].

1.1.2 Stoner criterion for ferromagnetism

Band splitting for an itinerant electron system in the absence of external magnetic field at the first glance seems unfavourable, as band-splitting costs extra energy to the system. However, in a situation where the density of states (DOS) at the Fermi level is very high and the band is sufficiently narrow, the energy gain of the process of placing electron from one spin-band to another spin-band may overcome the cost of energy require for exchange splitting. Thus, the bands split spontaneously and ferromagnetism occurs in some itinerant electron systems. This governing condition is set by the Stoner criterion:

$$I\mathcal{N}_{\uparrow,\downarrow}\left(E_F\right) > 1\,, \tag{1.4}$$

where, I is the exchange integral and $\mathcal{N}_{\uparrow,\downarrow}\left(E_F\right)$ is the DOS per atom for each spin state at the Fermi level. Fe, Co and Ni meet the above criterion, consequently exhibit spontaneous ferromagnetism.

1.1.3 Magnetic anisotropy

A magnetic material shows magnetic anisotropy as its free energy depends on the orientation of local magnetization ($\mathbf{M}$). The anisotropy favours an orientation, known as easy axis (or cone/plane), of magnetization for which energy is minimum, while the hard axis (or cone/plane) is the orientation for which energy is maximum. In fact, the anisotropy is often evaluated by measuring the energy needed to saturate the sample along the hard axis as compared to saturating along an easy axis. The anisotropy arises due to contributions from the intrinsic material properties, shape of the material and stress exerted on the material.

In fact, magnetic anisotropy plays a key role in many electronic devices. It determines the read/write speed and volatility of magnetic-based memory technologies. Anisotropy is also crucial for the thermal stability of nano-pillars. Hence, its study is essential in order to understand the dynamics of magnetization in devices.

1.1.3.1 Magnetocrystalline anisotropy

Microcrystalline anisotropy arises from the intrinsic properties of the material. The physical origin of magnetocrystalline anisotropy is spin-orbit coupling. The spin-orbit interaction couples the spin with the orbital degree of freedom. Orbitals are strongly coupled with the local crystal lattice. Therefore any attempt to change the direction of spin moment, using magnetic field, experiences a torque from orbitals. Since, coupling of orbitals depends on the symmetry of the material (local crystal field), a natural preferred orientation of magnetization emerges.

Thus magnetocrystalline energy can be written in terms of series expatiation of magnetization orientation. Anisotropy energy for a number of symmetry are shown

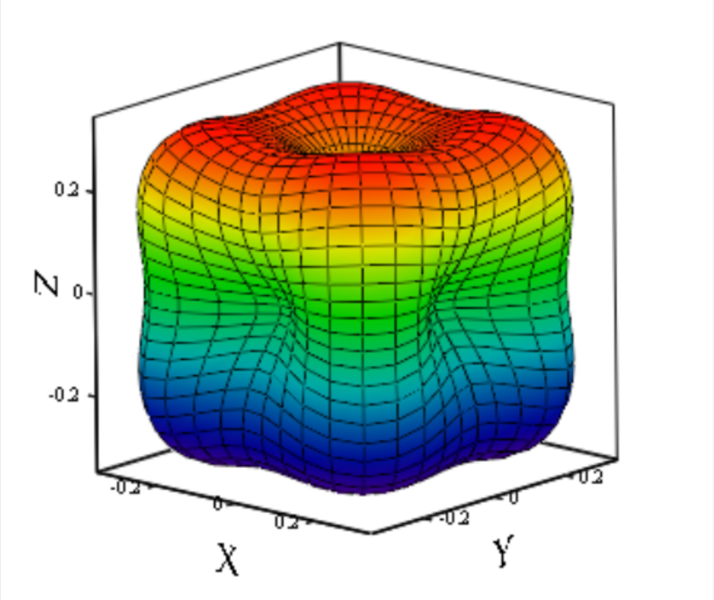

Figure 1.3: Anisotropic energy landscape for cubic crystal as described by equation 1.5. Here $K_0 = 0.2$, $K_1 = 0.8$ and $K_2 = 0$. Both radial distance and color-map indicate the energy. The color of anisotropic energy landscape denotes the arbitrary values from low (blue) to high (red). There are 6 easy axes along $< 100 >$ and hard axes along $< 111 >$.

below:

$$\text{Cubic}: \quad E_a = K_0 + K_1(\alpha_1^2\alpha_2^2 + \alpha_2^2\alpha_3^2 + \alpha_3^2\alpha_1^2) + K_2\alpha_1^2\alpha_2^2\alpha_3^2 + \dots \tag{1.5}$$

$$\text{Tetragonal}: \quad E_a = K_0 + K_1 \sin^2(\theta) + K_2 \sin^4(\theta) + K_3 \sin^4(\theta)\cos(4\varphi) \tag{1.6}$$

$$\text{Hexagonal}: \quad E_a = K_0 + K_1 \sin^2(\theta) + K_2 \sin^4(\theta) + K_3 \sin^6(\theta) + K_4 \sin^6(\theta)\sin(6\varphi) \tag{1.7}$$

here, α_i are the direction cosines of magnetization, while θ and φ are the polar and azimuthal angle of magnetization. K_j are the anisotropy constants of order i.

In a cubic system, for $K_1 > 0$, directions along $< 100 >$ are easy axes while $< 111 >$ are the hard axes, as shown in figure 1.3. This kind of anisotropic behaviour is observed in body-centred-cubic iron (Fe). On the other hand, when $K_1 < 0$, easy axes are along $< 111 >$ and hard axes are along $< 100 >$, see figure 1.4. The face-centre-cubic nickel (Ni) shows similar properties.

Furthermore, in a Hexagonal system, for $K_1 > 0$, uniaxial easy axes are along $< 100 >$, which leads to an uniaxial anisotropy of the sample, as shown in fig-

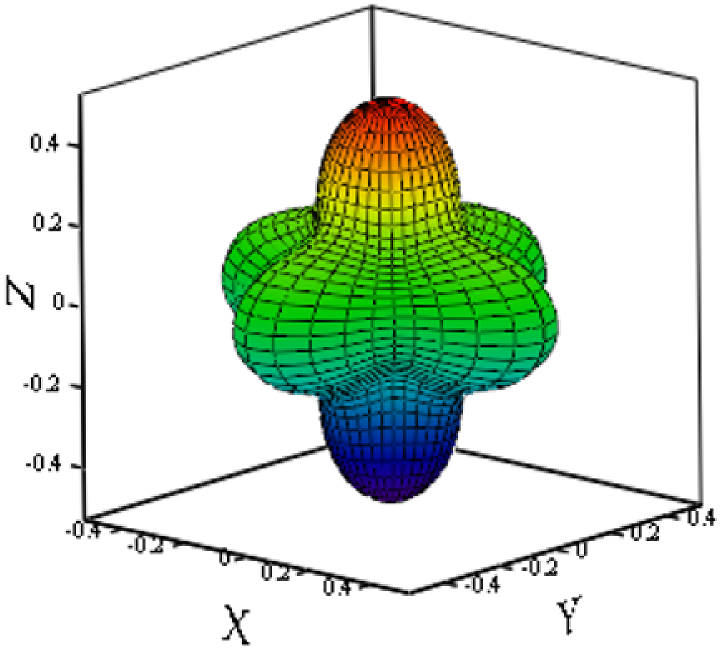

Figure 1.4: Anisotropic energy landscape for cubic crystal as described by equation 1.5 . Here $K_0 = 0.5$, $K_1 = -0.8$ and $K_2 = K_3 = 0$. Both radial distance and color-map indicate the energy. The color of anisotropic energy landscape denotes the arbitrary values from low (blue) to high (red). Here, the easy axes are along $< 111 >$ and hard axes are along $< 100 >$.

ure 1.5. Hexagonal closed-packed cobalt (Co) shows such properties. However, for $K_1 < 0$ an easy plane in xy-plane is realized, see figure 1.6.

A stable equilibrium position of the magnetization vector, in presence of applied magnetic field, can be obtained by finding the minima of energy landscape. For example in the simplest situation of tetragonal/hexagonal crystal system, the effective energy (E_a) is given in terms of magnetocrystalline energy and Zeeman energy :

$$E_a = K_0 + K_1 \sin^2(\theta) - \mu_0 MH \cos(\alpha_H - \theta)\,, \tag{1.8}$$

where, α_H is the polar angle of applied magnetic field with respect to the easy axis, see figure 1.7. If field is along the hard axis, ($\alpha_H = \pi/2$) then minimizing E_a by evaluating $\partial E_a/\partial\theta = 0$ and setting $\theta = \pi/2$, provides the anisotropy field H_a:

$$H_a = \frac{2K_1}{\mu_0 M}\,. \tag{1.9}$$

A thorough discussion of evaluating the anisotropy constants for a tetragonal system

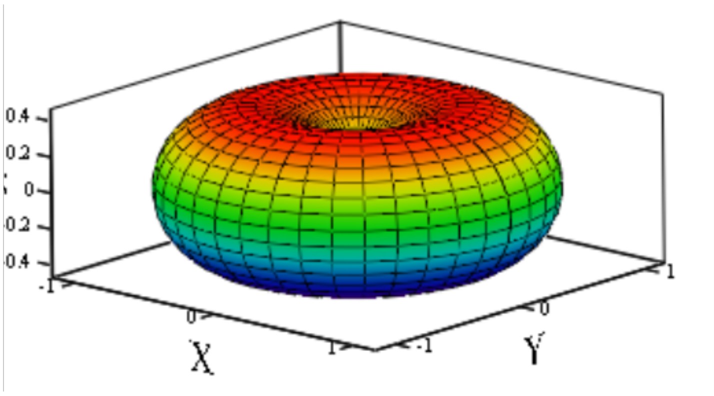

Figure 1.5: Anisotropic energy landscape of a hexagonal crystal system as described by equation 1.7. Here $K_0 = 0.1$, $K_1 = 1$ and $K_2 = K_3 = 0$. Both radial distance and color-map indicate the energy. The color of anisotropic energy landscape denotes the arbitrary values from low (blue) to high (red). In this situation easy axes are along $< 100 >$.

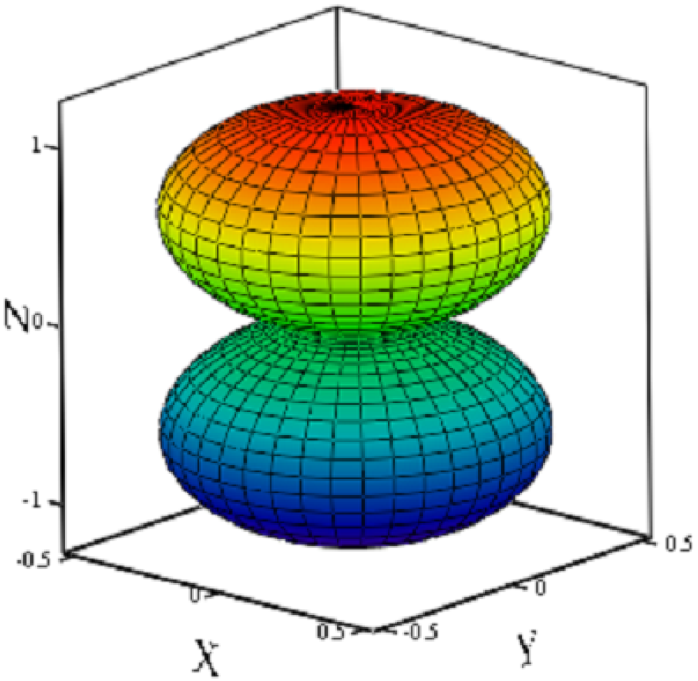

Figure 1.6: Anisotropic energy landscape for hexagonal crystal. Here $K_0 = 1.2$, $K_1 = -1$ and $K_2 = K_3 = 0$. Both radial distance and color-map indicate the energy. The color of anisotropic energy landscape denotes the arbitrary values from low (blue) to high (red). For $K_1 < 0$ an easy plane in xy-plane is realized.

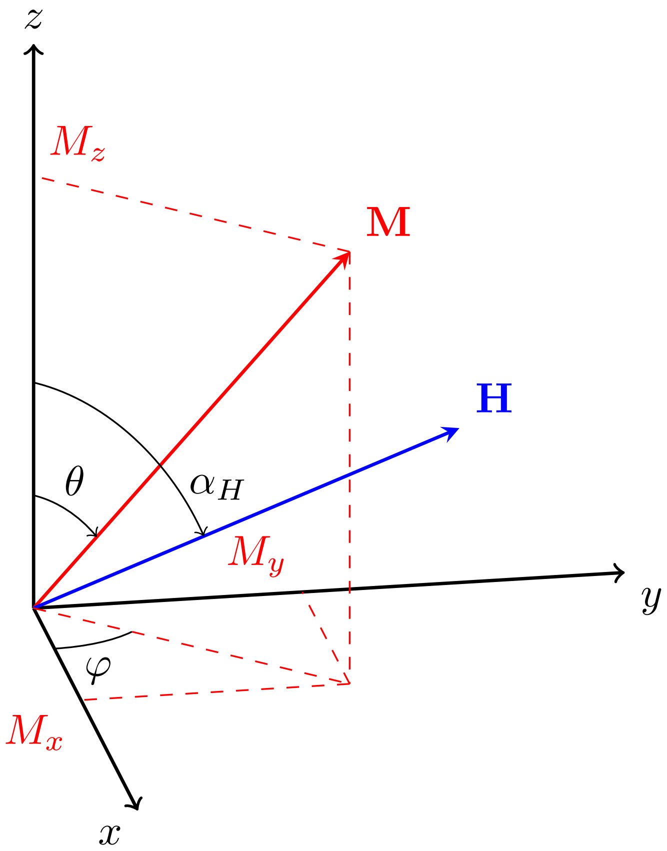

Figure 1.7: An illustration of co-ordinate system for the magnetization $\mathbf{M}$ and a applied magnetic field $\mathbf{H}$. Here, easy axis is considered along z-direction. θ and φ are the polar and azimuthal angles of magnetization $\mathbf{M}$ with respect to the easy axis z. Similarly, α_H is the polar angle of applied magnetic field $\mathbf{H}$.

(Mn_2Ru_xGa) is presented in chapter 4.

1.1.3.2 Shape anisotropy

Shape anisotropy is also referred as magnetostatic anisotropy. It arises from the dipole interaction of moments. A material prefers to magnetize in such way that it has fewest poles, hence minimum magnetostactic energy. This is the reason behind a non-spherical sample getting easily magnetized along its long axis.

The shape anisotropy is related to the demagnetization field, H_d. It contributes to the total energy of the magnetic system, which depends on the direction of magnetization of a sample. It is not an intrinsic property of the material as it depends on the shape of the sample. In case of ellipsoid sample, H_d is given by:

$$H_{d,i} = -N_{i,j}M_j \,, \tag{1.10}$$

where, $N_{i,j}$ is the demagnetization tensor. When the magnetization is parallel to one of the principle axis of ellipsoid, the demagnetization tensor is essentially a diagonal matrix with trace equal to unity.

In case of a spherical sample, $N_x = N_y = N_z = 1/3$. Hence H_d is isotropic in nature. For a long cylinder, with axis along z, $N_x = N_y = 1/2$ and $N_z = 0$. Therefore no demagnetization field along the long axis, hence M align along z-direction. On the other hand, for a thin film, with thickness along z-direction, $N_x = N_y = 0$ and $N_z = 1$. Thus most thin films have shape anisotropy along the plane of a sample.

1.1.3.3 Magnetoelastic anisotropy

Magnetoelastic anisotropy arises in a sample when it is subjected to stress. The origin of this is also spin-orbit coupling. When stress is applied on a sample, it alters the local symmetry in the neighborhood of atoms, and consequently the magnetic behavior. For a cubic system, magnetoelastic anisotropy energy density E_{ME} is given by [25]:

$$E_{ME} = B_1(\epsilon_{11}\alpha_1^2 + \epsilon_{22}\alpha_2^2 + \epsilon_{33}\alpha_3^2) + 2B_2(\epsilon_{12}\alpha_1\alpha_2 + \epsilon_{23}\alpha_2\alpha_3 + \epsilon_{31}\alpha_3\alpha_1) + \ldots \,, \tag{1.11}$$

where, $\epsilon_{i,j}$ is the strain tensor, B_i are the magnetoelastic coefficient and α_i are the direction cosines of the magnetization vector. Thus an uniaxial strain in a cubic system induces an uniaxial magnetoelastic anisotropy.

1.2 Spin electronics

Spin electronics or spintronics refers to the study of both charge and spin degree of freedom of electron in condensed matter physics [26]. It primarily exploits the spin of the electron in order to understand the physical properties of a system [27, 28]. For example, study of transport and relaxation properties of spin in metals and semiconductors is not only a fundamental interest but also demonstrated in various spin-based devices, such as in gaint magnetoresistance (GMR), tunnel magnetoresistance (TMR) sensor, spin-oscillators, etc.

1.2.1 Spin polarization

The Fermi level spin polarization[2] is defined by:

$$P_i = \frac{D_\uparrow v_\uparrow^i - D_\downarrow v_\downarrow^i}{D_\uparrow v_\uparrow^i + D_\downarrow v_\downarrow^i}\,, \tag{1.12}$$

where, $D_{\uparrow(\downarrow)}$, $v^i_{\uparrow(\downarrow)}$ are the density if states (DOS) and Fermi velocity of spin-up (spin-down) channel, and $i = 0, 1$, and 2. For $i = 0$, it represents the bare DOS spin polarization and is usually measured by spin-resolved photoemission spectroscopy. On the other hand, transport measurements measure a different spin polarization, which includes the Fermi velocity. In the ballistic regime, electrons do not lose their momentum and energy in the transport channel. Therefore, DOS is weighted with linear Fermi velocity v ($i = 1$) and P_1 is measured on a particular axis. In the diffusive regime, electrons lose both momentum and energy in a transport channel, hence the weighting is quadratic in v ($i = 2$) and P_2 is measured. P_1 and P_2 can be measured by point contact Andreev reflection spectroscopy (PCAR).
The spin polarization value of non magnetic metals is zero and, for magnetically ordered states, its value lies between 0 and 1 (Figure 1.8). In an extreme case, where there is a spin gap in one of the spin channel, spin polarization reaches the maximum value of 1, and the material is named half-metal. Some Heusler alloys, like NiMnSb and Mn_2Ru_xGa , Perovskite ($SrRuO_3$) and transition metal oxides (CrO_2) show half-metallicity.

1.2.2 Spin valves

In 1988, a large magnetoresistance in Fe/Cr multilayers was observed by Binasch et al. [29] and Baibich et al. [30]. In this multilayer, the thickness of the nonmagnetic layer is chosen in such as way that two consecutive ferromagnetic layers are anti-ferromagnetically coupled to each other through Ruderman–Kittel–Kasuya–Yosida

---

[2] This is the polarization which matters for the transport phenomena.

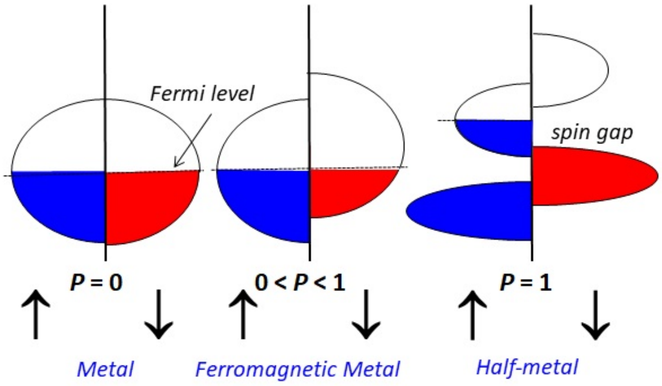

Figure 1.8: Schematic of spin dependent density of states (DOS) of typical metal $P = 0$, ferromagnet $0 < P < 1$ and half metal $P = 1$.

(RKKY) interaction [31]. Thus, ferromagnetic layers have opposite polarities at zero applied field. Furthermore, the oscillatory nature (between ferromagnetic and antiferromagnetic) of RKKY interaction was established by Parkin et al. [32, 33]. When a current flow in the plane of sample, the resistance of antiparallel alignment is more than the parallel alignment. The parallel alignment is achieved by applying magnetic field in the plane of sample. The resistance of the parallel state was found to be ∼ 50% lower than than the parallel state at 4.2 K. Therefore, such multilayer device is called a spin-valve or giant magnetoresistance (GMR) device. The corresponding GMR ratio is given by:

$$\mathrm{GMR}(\%) = \frac{R_{AP} - R_P}{R_P} \times 100\,, \tag{1.13}$$

where, R_P and R_{AP} are the parallel and antiparallel resistance respectively. GMR can be realized either in current-in-plane (CIP) or current-perpendicular-to-plane (CPP) configuration. The GMR effect arises from a complex spin-dependent scattering at bulk and interface. It can be phenomenologically understood under the Mott two-current model where current is split into up, $I^{\uparrow}$, and down, $I^{\downarrow}$ current components. The electron of $I^{\uparrow}$ scatters less in a magnetic layer where majority electron is also align along the same direction. On the contrary, it scatters more, when its spin is anti-aligned in the magnetic layer. GMR in CPP geometry is shown in figure 1.9.

GMR ratio in CIP-GMR is often very small. It has reached a maximum of value 10%

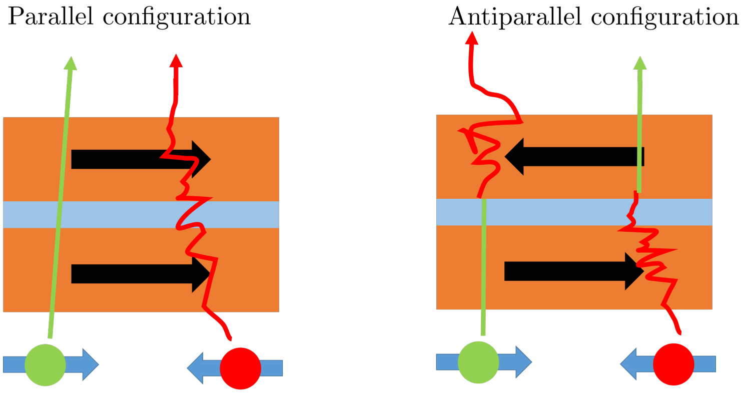

Figure 1.9: An illustration of CPP-GMR in both parallel and antiparallel configurations. Here under Mott two current model, electron with parallel spins have longer mean free path compared to spin aligned antiparallel.

at room temperature, in CoFe/Cu/CoFe multilayer. However, a much higher room temperature GMR ratio (75%) was reported in a epitaxial $Co_2Fe_{0.4}Mn_{0.6}Si/Ag/Co_2Fe_{0.4}Mn$ structure [34].

1.2.3 Tunnelling magnetoresistance

Another spin-valve in the field of spintronics is the tunnelling magnetoresistance (TMR). It is also known as magnetic tunnel junction (MTJ). MTJ is very similar to GMR-valve where the non-magnetic spacer is replaced by a thin ($<$ 2nm) insulating layer (AlO_x, MgO, AlN and $SrTiO_3$ are some of the common choice). The first observation of TMR was made by Julliere [2] with Fe/Ge/Co structure. The reported TMR is around 11% at 4.2 K at zero bias, and it drops quickly with temperature and bias, see figure 1.10. A significant improvement was made in 1995, by Moodera et al. [3] and Miyazaki et al. [35] when TMR in excess of 10% , at room tempearture, has reported with amorphous AlO_x barriers. A further higher value of TMR was observed in 2004 by Parkin et al. [36] and Yuasa et al. [4] with crystalline MgO barrier. Interestingly, TMR as high as 1010% at 5 K and 500% at room temperature was demonstrated by Ikeda et al. [37] in 2008 with CoFeB/MgO/CoFeB MTJ structure.

In a simplest model, proposed by Julliere, the tunnelling current is proportional to the product of DOS of two ferromagnetic layers at the Fermi level. The MTJ and its transport effects is shown in figure 1.11. The tunnelling probability is high in the parallel due to excellent overlap of spin-resolved DOS. On the other hand, in

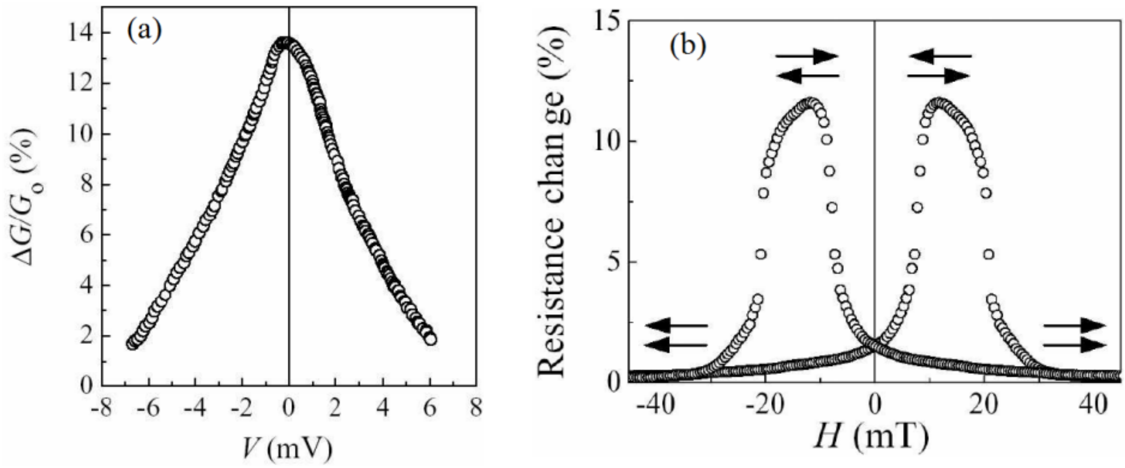

Figure 1.10: (a) The first demonstration of TMR in Fe/Ge/Co at 4.2 K, after Julliere [2], (b) high TMR at room temperature across CoFe/$A1_2O_3$/Co MTJ. The pictures are after Moodera *et al.* [3].

antiparallel situation a poor overlap of spin-resolved DOS leads to lower tunnelling probability. Note that Julliere's model ignores the band structure of the insulating barrier, which is the case of incoherent tunnelling. This condition is only valid for all amorphous barrier, such as AlO_x.

However, in the case of a crystalline barrier (MgO), the band structure of the barrier and corresponding coherent tunnelling across the barrier comes into the picture. For example in CoFe[001]/MgO[001]/CoFe[001] , the tunnelling matrix elements is dominated by Δ_1 symmetry which decay slower than Δ_2 and Δ_5 states [5]. The tunnel process across crystalline barrier is shown is figure 1.12.

1.3 Transport properties

1.3.1 Spontaneous Hall effect

In 1879, Edwin Hall [38] discovered the generation of transverse voltage (Hall voltage) across an electrical conductor when a perpendicular magnetic filed is applied. This phenomenon is popularly known as the normal or ordinary Hall effect. Later, he also observed spontaneous Hall [39] voltage in a ferromagnetic material, even in the absence of external field, which gained the name spontaneous Hall effect (SHE).

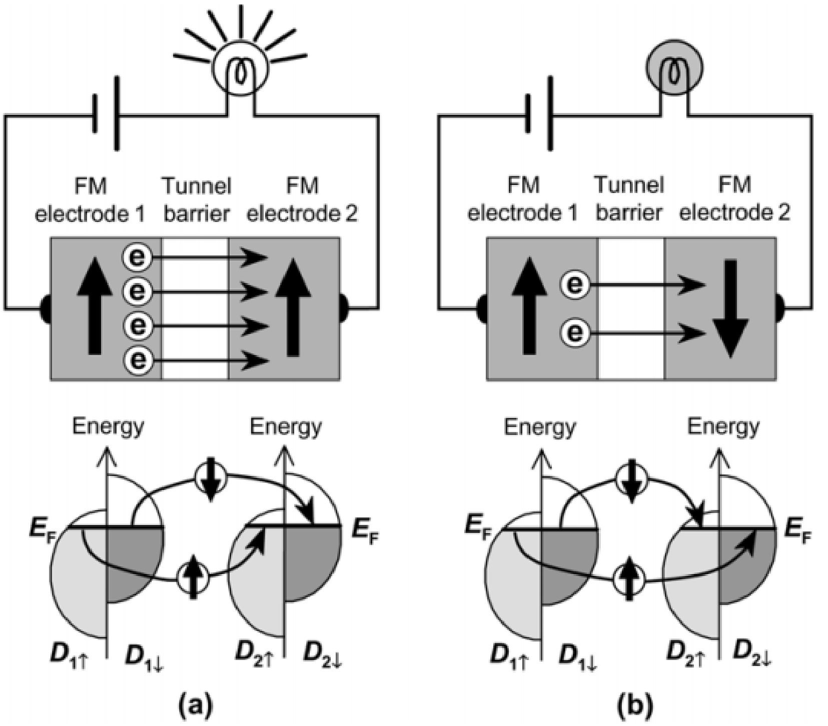

Figure 1.11: An illustration of TMR effect in MTJ, (a) when both magnetic layers are parallel, in this case electrons have higher tunnelling probability due to significant DOS overlapping, (b) in the antiparallel situation where tunnelling probability is low due to very low DOS overlapping. The pictures are after Yuasa *et al.* [4].

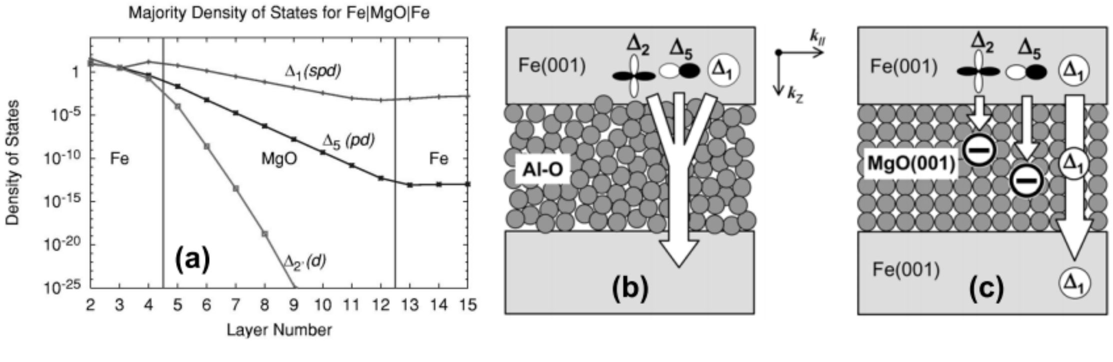

Figure 1.12: (a) Tunnelling DOS across Fe(001)/MgO(001)/Fe(001) MTJ structure for $k_{\parallel} = 0$. Δ_1 state decay much slower across the MgO barrier as compared to Δ_2 and Δ_5 states. (b) Incoherent tunnelling across AlO$_x$ barrier and (c) coherent tunnelling across crystalline MgO barrier. The pictures are after Yuasa *et al.* [4] and Butler *et al.* [5].

An empirical relation for the Hall resistivity can be written as,

$$\rho_{xy} = R_n H_z + R_s M_z \, , \tag{1.14}$$

where, R_n and R_s are the normal and spontaneous Hall coefficients respectively. H_z is the applied magnetic field perpendicular to sample and M_z is the normal component of the magnetization vector.

The ratio of SHE resistivity ρ_{xy} to longitudinal resistivity ρ_{xx} is known as Hall angle α_H, defined as,

$$\alpha_H = \tan^{-1}\left(\frac{\rho_{xy}}{\rho_{xx}}\right) . \tag{1.15}$$

Note that SHE is a non-linear Hall effect arising due to the normal component of magnetization. However, a thermal gradient and complex spin-orbit interactions can also contribute to the non-linearity in the Hall effect, hence named as anomalous Hall effect (AHE). Strictly speaking, SHE and AHE may be associated with quite different physical phenomena. Nevertheless, in this thesis SHE and AHE are interchangeably used owing to the presence of non-linearity in the Hall effect.

Although, the theory of AHE is still under debate, Karplus and Luttinger [40] had first proposed that spin-orbit interaction (SOI) attribute to the AHE. The SOI can be associated with either the crystalline potential (intrinsic contribution) or with impurities associated potential (extrinsic contribution). The net asymmetric impurity scattering (also known as skew-scattering) of charge carrier leads to a linear dependency of ρ_{xy} with ρ_{xx}. Additionally, another extrinsic scattering mechanism, side-jump, scaled has scaling $\rho_{xy} \propto \rho_{xx}^2$ similar to the intrinsic mechanism. The intrinsic contribution is attributed to the resultant net Berry phase acquired by a Bloch state in a Brillouin zone (BZ). The intrinsic Hall conductivity can be evaluated from [41]:

$$\sigma_{ij}^{a} = -\frac{e^2}{\hbar} \int_{BZ} \frac{d^3k}{(2\pi)^3} \sum_{n\mathbf{k}} f_{n\mathbf{k}} \Omega_{n\mathbf{k},ij} \, , \tag{1.16}$$

where, $\Omega_{n\mathbf{k},ij}$ is the Berry curvature tensor and $f_{n\mathbf{k}}$ is the Fermi-Dirac distribution. The AHE is proportional to the degree of spin polarization at the Fermi level and magnetization of the dominant sublattice. Material with high anomalous Hall angle are expected to have a high degree of spin polarization. However, the spin polarization must be verified by other techniques, such as point contact Andreev reflection (PCAR) spectroscopy . A correlation between spin-polarization and anomalous Hall angle is presented in chapter 3.

1.3.2 Point contact Andreev reflection spectroscopy

The conversion of normal current to supercurrent at metal/superconductor (n/s) interface is called Andreev reflection [42]. Point contact Andreev reflection (PCAR) relies on the principle of Andreev reflection, which is the only allowed process of injection of electrons into the superconductor when applied bias voltage is lower than superconducting gap ($|U_a| < \Delta$). For $|U_a| < \Delta$, when an electron (say spin up) in a metal with $P = 0$ propagates towards the interface, a hole of opposite spin reflects back into the spin down DOS due to unavailability of single particle DOS in superconductor (Andreev reflection). This reflection of a hole acts as a parallel conduction channel to the initial electron channel, which gives rise to doubling of the normal conductance (Figure 1.13A & B). On the other hand, if a metal has polarization $P = 1$ then due to unavailability of spin down DOS in the metal near Fermi level, Andreev reflection is fully suppressed which leads to the drop in the normal conductance (Figure 1.13C & D). For intermediate polarization values, the normal conductance lies between these two limiting cases. Strictly speaking, PCAR can measure the Fermi level spin polarization (with meV resolution) of magnetically ordered states by measuring the conductance across a ferromagnet/superconductor interface. The PCAR spectrum can be analyzed using Blonder-Tinkham-Klapwijk (BTK) model [43]. The net current through the interface can be written as,

$$I = (1 - P)I_{unpol} + PI_{pol} \, , \tag{1.17}$$

where, I_{unpol} and I_{pol} are the spin polarized and spin unpolarized current respectively. In BTK model, I_{unpol} and I_{pol} currents are evaluated by solving the Schördinger equation for metal/superconductor (n/s) interface. Interface potential strength $U(x) = W\delta(x)$ can be included in the BTK theory. The effective interface barrier strength (Z) is defined as,

$$Z = \sqrt{\left(\frac{W}{\hbar v_F}\right)^2 + \frac{1-r^2}{4r}}\,, \tag{1.18}$$

where, $r = v_{F1}/v_{F2}$ is the ratio between Fermi velocities in superconductor and metal, v_F is the equilibrium Fermi level velocity. Thus, Z parameter absorbs a few different physical effects: Fermi level mismatch between metal and superconductor, oxide at the interface and general interface scattering.

The normalized conductance of for spin polarized/nonpolarized current can be written as,

$$\frac{G_{ns}}{G_{nn}} = -\left(1+Z^2\right)\int \left[f'(E-eV)\right]\left(1 + A(E) - B(E)\right)\mathrm{d}E\,, \tag{1.19}$$

where, G_{nn} is conductance through metal/metal interface. f' is the first derivative of Fermi distribution. $A(E)$ and $B(E)$ are the Andreev and normal reflection coefficients. Spin polarization can be found by substituting the value of I_{unpol} and I_{pol} from equation 1.19 to equation 1.17.

It can be shown that Andreev reflection probability is inversely proportional to the barrier strength, $A(E) \propto Z^{-2}$. As the transparency of interface decreases (Z increases), Andreev reflection at low voltage is suppressed. For very high Z ($Z > 5$), Andreev reflection is fully suppressed and the spectrum is analyzed in the tunnelling regime. In fact, for very high Z, the spectrum for $P = 0$ looks similar to the Figure 1.13(D). Therefore, to be analyzed for spin polarization, spectra with very high Z values should be avoided.

Another important aspect of PCAR has to do with transport regimes. Transport through the point contact can be in three different regimes: ballistic, diffusive and inelastic. The type of transport is determined by the contact size d, elastic mean free path l_{el} and inelastic mean free path l_{in}. For ballistic regime, $d < l_{el}$, the electrons statistically do not undergo any scattering withing the contact region. Thus both energy and momentum-resolved spectroscopy can be performed. On the other hand, if $d > l_{in}$ (inelastic or thermal regime), the electrons undergo both elastic and inelastic scattering, thereby lose both momentum and energy. This is the transport regime which must be avoided, as the energy resolution is not well defined. In addition, since electrons dissipate energy within the contact region, the Joule heating effectively raises the temperature of contact which could lead to the quenching of the superconducting tip. The last regime is diffusive, $l_{el} < d < l_{in}$, where, electrons undergo predominantly elastic scattering. Therefore, the electrons lose momentum information but retain the energy resolution. Hence, energy resolved spectroscopy can also be realized in the diffusive transport regime. In short, an easy to interpreted PCAR spectrum can be measured only in the ballistic or the diffusive regime. Furthermore, one has to take into account the superconducting proximity effect into BTK model, which results into two superconducting gap Δ_1 and Δ_2 in the mathematical model. This is popularly known as modified BTK (mBTK) theory.

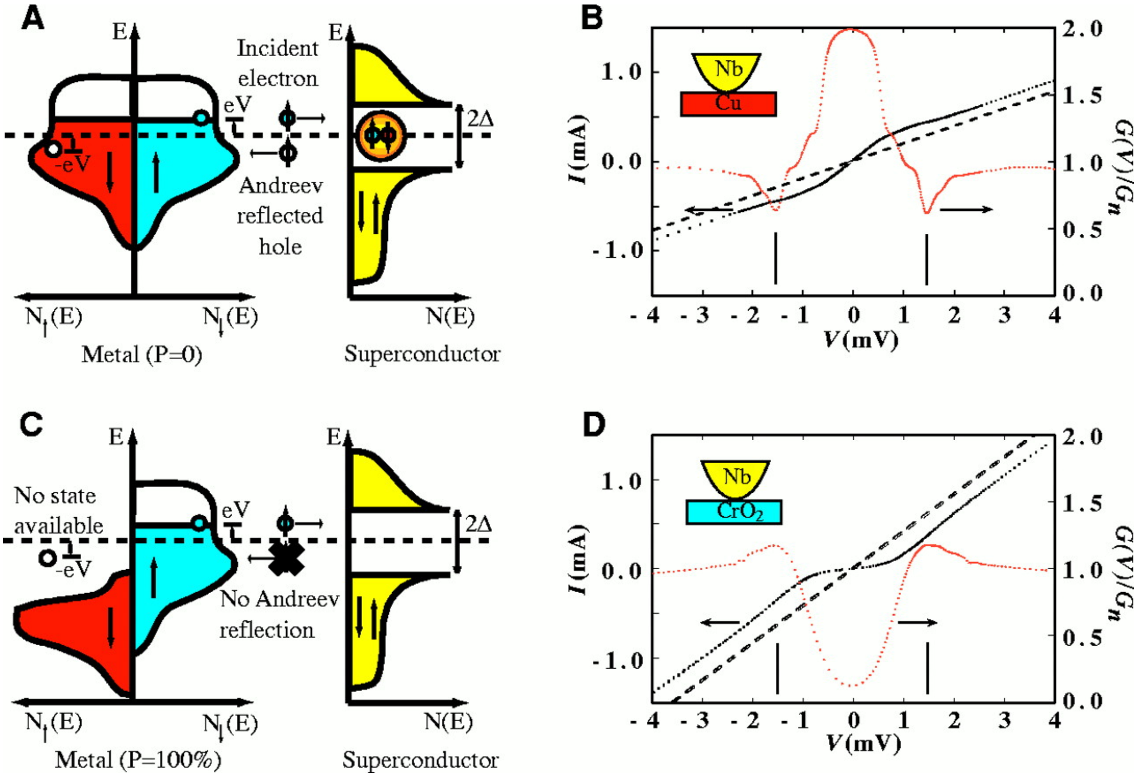

Figure 1.13: Schematic representation of Andreev reflection for (A) $P = 0$, non-polarized metal (Cu) and (C) $P = 1$, half-metallic ferromagnet (CrO_2) . Corresponding experimental spectra are shown in (B) and (D). The pictures are after Soulen *et al.* [6].

1.4 Magnetization dynamics

1.4.1 Spin-transfer torque

When a spin-polarized current passes through a ferromagnet, it exerts torque on the local magnetic moment, due to the fact that the spin-polarized current carries a net angular momentum, see figure 1.14. This phenomena is called spin-transfer torque (STT), and was first proposed by Slonczewski [44] and Berger [45] in 1996. If the quantization axis (vector) of spin-polarized current and magnetization are $\boldsymbol{\sigma}$ and $\mathbf{m}$ respectively, the STT arises due to transverse (non-collinear) component of $\boldsymbol{\sigma}$ acting on $\mathbf{m}$. The equation of motion of the local magnetic moment under spin-polarized current, within macrospin approximation, is described by the Landau-Lifshitz-Gilbert (LLG) expression:

$$\frac{\partial \boldsymbol{m}}{\partial t} = -\gamma \boldsymbol{m} \times \mu_0 \boldsymbol{H_{eff}} + \alpha \boldsymbol{m} \times \frac{\partial \boldsymbol{m}}{\partial t} - a_{SL} \boldsymbol{m} \times (\boldsymbol{\sigma} \times \boldsymbol{m}) - b_{FL} \boldsymbol{m} \times \boldsymbol{\sigma} \,, \quad (1.20)$$

where, the first term of equation 1.20 is the Larmor precession of $\boldsymbol{m}$ around local effective field $\boldsymbol{H_{eff}}$. The effective magnetic field takes contribution from external field, anisotropy field and other quantum mechanical effects. $\boldsymbol{H_{eff}}$ can be written in term of an energy function E:

$$\boldsymbol{H_{eff}} = -\frac{1}{\mu_0} \frac{\partial E}{\partial \boldsymbol{H}} \,. \quad (1.21)$$

The second term of equation 1.20 is the dissipative term arising from the damping within the material, here α is the material damping constant. The third and forth terms describe the contribution from STT, arising from net the angular momentum transfer from the spin-polarized current to the system, where a_{SL} is a Slonczewski-like coefficient and b_{FL} is a field-like coefficient.

The Slonczewski-like torque and field-like torque can be associated with an effective current-induced field along $\boldsymbol{\sigma} \times \boldsymbol{m}$ and $\boldsymbol{\sigma}$ respectively.

An important consequence of STT is that under a suitable critical current (j_c), a stable precession or even switching of magnetization are achievable, see figure 1.15

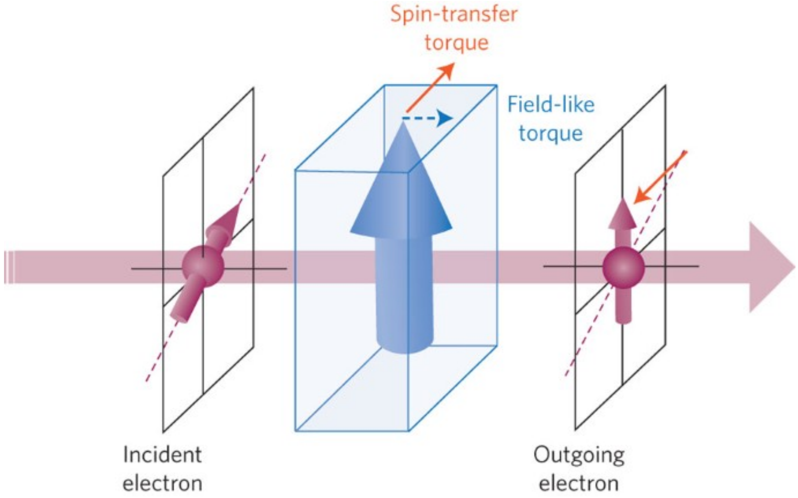

Figure 1.14: In illustration of STT. When spin, $\boldsymbol{\sigma}$, of indecent electron is non-collinear with the $\boldsymbol{m}$ of the ferromagnetic layer, passes through the magnetic layer it exerts the torques on the magnetization. The outgoing electrons align itself parallel to the magnetic moment after losing its angular momentum. The lost angular momentum is absorbed by the ferromagnetic moment $\boldsymbol{m}$, which gives rise to a STT effect. The picture is after Brataas *et al.* [7].

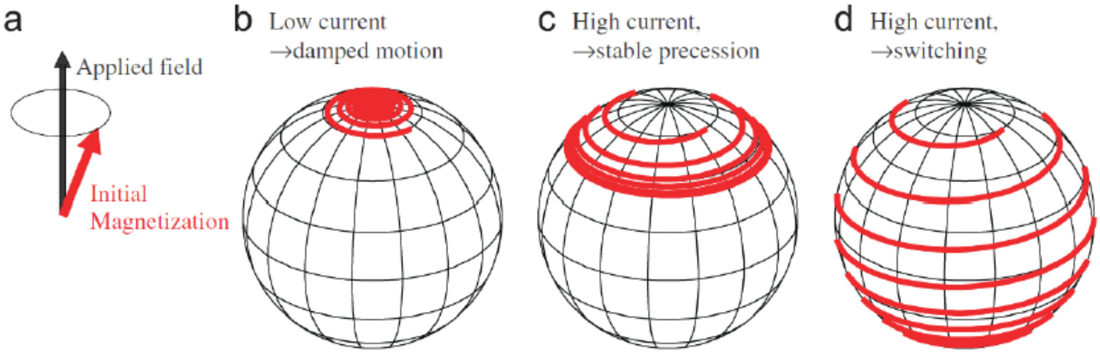

Figure 1.15: magnetization dynamics in various situation under applied spin-polarized current (a) Initial magnetic configuration, (b) for a low threshold current value, magnetization eventually settles along the field due to finite damping present within the sample, (c) when current is high enough to compensate the damping term, a stable precession is achieved, (d) when current is more than the threshold value, a switching process occurs. Here the current induced torque is well in excess to the torque experienced through the anisotropy of the sample. The picture is after Ralph and Stiles [8].

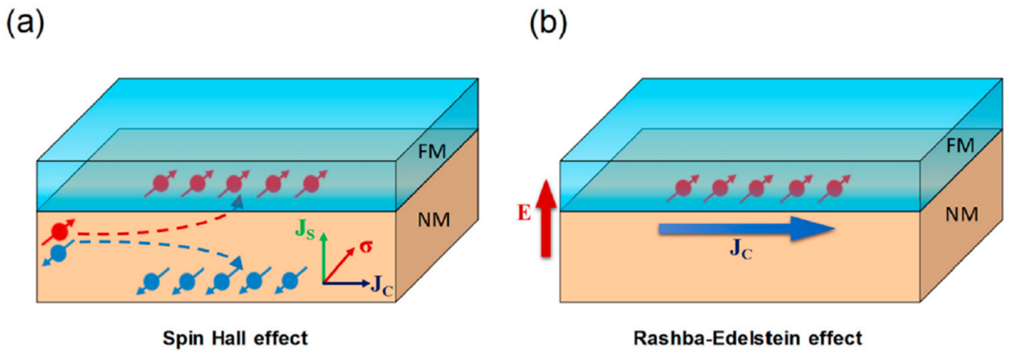

Figure 1.16: (a) Spin Hall effect in a heavy metal , (b) Rashba–Edelstein interfacial effect at the interface of FM/HM. E is the effective electric field induced from the inversion asymmetry at the interface. Note that current is biased along a longitudinal direction of the sample. The picture is after Ramaswamy *et al.* [9].

1.4.2 Spin-orbit torque

The spin-orbit torque (SOT) provides an efficient alternative way to control the magnetization dynamics as compared to STT. The SOT is more commonly realized in a bilayers system composed with heavy metal (Pt, W, Ta, etc, i.e. nonmagnetic material with sizable spin-orbit coupling) and a ferromagnet. The origin of SOT in this hetrostructure combine the spin-Hall effect [46, 47] and Rashba–Edelstein effects [48]. In spin-Hall effect, a transverse net spin current is generated when a charge current passes through the heavy metal (HM) due to high spin-orbit coupling strength of HM. The spin current accumulates at the ferromagnet (FM) and HM interface, then further diffuses into the FM, exerting torques on the local moment mainly through exchange interaction, see figure 1.16. In case of Rashba–Edelstein effect, the inversion asymmetry across the FM/HM interface induces the spin-splitting in the band, which leads to a non-vanishing spin-orbit field. In fact the presence of inversion asymmetry in a bulk sample, with a appropriate symmetry, can also give rise to a spin-orbit field in the sample. A further discussion on SOT is presented in chapter 5. SOT has emerged as a more efficient method to control the magnetization as applied current is biased along the longitudinal direction of sample (figure 1.16). An investigation of bulk SOT is discussed in chapter 5.

1.5 Zero moment half-metals

In 1995, van Leuken and de Groot first predicted a new class of half metal called 'half-metallic antiferromagnet' [49]. Such materials are immune to the external and demagnetizing fields, and at the same time are highly spin polarized at the Fermi level. These are expected to show spin dynamics, lying in terahertz gap (from hundreds of GHz to sub terahertz range frequencies), due to their low damping parameters and high magnetic anisotropy. Several potential candidates such as CrMnSb, Fe_2VGa and $D0_3$ Mn_3Ga have been predicted theoretically as half-metallic antiferromagnets.

Since the theoretical prediction, such a class of materials had never been realized experimentally. Several attempts were carried out to fabricate experimentally, but, all efforts ended with failure, mainly because, either the proposed materials crystallize in a different crystal structure or they are non-magnetic. However, in 2014, Mn_2Ru_xGa (MRG) was finally realized experimentally by Kurt, *et. al.*, as a prototype material [22].

Mn_2Ru_xGa crystallizes in the cubic inverse $L2_1$ structure, where Mn occupy two inequivalent sublattices $4a$ and $4c$, as shown in Figure 1.17a. Moments at $4a$ and $4c$ sublattices are antiferromagnetically coupled, while those on the same sites are ferromagnetically coupled. Due to inequivalent crystal environments both sublattices moments have different temperature dependencies. It has been confirmed through X-ray absorption and dichroism spectroscopy that moment of Mn^{4a} has smaller temperature dependence compared to the moment of Mn^{4c} sublattice (Figure 1.17b). Thus, a perfect compensation point can be tuned by altering the composition and/or by inducing crystal distortion. In MRG, at the Fermi level, the delocalized states are dominated by the Mn^{4c} site, thereby the transport phenomena is dictated by Mn^{4c} electrons. DFT calculations, PCAR ($P > 58\,\%$) and large anomalous hall coefficient confirm its half-metallic properties [22, 50]. Therefore, the unique combination of low net moment, high spin polarization at the Fermi level and high magnetic anisotropy identify MRG as a potential candidate for the next generation THz oscillators/receivers.

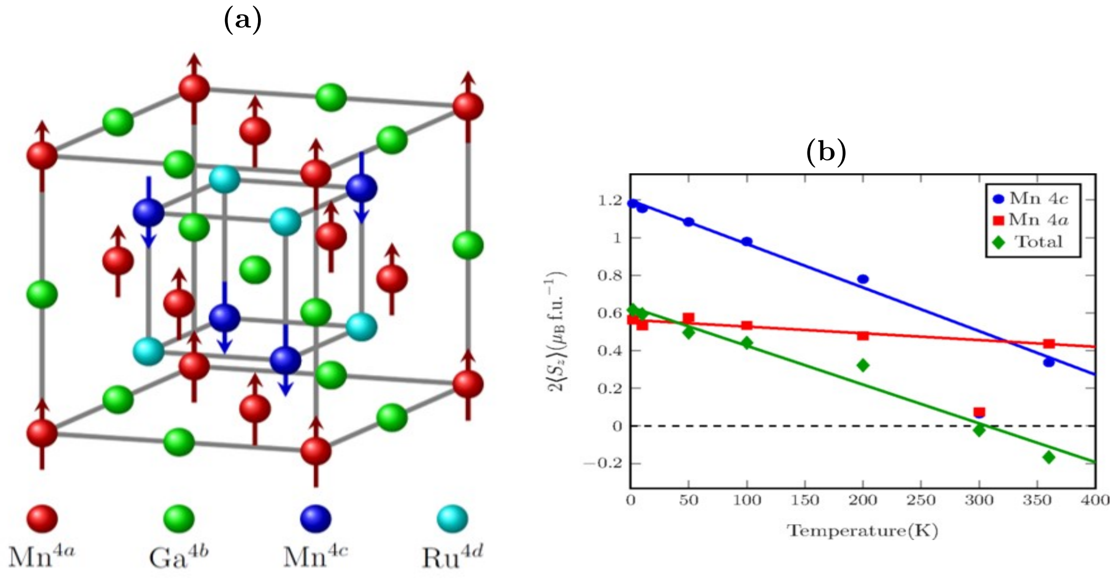

Figure 1.17: (a) Crystal structure of MRG (cubic inverse L2_1 structure) . (b) Temperature dependency of site-specific spin moments $2\langle S_z \rangle$ of MRG; L-edge X-ray absorption and dichroism allow the independent determination of the spin and orbital moments. Perfect compensation near 300 K is clearly visible. The picture is after Betto *et al.* [10].

2

Experimental techniques

2.1 Introduction

This chapter discusses the various experiment techniques utilized to fabricate and analyse the samples under investigation within this thesis work. A high-vacuum Shamrock sputtering tool was used to grow the thin-film samples. The crystallographic properties of blanket samples were investigated using standard X-ray techniques, namely X-ray diffraction (XRD) and X-ray reflectometry (XRR). Furthermore, the magnetic properties of the blanket thin films were studied using a Superconducting QUantum Interference Device (SQUID) magnetometer. The magneto-transport studies of the blank thin-films and micro-patterned devices were performed using electromagnet (GMW) and more sophisticated, superconducting magnet (PPMS) tools. The micro-patterned devices were realized using a standard photolithography, Ar-ion etching and lift-off process. Moreover, the Fermi level spin-polarization of the blanket thin-film samples were examined with the help of point contact Andreev reflection (PCAR) spectroscopy, using superconducting Nb tips.

2.2 Thin-film deposition techniques

2.2.1 Direct-current (DC) magnetron sputtering

DC magnetron sputtering is a physical vapour deposition (PVD) technique, which is used for epitaxial growth of the thin-film of a wide range of mostly metallic materials.

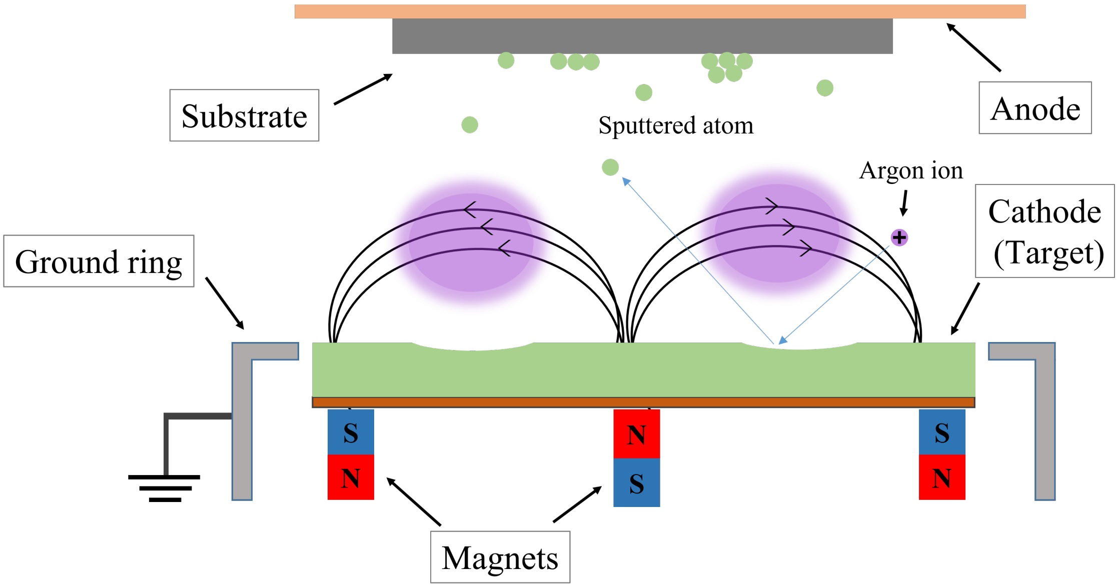

Figure 2.1: Schematic illustration of a DC magnetron sputtering system. A static potential difference is applied between the target (cathode) and the substrate (anode). The magnetic flux from the permanent magnets, underneath the target, enhances the Argon plasma density near the target. The highly energetic Ar^+ ions remove target material after colliding with the target. The ejected material gets deposited onto the substrate.

This is a widely used method in mass production within the semiconductor industry due to its associated low cost, high-yield and low-maintenance characteristics. In this technique, the atoms are sputtered-off from the target material using a cloud of highly energetic ions in a pre-pumped vacuum chamber. Figure 2.1 shows the basic components and mechanism of a DC magnetron sputtering system.

In a sputtering system, constant static electric potential is applied across anode (substrate) and cathode (target). A noble gas (typically Argon) at partial pressure between 1 to 100 mTorr is maintained inside the chamber in order to ignite and sustain the plasma. The positively charged Ar^+ ions accelerate towards the cathode (target) and bombard the target with sufficiently high kinetic energy ($\sim$ 100 eV). Consequently, a stream of atoms from the surface of the target is sputtered-off. The ejected atoms (material) then eventually get deposited on substrate through a drift and diffusion mechanism. The purpose of the permanent magnet structure underneath the target is to trap the ions in a cycloid-like motion which enhances the plasma density near the target even at a reduced Argon partial pressure. Consequently a higher deposition rate can be achieved. Also, the local magnetic field traps and deflects the trajectory of the electrons present in the plasma to prevent it heating the substrate. However, a drawback of using magnets is that the enhance plasma cloud has a annular shape due to the a characteristic magnetic flux line near the surface of target (see figure 2.1). This results in a uneven consumption of target material in the sputtering process, which leads to the formation of a race-track on the target.

In this technique, the deposition process is not directional due to much shorter mean free-path of ejected adatoms as compared to the substrate to target distance. The ejected atoms collide multiple times before settling on the substrate. As sputtering is not a directional deposition technique it has limited application for lift-off processes.

Moreover, the DC sputtering method can not be used for the non-conducting (semiconductor or dielectric) targets. This is because the continues bombardment of ions builds up charge on the surface of the target. Consequently, sudden dendritic electric discharge processes (arcing) destabilize the plasma, resulting in an uncontrolled deposition rate. In fact, for a sufficiently strong electric discharge event, the strength of surface electric field reaches a point, at which it can produce cracks on the surface of a target material.

2.2.2 Radio-frequency (RF) magnetron sputtering

The radio-frequency (RF) magnetron sputtering technique is used to deposit the non-conducting (semiconductor or dielectric) targets. In this technique, a RF source of frequency usually $\approx 13.50\,\mathrm{MHz}$ is used to bias the target, which prevents the build up of charge on the surface of the target. This is because, in the positive half-cycle of the RF-bias, electrons are attracted to the target, while in the negative half-cycle Argon ions are attracted towards the target. Since, the Argon ions are much heavier than the electrons, the overall polarity of target (cathode) remains negative, which is preventing the arcing type electric discharge processes.

The RF sputtering method can provide a slower deposition rate and a smoother film as the plasma can be sustained at a lower partial pressure of Argon. In addition, due to the oscillatory nature of the motion of ions near the target, the formation of race-track can be significantly minimized.

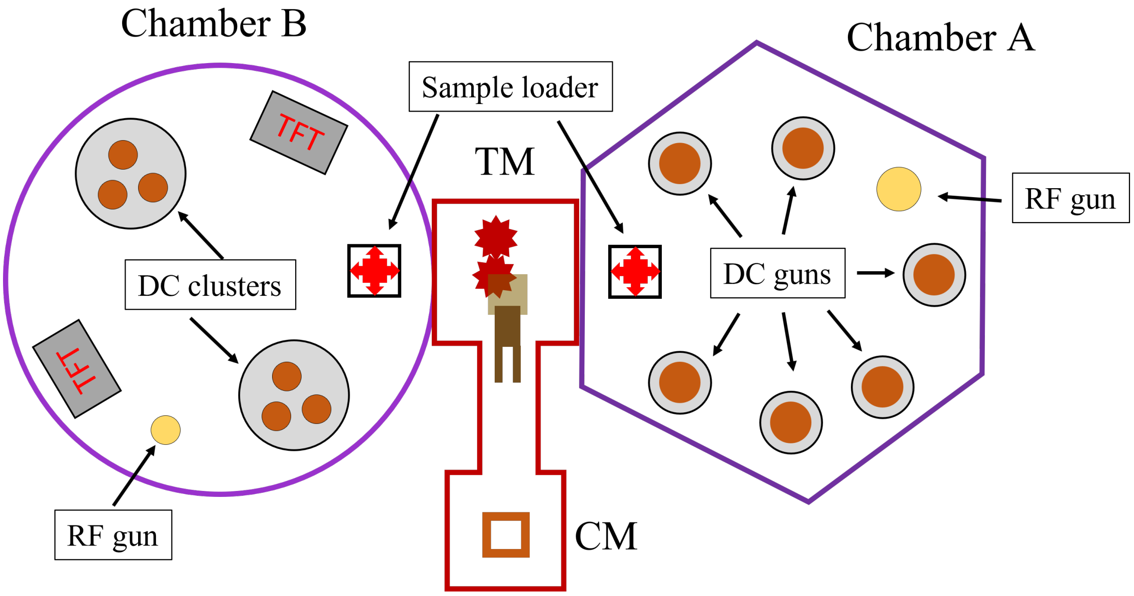

Figure 2.2: A schematic of Shamrock sputtering tool. Here the cassette module (CM), transfer module (TM), target facing target (TFT) gun and various other components are illustrated. Each module are briefly described in section 2.2.3.

In fact, the RF deposition technique can be used to deposit from metallic targets, where the lower deposition rate might be useful to improve the film quality due to the time given to atoms to migrate on the target surface.

2.2.3 The Shamrock deposition tool

A vast number of thin-films for this work were grown in the Shamrock sputtering tool, located in the class 10000 cleanroom at CRANN, TCD. A schematic of the tool is shown in figure 2.2. It is a fully automated deposition tool with two growth chambers, (chamber A and B), interconnected via a robot arm in transfer module (TM). The tool is also equipped with a cassette module (CM) which helps to load up to 16 wafers on the sample stage without compromising the vacuum of main sputtering tool.

Cassette module (CM)

It is a high vacuum load-lock chamber pumped with a turbo pump. It has a sample loading rack capable of loading up to sixteen wafers (diameter$\leq$ 6 inch).

Transfer module (CM)

It has a fully automated robotic arm to pick and park the samples from the CM and the deposition chambers A and B.

Chamber A

It is a deposition chamber with a turntable fitted with four planets. The four planets allow to process up to four samples (diameter $\leq$ 6 inch) simultaneously. The plants are also equipped with an array of permanent magnets arranged so that a uniform magnetic field ($B = 10$ mT) can be applied during the deposition process. The presence of magnetic field during the deposition helps to define the easy axis or exchange field direction in the multilayer stacks (GMR,TMR). The chamber can reach a base pressure of 3×10^{-7} Torr using a turbo molecular and a cryogenic pump. The chamber has six DC magnetron guns with an option to bias two of the guns with an RF source as well. The reactive deposition is usually performed under oxygen or nitrogen atmosphere. Typical growth rates between $0.1\,\text{Å}\,\text{s}^{-1}$ to $1\,\text{Å}\,\text{s}^{-1}$ can be achieved under normal operating conditions. The presence of turntable with planets allow to deposit up to six different materials in a sequential manner to grow multilayer stacks. The deposition process can be set into a computer-automated recipe to perform the task sequentially. The chamber also includes an ion gun to in-situ clean the samples, which is very convenient for many applications.

Chamber B

Chamber B has two DC clusters consist of three confocal DC guns. The three confocal guns allow the growth of metallic alloys through the co-sputtering deposition technique using more than one target. For example the, $\mathrm{Mn_2Ru}_x\mathrm{Ga}$ compound (this ordered alloy is the heart of the thesis) can be deposited by co-sputtering from the $\mathrm{Mn_2Ga}$ and Ru targets. The relative composition can be set by altering the power supplied to each gun. The chamber also includes two off-axis, target-facing-target (TFT), RF deposition guns where two target face each other. The TFT allows to grow dielectric materials such as MgO, AlO_x, $SrTiO_3$, SiO_2, etc., where the energy of ejected atoms and deposition rate is relatively low to promote better growth conditions. The typical pressure in the chamber is 3×10^{-8} Torr. A substrate temperature up to 500 °C can be obtained using an infrared heater. The chamber also includes a separate RF gun with local gas injection capability.

2.2.4 Trifolium Dubium deposition tool

The Trifolium Dubium (TD) is a versatile multi-technique cluster tool. It is located in the class 10000 cleanroom at CRANN, TCD. A 3D rendered image of the tool is shown in figure 2.3. It is a DCA® instrument built deposition tool, which is designed for full ultra-high vacuum (UHV) conditions. It is a highly automated deposition tool with a capability to run various inter and intra chamber deposition process with easy to use sequential routines. During the course of this thesis only SP1 and SP2 have been used to prepare a few Mn_2Ru_xGa samples.

- **Loadlock:** It has a cassette with sample rack for up to 10 wafers. The inbuilt heater allows it to bake-out the chamber at 200 °C in order to remove water vapour.

- **Central distribution chamber (CDC):** It has a fully automated robot arm to transfer the wafers into several UHV chambers. The UHV ($< 1\times10^{-11}$ Torr) of the CDC is achieved using ion and Titanium sublimation pump.

- **Sputter 1 (SP1):** It is a UHV *only metal* deposition chamber. The base pressure can reach down to 1×10^{-10} Torr. It has six guns compatible with two-inch targets, and can be arranged in a confocal manner for co-sputtering. The relative angle of confocal targets can be altered using mechanical knobs. Out of the six guns, three can be biased with RF sources for RF deposition. The position of the sample stage with respect to the gun can be altered as well. A retractable quartz crystal monitor (QCM) provides the ability to monitor the deposition rate.

- **Sputter 2 (SP2):** It is very similar to SP1 but can be used for dielectric and reactive deposition. Additionally, it is equipped with a differentially pumped residual gas analyser (RGA) to analyse the UHV quality. A target-facing-target gun is also available to deposit dielectric materials.

- **Pulsed laser deposition (PLD):** It has six target slots and is capable to handle one inch circular targets. The Quantel YG981E Nd:YAG laser generates the second, third and fourth harmonic for output wavelengths of 1064 nm, 532 nm, 355 nm, and 266 nm. The chamber includes a QCM, RGA and reflection high-energy electron diffraction (RHEED) tool.
- **Molecular beam epitaxy (MBE):** It has four high-temperature (2000 °C) effusion evaporation cells. The chamber temperature can be controlled with water cooling or liquid nitrogen. The base pressure of MBE is $< 1\times10^{-11}$ Torr. It is also equipped with RHEED and RGA.
- **X-ray photoelectron spectroscopy (XPS):** The XPS/UPS chamber uses a PHOIBOS 150 hemispherical analyser, with a 2D detector for angular resolved photoelectron spectroscopy (ARPES). It includes a monochromated X-ray source utilising Ag and Al electrodes, and a plasma discharge He UV source.

2.3 X-ray crystallography

In this thesis, the standard X-crystallography[1] techniques are used to investigate the crystal structure, grain size, defects, film thickness and density of the samples.

2.3.1 X-ray diffraction

The spacing between atoms in solid is of the order of few Angstrom, which is comparable to the wave length of X-rays. A detailed modelling of X-ray interaction involves elastic and inelastic scattering, refection, reflection, absorption, etc. In the case of solid materials the elastic scattering is the dominating interaction. Moreover,

---

[1] There are several other crystallography techniques with different kind of sources, such as electron, neutron. For each technique, matter interacts differently and hence provide different complementary measure of the properties of the sample.

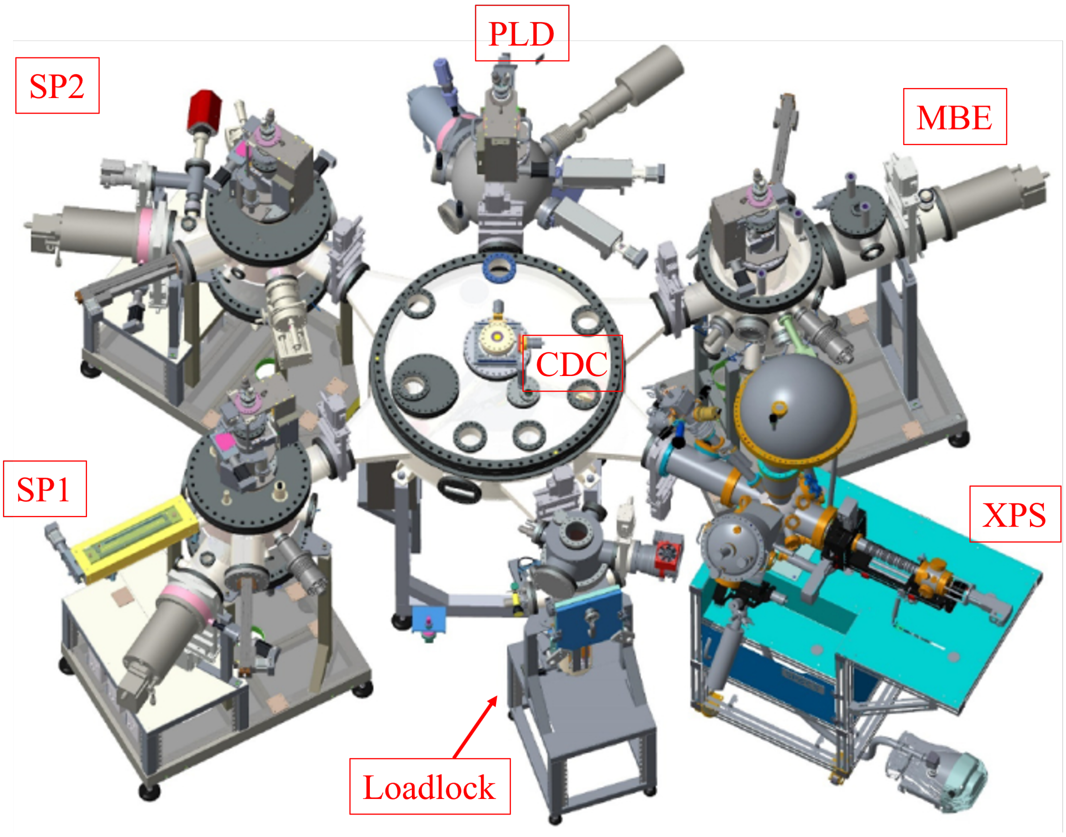

Figure 2.3: A 3D rendered image of Trifolium Dubium (TD). Some of the important component of TD such as Sputter 1 (SP1), Sputter 2 (SP2), Pulsed-laser deposition (PLD), Molecular beam epitaxy (MBE), X-ray photoelectron spectroscopy (XPS), Central distribution chamber (CDC) and Loadlock are labelled.

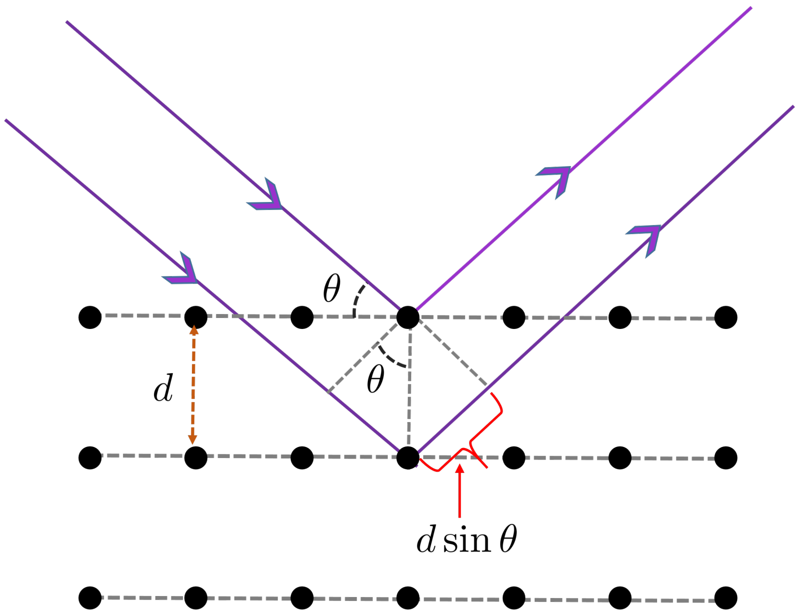

Figure 2.4: A schematic diagram of Bragg's X-ray diffraction law. A constructive interface is obtained when it satisfies the equation 2.1. Here θ is the incident angle of wave and d is the interplanar distance.

the scattering cross-section for the elastic mechanism is given by Thomson's scattering formula where scattering cross-section is inversely proportional to the particle mass. Therefore, in X-ray diffraction scattering from electrons dominates. A complete calculation of elastic scattering from each scattering centre is computationally intensive process, where the phase and direction of the scattered wave is taken into account to formalize the constructive and destructive interference of scattered waves.

However, a much simpler formalism can be established in real space using the Bragg's diffraction law, as shown in figure 2.4. When a monochromatic X-ray beam incident on the periodic lattice at an angle θ, the specularly reflected beam interferes constructively when it satisfies Bragg's condition:

$$2d \sin\theta = n\lambda \tag{2.1}$$

where, d is the interplanar distance and λ is the wave length. n is the order of diffraction which takes the integer values.

Alternatively, X-ray diffraction can also be understood via von Laue formalism. According to it, a constructive interference occurs when the change in the wave

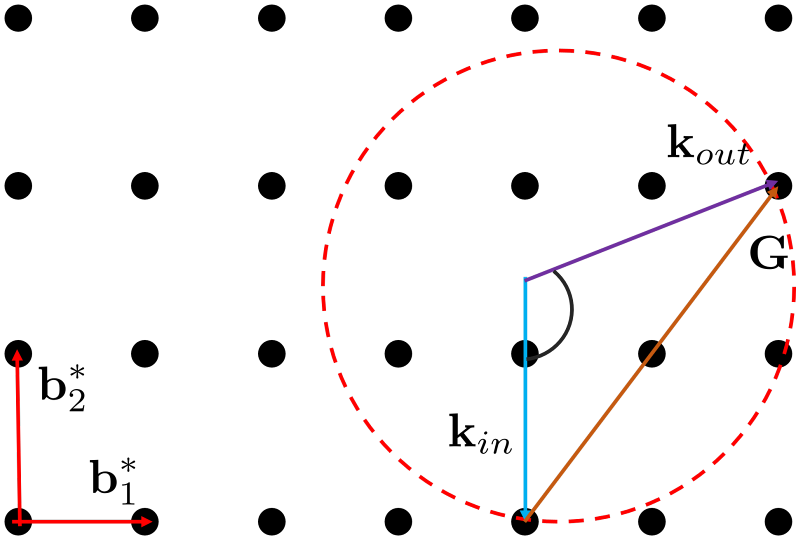

Figure 2.5: An illustration of Ewald's sphere for a two dimensional reciprocal lattice. Here, $\mathbf{k}_{in}$, $\mathbf{k}_{out}$ and $\mathbf{G}$ are the indecent wave vector, scattered wave vector and reciprocal lattice vector respectively.

vector $\mathbf{\Delta k}$ is equal to a valid reciprocal lattice vector, i.e.,

$$\mathbf{k}_{out} - \mathbf{k}_{in} = \mathbf{\Delta k} = \mathbf{G}\,, \tag{2.2}$$

where, $\mathbf{k}_{in}$, $\mathbf{k}_{out}$ and $\mathbf{G}$ are the indecent wave vector, scattered wave vector and reciprocal lattice vector respectively. For the elastic scattering mechanism $|\mathbf{k}_{out}|^2 = |\mathbf{k}_{in}|^2$, defining a sphere in the reciprocal space, called Ewald's sphere. Therefore, the diffraction from a given family of planes occurs when the corresponding point in reciprocal space lies on the Ewald's sphere, as shown in figure 2.5

Bragg's or von Laue condition is a necessary but not the sufficient condition to observe the intensity of the diffraction pattern. The intensity of the diffracted beam depends on the structure factor $S(\mathbf{G})$ and form factor $F(\mathbf{G})$ of the lattice, given by:

$$I \propto |S(\mathbf{G})|^2 \cdot |F(\mathbf{G})|^2\,. \tag{2.3}$$

The structure factor arising from the atoms occupying different lattice sites, while the form factor is given by the Fourier transform of the electronic charge distribution at the various lattice sites.

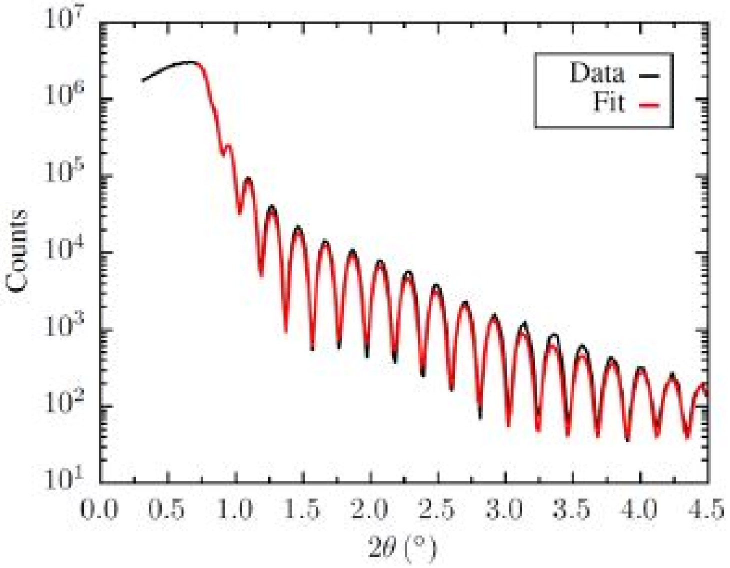

Figure 2.6: The XRR data and fit of bilayers stacks compromise of MgO(sub)/Mn_2Ru_xGa /AlO_x.

2.3.2 X-ray reflectivity

X-ray reflectivity (XRR) is used to determine the film thickness, interface roughness, density of materials in multilayer thin-film stacks. XRR relies on the total external X-rays reflection effect near the critical angle (θ_c). In this method an X-ray beam is incident on the surface at a grazing angle (θ <10 deg) and the reflected beam is studied. Below the critical angle a total reflection effect dominates. Above the critical angle, (θ_c), the X-rays penetrate the films. The X-ray beam reflects from each surface where electronic density changes. The partial reflected beams from each surface/interface interfere and form an oscillatory pattern, as shown in figure 2.6. The film thickness, density and interface roughness can be obtained by fitting the XRR data, regardless of the crystalline quality of layers. In other words, XRR can be used for polycrystalline, amorphous or single crystal samples.

2.3.3 X-ray diffractometers

For this work two X-ray diffractometers: the Philips PANalytical X'Pert (PANalytical) XRD system and Bruker D8 Discover diffractometer (Bruker) were used, see figure 2.7. The central X-ray wavelength for both the instrument is at λ =1.5405 Å (Cu K_α). A multi-strip detector capable of fast data acquisition over all 2θ range

Figure 2.7: (a) Philips PANalytical X'Pert (PANalytical) X-ray diffractometer, (b) Bruker D8 Discover diffractometer (Bruker) X-ray diffractometers.

in both the diffractometers. The PANalytical is normally used for XRR and low resolution XRD measurement while the Bruker is used for high-resolution XRD measurements. Additionally, Bruker provides a parallel incident beam while PANalytical has a divergent beam.

2.4 Micro-fabrication

In this section the methods used to fabricate micron-sized device, such as Hall bars are, discussed.

2.4.1 Optical lithography

Devices of micrometer scale are fabricated using optical lithography in the OAI$^{\text{TM}}$ Ultra-Violet (UV) mask aligner, located in the CRANN class 100 cleanroom. Clean substrate is coated with photoresist (a photo-active polymer) by rotating at a high speed on a centrifuged spinner. The thickness of the coated layer is determined by the viscosity of the photoresist and the spinner speed profile. After drying the excess solvent present in the resist, the same is exposed with UV light through a photomask. Then it is developed in a resist developer (a basic pH solution). The UV exposed area either dissolves in the solution (positive photo-tone resist) or doesn't dissolve in the developer (negative-tone resist). In my work, I have used both kinds of resist to fabricate the devices. Further, hard baking is performed depending upon the next fabrication step of the process.

2.4.2 Ion milling

The device fabrication process involves the removal of the unwanted layer(s). One of the common method is ion milling. In this method, highly energetic beam of noble gaseous (typically Argon) ions created by an ion gun, are accelerated towards the sample. The accelerated beam of ion bombards the sample and physically removes the material. Therefore, in order to achieve a desired microstructure, some parts are covered with relatively thick photoresist material, while the rest are directly exposed to the beam.

The Millatron ion milling tool is available in the SNIAM building cleanroom. It consists of a high vacuum chamber and a CCR Technology COPRA DN250 plasma beam source. A pair of Helmholtz electromagnetic coils is used to enhance the ionisation rate and the stability of plasma. An RF source ($P = 300\,\mathrm{W}$) is used to generate the plasma. The sample stage and plasma source are cooled using chilled water-based coolant. The system can be pumped using a cryogenic pump to achieve a base pressure of value 5×10^{-7} Torr. The orientation of the sample stage can be manually adjusted between 0 deg and 90 deg.

Millatron also contains a Hiden secondary ion mass spectrometry (SIMS) *end-point* detector to detected and monitor in real time the etch process.

2.4.3 Recipe for Hall bar fabrication

The following recipe was used to fabricate the Hall bars of a metallic thin-films deposited using magnetron sputtering on 10×10 mm^2 MgO substrates.

Patterning of Hall bars is a two stage process. In the first stage Hall bars are defined as per the following procedure:

1. Sonicate the sample in acetone for 5 min in order to remove the organic contamination on the sample. This is followed by a 2 min wash in isopropyl alcohol (IPA).

2. Dry the sample with dry nitrogen prior to baking the sample on the hot plate

at 100 °C. This helps to get rid of moisture present on the surface of the sample.

3. Spin-coat the negative photoresist MaN-1410 at 3000 RPM for 30 s. The approximate thickness of photoresist will be around 1 µm.
4. Pre-bake at 100 °C for 90 s.
5. Align the substrate with the designated mask on OAI$^{\mathrm{TM}}$. After that expose with UV light (λ =365 nm) for 20 s. It requires an exposure dose of around 450 mJ cm^{-2}.
6. Bake the sample for 2 min to enhance the stability of the negative photoresist.
7. Develop in ma-D 533/S for 30 s.
8. Etch the uncovered film in the Millatron at 85 deg.
9. Deposit a SiO_2 layer to planarise the surface.
10. Lift-off the photoresist and SiO_2 in acetone or 1165 remover.

After competing the first stage, a well defined Hall bars can be obtained. In the second stage electrical contacts are made, as per the following procedure:

1. Spin coat S1813 (positive) photoresist at 5000 RPM for 50 s.
2. Pre-bake at 115 °C for 2 min.
3. UV expose for 5.5 s on OAI.
4. Develop for 60 s in MF 319 developer.
5. Deposit Ti(5 nm)/Au(20 nm) in an evaporation tool (for the contact pads).
6. Lift-off by immersion in acetone with occasional gentle sonication.

A resultant Hall bar after the contact deposition and lift-off process is shown in figure 2.8

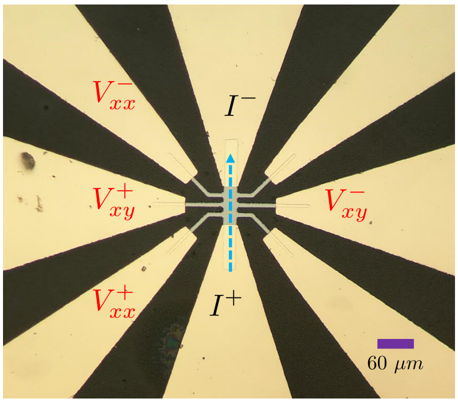

Figure 2.8: An optical image of a litho-graphically obtained Hall bar. I$^+$ and I$^-$ are the applied current electrodes. V$_{xy}^{+}$ and V$_{xy}^{-}$ are the Hall voltage electrodes whereas V$_{xx}^{+}$ and V$_{xx}^{-}$ are the electrodes used to measure the longitudinal voltage.

2.5 Magnetotransport measurement

The magnetotransport investigations of magnetic thin-films were performed using both Van der Pauw and Hall bar geometries.

2.5.1 Van der Pauw and Hall bar method

The Van der Pauw technique is an easy to use method to probe the magnetotransport properties and sheet conductivity of the sample. This is because it does not require a micro-patterning process. A uniform conducting film of preferably square shape (of any size) can be measured, provided that the area of four contact pads are much smaller than the area of sample under investigation [51, 52].

The measurement involves applying current across two contact and recording the voltage across remaining two contacts. For example if current is biased across contacts 1 and 2 while voltage is recorded across contact 3 and 4, the corresponding resistance is defined as $R_{12,34} = V_{34}/I_{12}$, as shown in figure 2.9. The sheet resistance of the sample is given by:

$$R_{\square} \equiv \frac{\rho}{t} = \frac{\pi}{\ln 2} \frac{R_{12,34} + R_{14,23}}{2} f\left(\frac{R_{12,34}}{R_{14,23}}\right); \tag{2.4}$$

where, ρ and t are the resistivity and thickness of the film respectively. f is correction factor, whih depends on the exact sample geometry.

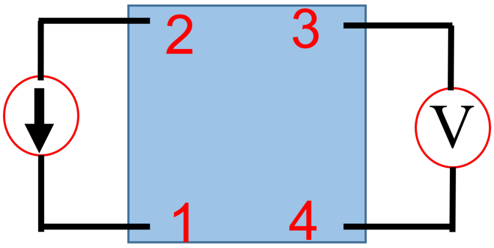

Figure 2.9: A schematic of Van der Pauw measurement configuration, with current is biased along contact 1 and 2, while voltage is measured across contact 3 and 4.

The Hall measurement of the sample can be achieved when current is biased along one of the diagonally opposite contacts and voltage is recorded along the remaining diagonally opposite contacts. The Hall resistivity can be defined as:

$$\rho_{xy} = R_{13,24}t \tag{2.5}$$

Alternately, a more accurate Hall effect and sample resistivity measurements of the films can be performed in the Hall bar geometry, shown in figure 2.8, as the current density is forced to be much homogeneous within the Hall bars.

2.5.2 Physical properties measurement system and GMW

The magneto-transport measurement of several samples were measured in the physical properties measurement (PPMS$^{\mathrm{TM}}$) system, located in CRANN, within Van der Pauw and Hall bar geometries. The PPMS is a liquid helium-cooled cryostat where the magnetic field from the superconductive solenoid can reach up to 14 T. The temperature of the sample space can be controlled between 2 K and 400 K. It is a versatile tool where a wide variety of measurements such as magneto-transport, resistivity, heat capacity, thermal transport, vibrating sample magnetometry (VSM), etc. can be easily performed. Here, the sample space is not in the direct contact with Helium vapour, rather it is thermally connected to a cooling annulus via vacuum sealed sample receptor, which makes a thermal bridge between outer wall of cooling annulus. Helium in the cooling annulus is filled through a vacuum insulated bubble formation impedance valve. The temperature of the cooling annulus, and hence sample space, is controlled by pumping on the Helium gas within the cooling

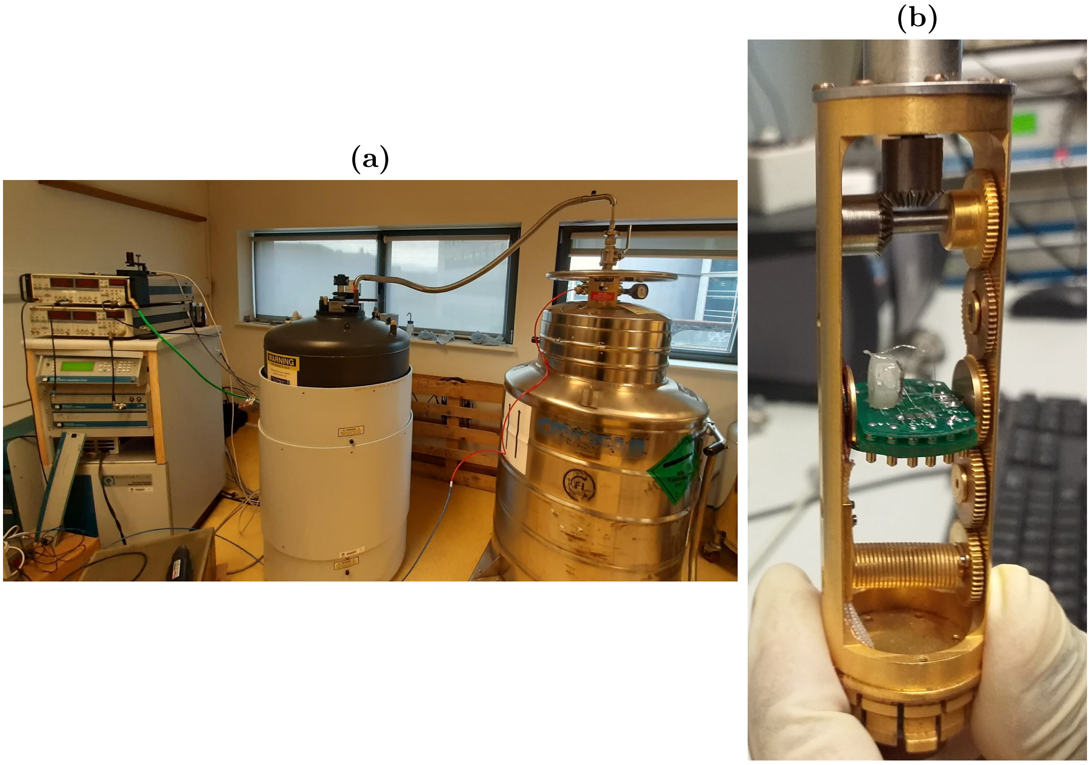

Figure 2.10: (a) A physical properties measurement system (PPMS) used for various trasnport measurement, (b) the electrical probe with single axis sample stage rotator. Note that here sample is mounted perpendicular to the stage in order to access the field rotation within the sample's plane.

annulus using a scroll pump.

An automated sample rotator stage (see figure 2.10b) with angular resolution of 0.01 deg, is used to rotate the sample in various planes, in order to investigate the complete picture of the quasi-static dynamics of magnetization (see section 4.6). The magnetotransport properties of samples are also studied using a GMW$^{\mathrm{R}}$ electromagnet (Model 5403), see figure 2.11. Here, a magnetic field of magnitude up to 2 T can be achieved. The strength of the magnetic field is measured using a Lakeshore Gaussmeter. During this work, the GMW instrument is mostly used for the room temperature Van der Pauw and first order reversal curves (FORC) measurements. During the FORC measurement, a magnetic field controled resolution of 5 mT is used.

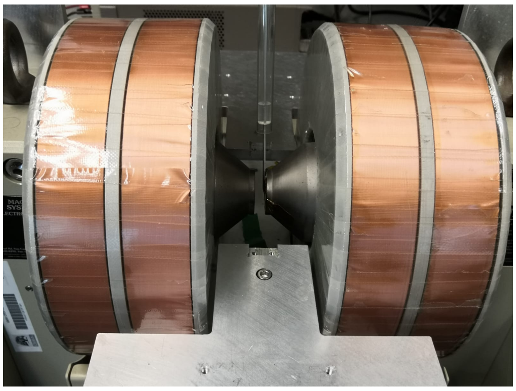

Figure 2.11: The GMW electromagnet tool (located in CRANN). It is utilized to measure magnetotransport properties of samples at room temperature. The maximum obtainable magnetic field is 2 T.

2.6 SQUID magnetometer

Superconducting QUantum Interference Device (SQUID) magnetometries are some of the most sensitive instruments to measure the absolute magnetic moment of a sample, with a sensitivity of $< 10^{-11}$ Am^2 in DC and can reach to a value of 10^{-12} Am^2 as an AC magnetometer. The governing principle behind the SQUID is the Josephson junction effect. The heart of the SQUID is a superconducting loop with RF bias one Josephson junction where current through the junction is influneced by the variable magnetic flux passing through the loop. When a magnetic sample is vibrating along the z-axis, the change in flux is picked up using a superconducting pick-up coil (second order gradiometer). A typical response curve of the pickup coil is shown in figure 2.12. The moment of the sample can be evaluated by fitting the response curve.

In this work the magnetic moment of the samples is measured using the Quantum Design Magnetic Property Measurement System (MPMS) SQUID system (located in SNIAM building) with an Evercool option. A maximum magnetic field of magnitude 5 T can be used. The sample temperature achievable is between 1.8 K and 400 K, without a sample space oven.

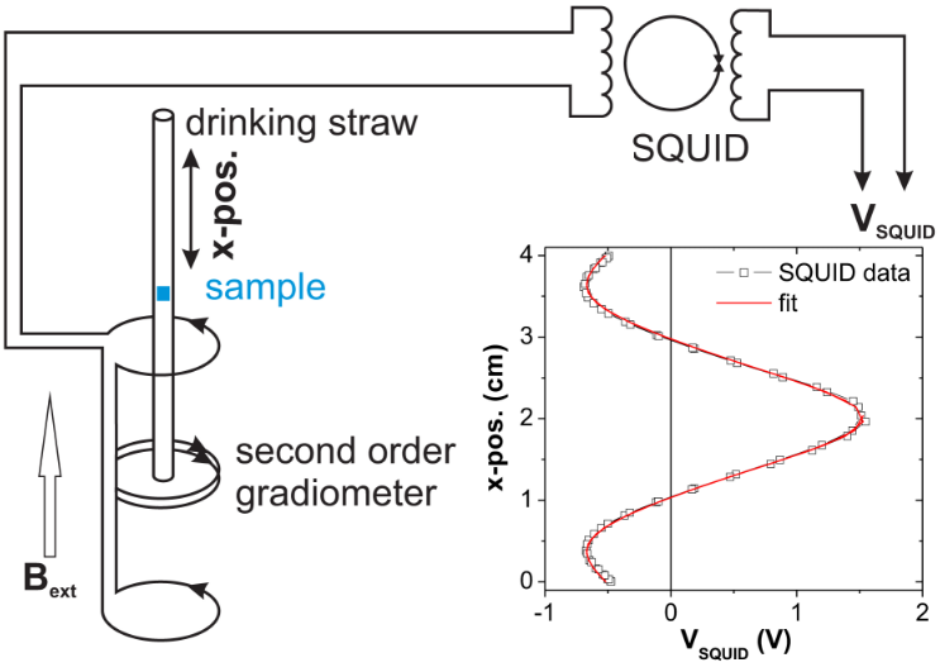

Figure 2.12: Schematic of second order gradiometer (pick-up coil) of SQUID, inset shows a typical response curve of second order gradiometer as a function of sample position (z). The picture is after Buchner *et al.* [11].

2.7 PCAR measurements

PCAR measurements are performed using two-point differential conductance ($\mathrm{d}I/\mathrm{d}V$) detection across a metal/superconductor (NM/SC) junction. ($\mathrm{d}I/\mathrm{d}V$) curve is obtained by modulating at very low frequency ($f \approx 0.5\,\mathrm{Hz}$) triangular waveform of the DC bias, of a relatively small amplitude AC carrier signal ($f \approx 1.23\,\mathrm{kHz}$). The resultant current due to the DC bias V and the small AC bias $v = v_0 \sin(\omega t)$ can be written as,

$$I(V+v) \approx I(V) + \frac{\mathrm{d}I}{\mathrm{d}V} v_0 \sin(\omega t)\,. \tag{2.6}$$

The modulated signal waveform is fed across the NM/SC junction and the output current is passed through the current pre-amplifier (SR570), where it is amplified with band pass filtering (300 Hz - 3 kHz, 6 dB/octave). The amplified signal is then recorded by a lock-in-amplifier (LIA), synchronised with the DC bias function generator TG102. The data is first temporally stored in the buffer memory of one of the LIAs for the upward trend of the triangular waveform. A schematic of the acquisition electronics is shown in Figure 2.13. In order to record the other half of waveform, the TTL signal from TG102 generator is delayed using an HP 4284A

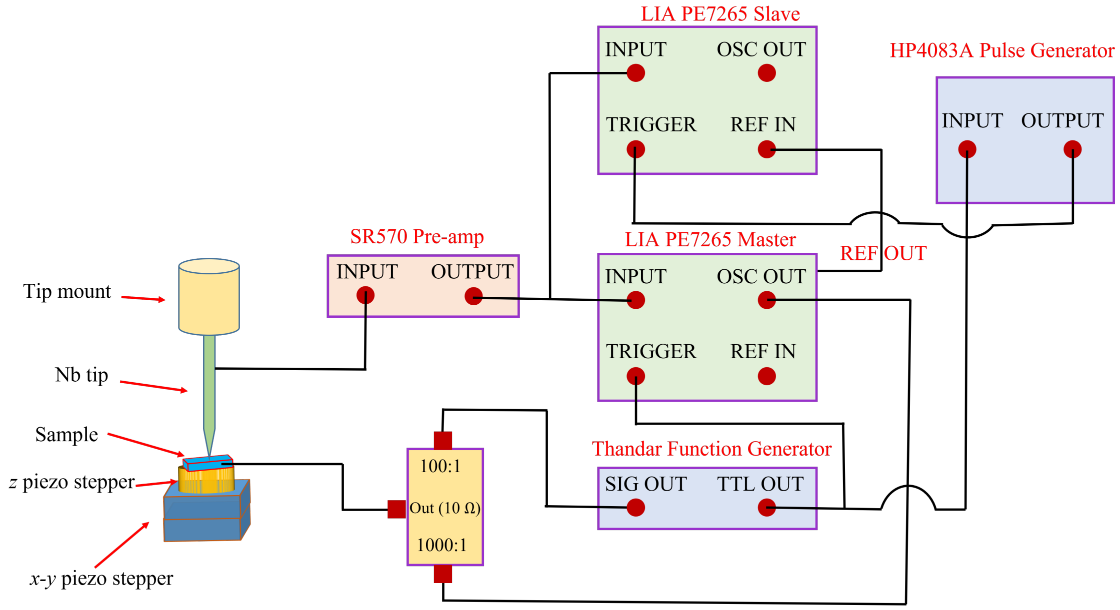

Figure 2.13: A schematic illustration of the PCAR experimental setup and the electronic measurements circuit. Triangular quasi DC signal from Thandar function generator is modulated with a sinusoidal AC signal (OSC out of LIA) using a voltage divider. A slave and master LIA is used to record the data in for the full waveform. The details of measurement methodology are discussed in the main text.

waveform generator, so that a second 'slave' LIA can be triggered for the second half of triangular waveform. Hence, with this setup two LIAs can acquire the data concurrently on both side of the triangular DC bias wave form, which helps to monitor the PCAR signal in the real time, with a cadence of 2 Hz. The real time measurement of differential conductance helps to determine any perturbation in the specta, including perturbations due to contact thermal and field drift.

Most of the PCAR measurements are performed in a Quantum Design physical property measurements system (PPMS). Figure 2.14 shows an image of the actual PCAR probe. The sample space of the probe is shown in figure 2.15 . The sample is mounted on a set of piezo stepper stages. Three different steppers can easily manipulate the sample position on all three axes (x, y, and z). A mechanically sharpen Niobium (Nb) tip is used to make SC/NM junctions on the fly. Niobium has critical temperature (T_c) of the value of 9.2 K. A Cernox$^{\text{TM}}$ temperature sensor is mounted just underneath the sample stage to monitor the temperature of the sample. The PCAR data is flittered and fitted under modified-BTK model using programmes written in Mathcad$^{\text{TM}}$. The fitting includes a dynamically optimized non-linear re-

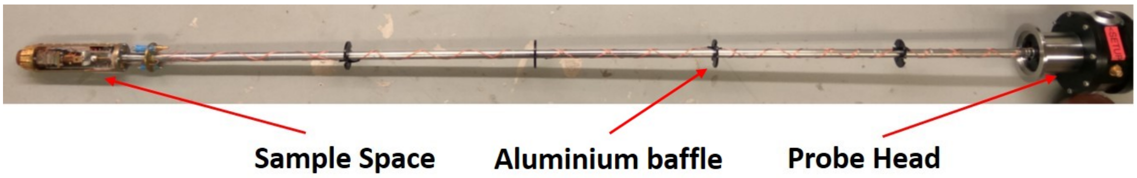

Figure 2.14: Picture of the wired PCAR probe used in the PPMS system. The bottom of probe is the sample space (described in Figure 2.15) and at the top of the probe is the probe head, where all the cables connect to the external of the electronics setup (Figure 2.13). The four aluminium baffles are used to reduce the amount of infrared radiation received at the bottom of the probe.

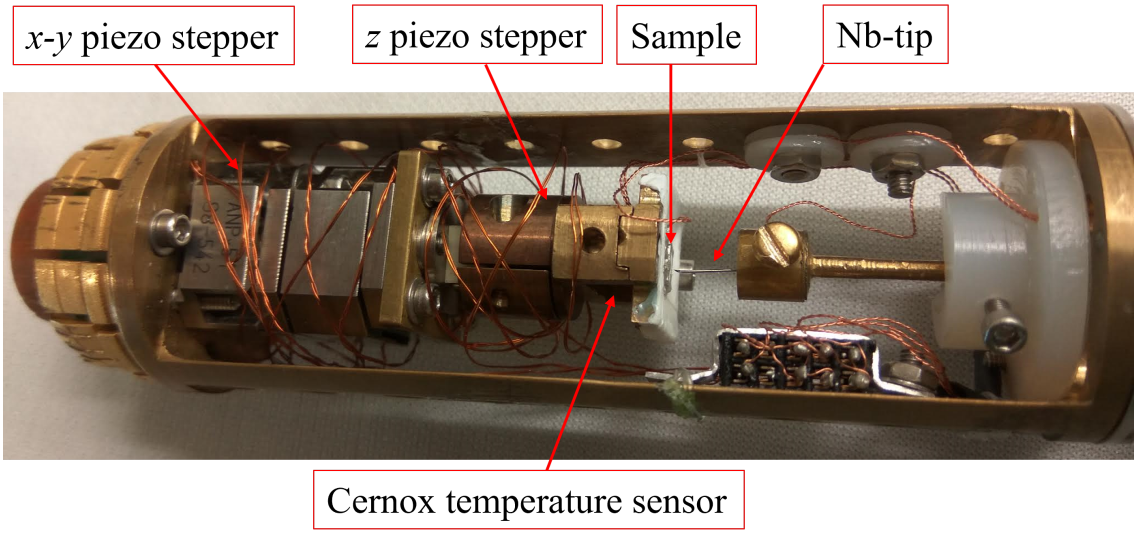

Figure 2.15: Picture of PCAR sample space. Few important components are indicated, namely, Nb tip, piezo-steppers/scanner and Cernox sensor.

gression algorithm. The more details about the fitting can be seen in section 3.4.

3

Spin polarization study of Mn_yRu_xGa thin-film

3.1 Introduction

Materials with high Fermi level spin polarization play a vital role in various spintronics applications and phenomena, such as in giant magneto-resistance (GMR) [53, 54], tunnel magneto-resistance (TMR) [2, 3], magnetic random access memory (MRAM) [55], spin-transfer torque magnetic random access memory (STT-MRAM) [44, 45, 56] and various form of spin dependent computing [57, 58]. The performance of these spintronics devices highly depends on the degree of spin polarization of the material of choice. Therefore, a material with 100% spin polarization is ideal for advanced spin-based devices. One such type of materials is the half-metal, where band structure for one spin direction is metallic while insulator or semiconductor for the other spin direction[1]. There are direct consequences of half-metallicity in spintronics applications. For example the electrical transport solely takes place by charge carriers of one spin direction, thereby huge improvement in the efficiency of spintronics devices comes about[2]. Additionally, magnetic moment per unit cell for a half-metal is an integral number[3].

Realizing, a ideal half-metal in practice is elusive due to imperfect stoichiometry, disorder [61], impurities, finite spin-mixing conductance[4] [62], thermal excitations [63],

---

[1] The concept of two-spin channel is valid as long as the electron spin is a good quantum number. In a situation where spin-orbit interaction is larger than exchange energy, the description of two spin channel fail.

[2] GMR/TMR device made using ideal half-metal should, theoretically, show infinite GMR/TMR ratio.

[3] This is the basis for standard Slater–Pauling rule to characterize the half-metallicity in a metallic alloy [59, 60].

[4] Presence of spin-orbit interaction leads to spin-mixing conductance.

pressure [64], etc. Therefore, only few half-metallic[5] examples are available, such as some Heusler alloy [65, 66], Perovskite [67], spinel [68], transition metal oxides[6] [71], etc.

Most of the half-metals reported are ferromagnets, which have the major drawback of large intrinsic net magnetic moment. Consequently, the associated long-range dipolar interactions hinder the performance of multilayer structures or nearby bits and devices. Therefore, development of a new class of materials started, where blend of zero magnetic moment and high spin polarization are present. One such material is the antiferromagnetic half metal (AFHM), first proposed in 1995 by van Leuken and de Groot [49]. However, an antiferromagnet (AF) with half-metallic property is not compatible because two or more sublattices of AF are chemically and crystallographically equivalent. Hence, AF poses rotational symmetry and zero spin polarization. In the contrast, for a compensated ferrimagnetic half-metal (CFHM), presence of crystallographically inequivalent magnetic sublattices, which are antiferromagnetically coupled, possess interesting possibilities, including half-metallicity. Thus, CFHM facilitates the possibility of next generation spintronics devices. There have been many such materials theoretically proposed, especially Heusler alloy [72, 73, 74], but realizing CFHM remains elusive due to the unstable structure, presence of zero gap at the Fermi level and loss of magnetic properties. However, the first experimental realization of CFML was achieved by Kurt *et.al.* in 2014 with Mn_2Ru_xGa (MRG) thin-films [22].

MRG crystallizes in the near cubic inverse Heusler XA structure, space group $F\bar{4}3m$, where Mn occupies two inequivalent sublattices positions, 4a (Mn^{4a}) and 4c (Mn^{4c}), as shown in figure 3.1. Magnetic moments of 4a and 4c sublattices are antiferromagnetically coupled, while those on the same sites are ferromagnetically coupled. The details of MRG and their properties are presented in chapter 1.

One of the striking properties of MRG is the high degree of spin polarization at the Fermi level. However, further studies have suggested that in such samples,

---

[5] Technically the experimental evidence of true ∼100% Fermi level spin polarization has never been realized, except in rutile CrO_2 ($P \sim 96\%$).

[6] CrO_2 is a famous ferromagnetic half-metal which has rutile structure. Even though an experimental evidence of more than 96% spin-polarization at low temperature has been achieved in this material [69], the nature of its metastable phase in ambient atmospheric conditions limit its application. Its surface spontaneously decomposes to the more stable phase of Cr_2O_3 [70].

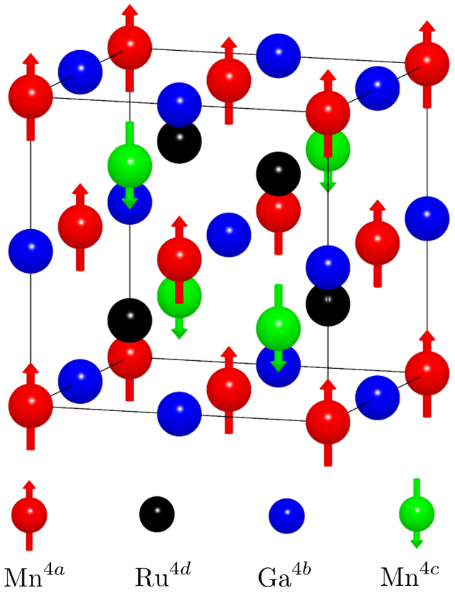

Figure 3.1: Crystal structure of MRG. It consist of four interpenetrating fcc lattice, where Mn^{4a} (red) occupy 4a while Mn^{4c} (green) 4c Wyckoff positions. Also, Ru (black) and Ga (blue) occupy 4d and 4b Wyckoff positions respectively. Moment at Mn^{4a} and Mn^{4c} antiferromagnetic coupled with each other. In this case both 4c and 4d sites are fully occupied by Mn and Ru atoms respectively.

the Fermi level actually lies below the spin gap [50]. A possibility to bring the Fermi level in the gap arises by carefully tuning the Mn-Ga and/or Mn-Ru relative concentration. Altering the relative concentration, changes the electronic pressure within the MRG unit cell, which eventually leads a shift of the Fermi level.

In this chapter a further insight into half-metallicity is pursued by altering stoichiometry and disorder of $\mathrm{Mn_yRu}_x\mathrm{Ga}$, where $1.2 \leq\ y \leq\ 2.6$ and $x = 0.5, 0.7$ and 0.9. The chapter begins with the samples' preparation and various measurements techniques used to characterize the samples. Then, structural, magnetic and magnetotransport properties are discussed before presenting the spin-polarization investigation. The spin-polarization of MRG samples was evaluated using point contact Andreev reflection (PCAR) spectroscopy. The aim of this study is to identify the appropriate stoichiometry of $\mathrm{Mn_yRu}_x\mathrm{Ga}$, which shows optimal desirable properties.

3.2 Methodology

A series of epitaxial thin films of varying Mn and Ru ratios in $\mathrm{Mn_yRu}_x\mathrm{Ga}$, with $1.6 \leq \ y \leq \ 2.6$ and $x = 0.5, 0.7$ and 0.9, were prepared using DC magnetron sputtering system on a 10×10 mm^2 MgO (100) substrate. All the films were co-sputtered under an inert environment (Argon gas) from $\mathrm{Mn_3Ga}$, $\mathrm{Mn_22Ga}$ and Ru targets onto the substrate maintained at 350 °C. The required stoichiometry ratio of MRG is realized by a careful calibration of the sputtering parameters. All the films were further capped with ∼3 nm of amorphous AlO_x in order to prevent excessive oxidation.

The structural properties of MRG films were characterized using the standard X-ray crystallographic techniques. Symmetric $2\theta - \theta$ scan was realized in Bruker-D8 high resolution X-ray diffractometer of wave length 154.06 pm to evaluate the out-of-plane lattice parameters, c, of the MRG. In-plane lattice constants, a and b, of the film were determined using reciprocal space mapping (RSM), where the scan is performed around the MgO (113)[7] peak. Additionally, the scan is repeated around the other intense peak of MgO (206). The thickness and density of the films were determined using low-angle X-ray reflectivity (XRR) measurements, performed with a Panalytical X'Pert Pro diffractometer. Anomalous Hall effect (AHE) measurement were performed in a Quantum Design Physical Property Measurement System (PPMS) up to a field of 14 T. AHE and longitudinal resistivity of MRG were realized in four-point Van der Pauw measurement geometry.

PCAR spectroscopy was performed to determine the Fermi-level spin-polarization of MRG, using a mechanically-sharpened superconducting Nb-tip in the PPMS system. The $x, y,$ and z motion of the sample are positioned using three precisely controlled Attocube™ piezo-steppers/scanners. A large number of differential conductance spectra were recorded to achieve a statistically stable signal. The PCAR spectra were analyzed by fitting the data using a modified Blonder-Tinkham-Klapwijkv (m-BTK) model. More details can be found in chapter 1.

The magnetic moments of the MRG samples were determined in a 5 T Quantum Design's MPMS SQUID magnetometer.

---

[7] MgO (113) reflection is parallel to the MgO (204) peak.

3.3 Structural, magnetic and magnetotransport properties of $\mathrm{Mn_yRu}_x\mathrm{Ga}$

A series of $\mathrm{Mn_yRu}_x\mathrm{Ga}$ samples with varying y and x were investigated within a structural, magnetic and magnetotransport study. A complete list of samples are shown in table 3.1. These samples are the subset of sample $\mathrm{Mn_yRu}_x\mathrm{Ga}$ so that their magnetic compensation point lie above 0 K.

Series-1	**Series-2**	**Series-3**
$Mn_{2.2}Ru_{0.5}Ga$	$Mn_{2.0}Ru_{0.7}Ga$	$Mn_{1.8}Ru_{0.9}Ga$
$Mn_{2.4}Ru_{0.5}Ga$	$Mn_{2.2}Ru_{0.7}Ga$	$Mn_{2.0}Ru_{0.9}Ga$
$Mn_{2.6}Ru_{0.5}Ga$	$Mn_{2.4}Ru_{0.7}Ga$	$Mn_{2.2}Ru_{0.9}Ga$

Table 3.1: List of $\mathrm{Mn_yRu}_x\mathrm{Ga}$ thin-film for various x and y, deposited using magnetron sputtering techniques.

X-ray diffraction patterns for $\mathrm{Mn_yRu}_x\mathrm{Ga}$ are shown in figure 3.2. The presence of two strong peaks for MRG (002) and MRG (004) in all samples suggest the growth of a highly textured film in the inverse XA crystal structure. The out-of-plane lattice constant c has value around 605 pm, as obtained from 2θ value of MRG (004) peak (see table 3.2). A slight change in c for different MRG samples is due to change in the thickness of films. Furthermore, the value of in-plane lattice constant (a) of value around 596 pm was determined from RSM scans performed about MRG (206) peaks. The value of in-plane parameter suggests that the growth direction for all the film is along the diagonal of MgO substrate ($\sqrt{2}a_{\mathrm{MgO}} = 596.6\,\mathrm{pm}$). Therefore, it confirms a tetragonal distortion ($[c-a]/a$) of value around 1.5%, in the films. The presence of tetragonal distortion leads to a strong out-of-plane anisotropy in the films, which determines several interesting properties of MRG [75, 76, 77, 18]. The relative intensity of the (002) and (004) reflections provides the information about the degree of order in the film. A higher value of (002)/(004) suggests a less ordered film. The summary of these ratios is listed in table 3.2. The values suggest that order parameter for Ru = 0.5 remains constant for all Mn stoichiometry. However, the order parameter falls as the Ru amount increases in the unit cell, with further possibility of improvement by increasing the Mn content.

The values of films' thickness and density were determined by XRR measurements. The average thickness of the films is around 50 nm.

The magnetic compensation temperatures (T_{comp}) of the samples were determined by measuring the temperature evaluation of perpendicular magnetic moment using SQUID magnetometer (see figure 3.3). The measurement begins by saturating the sample with 5 T magnetic field at appropriate temperature range (away from compensation point), then temperature scans are performed at zero magnetic field to avoid the strong paramagnetic contribution of the MgO substrates[8]. The magnetization measurements for the whole series of samples are shown in figure 3.3. A summary of magnetic magnetic properties is presented in table 3.3. Here, the Curie temperature was evaluated by fitting the data under mean field theory, as discussed by Siewierska *et al.* [78]. It is evident that a desirable range of compensation points, from well below the room temperature up to well above the room temperature, are attainable by tuning the Mn and Ru concentration, highlighting their adaptability for various spintronics applications.

	a (pm)	**c** (pm)	$\frac{\mathbf{c-a}}{\mathbf{a}} \times 100$	$\frac{\mathbf{I(002)}}{\mathbf{I(004)}}$	**Density** (kg/m^3)
$Mn_{2.2}Ru_{0.5}Ga$	597	605	1.3	0.05	8003
$Mn_{2.4}Ru_{0.5}Ga$	596	604	1.3	0.04	8135
$Mn_{2.6}Ru_{0.5}Ga$	595	604	1.5	0.05	7840
$Mn_{2.0}Ru_{0.7}Ga$	598	605	1.2	0.10	8293
$Mn_{2.2}Ru_{0.7}Ga$	596	605	1.5	0.09	8365
$Mn_{2.4}Ru_{0.7}Ga$	596	606	1.7	0.09	8359
$Mn_{1.8}Ru_{0.9}Ga$	596	608	2.0	0.29	8513
$Mn_{2.0}Ru_{0.9}Ga$	596	606	1.7	0.18	8496
$Mn_{2.2}Ru_{0.9}Ga$	597	607	1.7	0.11	8496

Table 3.2: Table of various parameters of Mn_yRu_xGa. a and c are the in-plane and out-of-plane lattice constants respectively, $\frac{I(002)}{I(004)}$ provides a degree of order parameter, $\frac{c-a}{a} \times 100$ is the substrate induced out-of-plane strain, and finally density, as obtained from the XRR fit (total internal reflection angle).

An increment of T_{comp} is observed as Mn concentration for a given Ru concentration increase. This is attributed to the fact that the excess Mn occupy the Mn^{4c} sites, which leads to increased moment on the Mn^{4c} site. Detail understanding can be achieved using model shown in figure 3.4. A previous report of site-specific mag-

---

[8] MgO has strong paramagnetic contribution below 100 K. This is due to the presence of traces of Fe atoms

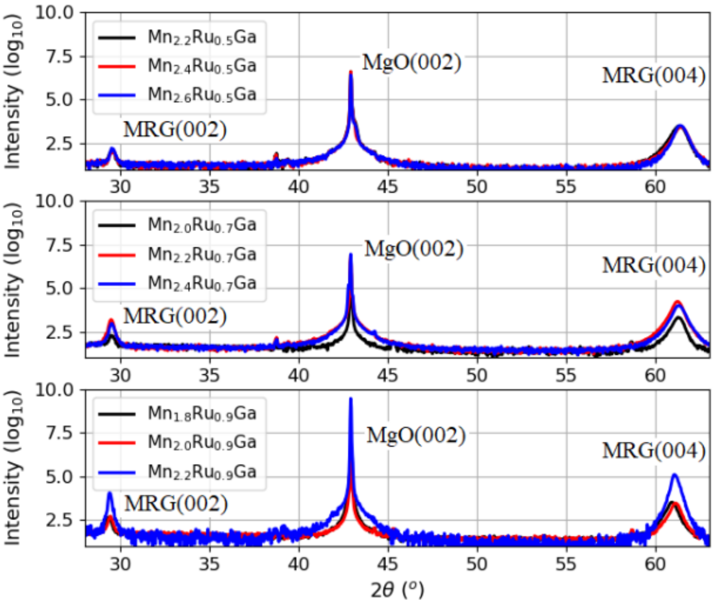

Figure 3.2: XRD patterns for Mn_yRu_xGa for various values of x and y. The top panel corresponds to $x = 0.5$, the middle and bottom for $x = 0.7$ and $x = 0.9$ respectively. Peaks of Mn_yRu_xGa (002) and (004) are clearly labeled along with the MgO substrate (002) peak. This work is also included in Siewierska's Ph.D. thesis [12].

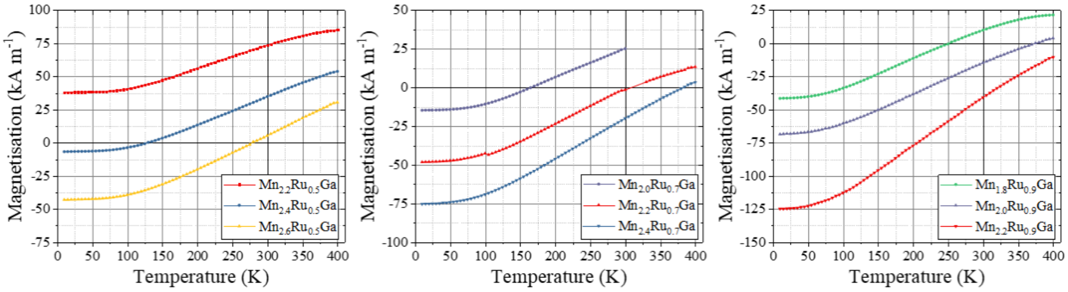

Figure 3.3: Magnetization vs temperature of Mn_yRu_xGa for various value for x and y. The compensation temperature is obtained by finding the crossings with $M = 0$ axis. This work is also included in Siewierska's Ph.D. thesis [12].

	$\mathbf{M_0^{Net}}$ (kA/m)	$\mathbf{M_0^{Net}}$ (μ_B/Mn)	T_{comp} (K)	$\mathbf{T}_C$ (K)
$Mn_{2.2}Ru_{0.5}Ga$	34	0.20	-	550
$Mn_{2.4}Ru_{0.5}Ga$	6	0.03	130	577
$Mn_{2.6}Ru_{0.5}Ga$	38	0.22	278	592
$Mn_{2.0}Ru_{0.7}Ga$	13	0.08	165	530
$Mn_{2.2}Ru_{0.7}Ga$	43	0.25	311	543
$Mn_{2.4}Ru_{0.7}Ga$	67	0.39	381	494
$Mn_{1.8}Ru_{0.9}Ga$	36	0.65	436	491
$Mn_{2.0}Ru_{0.9}Ga$	61	0.35	375	513
$Mn_{2.2}Ru_{0.9}Ga$	111	0.65	436	491

Table 3.3: Table for various parameters of Mn_yRu_xGa. M_0^{Net} is the net magnetic moment as obtained by SQUID both in kA/m and μ_B/Mn unit, T_{comp} is the compensation temperature and T_C is the Curie temperature.

netic moments in MRG suggests that the moment of Mn^{4c} changes as temperature varies, whereas the moment of Mn^{4a} remains almost constant [10]. Therefore, T_{comp} of MRG can be altered by the occupancy of Mn atoms on the different sub-lattices. For example, if excess Mn is added to the Mn^{4a} site, T_{comp} of the sample shifts to lower temperatures (figure 3.4(a)). On the other hand, if it occupies the Mn^{4c} site, T_{comp} increases. A summary of the consequences of adding and removing Mn in Mn_yRu_xGa and its effect on T_{comp} are shown in Table 3.4.

Mn concentration	**Moment**	$\mathbf{T_{comp}}$
Adding Mn^{4a}	increase	decrease
Removing Mn^{4a}	decrease	increase
Adding Mn^{4c}	increase	increase
Removing Mn^{4c}	decrease	decrease

Table 3.4: A summary of the effect of the adding or removing Mn atoms from the different sublattices of Mn_yRu_xGa for a given Ru values and its impact on the moment, and T_{comp}.

Another crucial property of MRG is the presence of large anomalous Hall coefficient. AHE in MRG is proportional to the vertical component of moment of Mn^{4c} sites, rather than the total magnetic moment. This is because bands at the Fermi level are mostly populated by Mn^{4c} [76, 79]. Thus AHE in MRG can be written as;

$$V_{xy} \propto M^{4c}\cos(\theta) \tag{3.1}$$

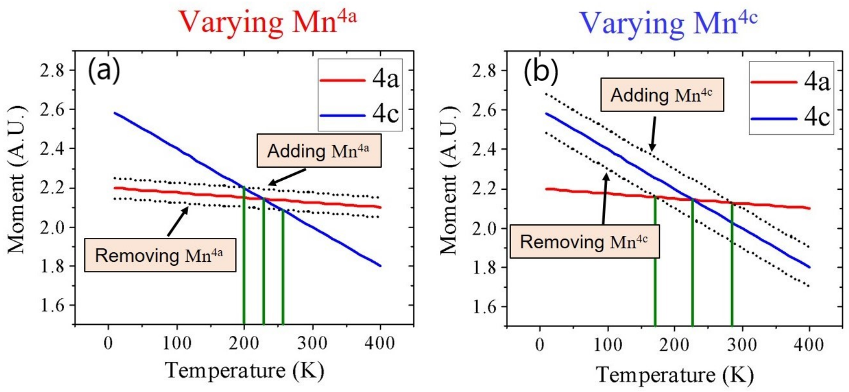

Figure 3.4: An illustration of the effect of Mn doping in $\mathrm{Mn_yRu}_x\mathrm{Ga}$. (a) If Mn is added (removed) to Mn^{4a} site, moments increase (decrease), T_{comp} shifts to lower (higher) temperature. (b) Mn is added (removed) to Mn^{4c} site, moments increase (decrease), T_{comp} shifts to higher (lower) temperature.

where, θ is the polar angle between M^{4c} and easy axis. The detail understanding of AHE in MRG can be illustrated by the model shown in figure 3.5. The figure illustrates the Mn^{4a} and Mn^{4c} sublattice moment along with the net magnetic moment M^{net}, when an applied magnetic field $\mu_0 H$ is projected along the easy axis of MRG [76]. Below the compensation temperature (T_{comp}), the moment of Mn^{4c} (black arrow) is larger than Mn^{4a} (green arrow) and M^{net} (red arrow) is parallel to the Mn^{4c}. At T_{comp}, M^{net} is zero but the direction of sublattice moments have not changed with respect to the $\mu_0 H$. Above T_{comp}, Mn^{4c} reverses its direction (provided $\mu_0 H$ exceeds the coercive field), while M^{net} follows the direction of $\mu_0 H$. Since, the direction of spin polarization is governed by the direction of moment of Mn^{4c} sublattice, the reversal of its direction above and below the compensation point causes the reversal of the sign of AHE signal (V_{xy}). As an example, the change in sign of AHE signal, above and below the compensation in $\mathrm{Mn_{2.6}Ru_{0.5}Ga}$ sample, measured using Van der Pauw method, is shown in figure 3.6a. A finite AHE signal at the compensation point also suggests that AHE in MRG is not given by M^{net}, rather it is dictated by M^{4c}. The anisotropy field, $H_K = 2H_{\mathrm{eff}}/M^{\mathrm{net}}$, at the compensation temperature is high, exceeding more than 14 T due to vanishing net moment, $\mathrm{M}^{\mathrm{net}}$.

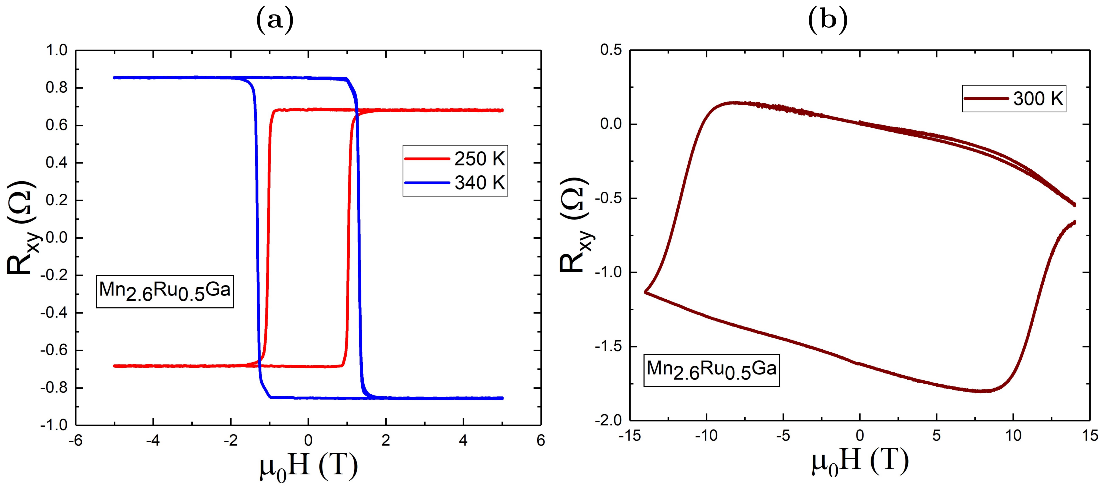

Figure 3.6: AHE measurement on $Mn_{2.6}Ru_{0.5}Ga$ using van der Pauw method, (a) reversal of Hall signal above and below the compensation point is due to change in the direction of moment of Mn^{4c}, as disused by model shown in figure 3.5 , (b) AHE measurement on $Mn_{2.6}Ru_{0.5}Ga$ at 300 K, near compensation temperature, highlighting the presence of huge coercivity ($H_c > 14$T).

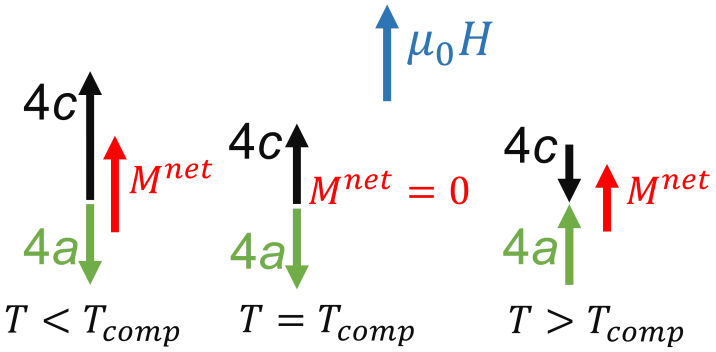

Figure 3.5: An illustration of the two-sublattice macrospin model to understand the magnetotransport properties of MRG in the presence of applied magnetic field $\mu_0 H$ directed along the easy axis of MRG. Below (above) T_{comp} the sublattice moment Mn^{4c} (black arrow) is parallel (antiparallel) to M^{net} (red arrow).

Furthermore, a comparison between magnetization and AHE is shown in figure 3.7. The in-plane (IP) and out-of-plane (OOP) magnetic moment of MRG were measured at 300 K in a SQUID magnetometer. A four point Van der Pauw method was utilized to measured the AHE at 300 K for low magnetic fields (using GMW) and high magnetic fields (using PPMS). The OOP magnetization has two step switching, first a soft component switches at lower field and second hard component, which switches at field values matching with the coercivity of corresponding AHE. The soft component is attributed to the noncolinearity of $4a$ and $4c$ sites, arising due disorder and interstitial occupancy of access Mn atoms. In order to understand it in details, consider the ideal unit cell of $\mathrm{Mn_2Ru_{0.5}Ga}$, where, Mn^{4a}, Ga^{4b} and Mn^{4c} have 100% occupancy at $4a$, $4b$ and $4c$ Wyckoff positions. On the other hand Ru^{4d} has occupancy of 50% on the $4d$ sites (see figure 3.1). However, it has been reported that vacancies at $4d$ sites are filled by the Mn atoms in films prepared by sputtering techniques [78]. With excess Mn in MRG, a further reduction in vacancies occurs, where Mn atoms occupy/replace $4d$ and $4b$ sites. Therefore, Mn^{4c} experiences competitive positive and negative exchange interaction with neighboring Mn atoms occupying the $4d$ and $4b$ sites. This competitive exchange interaction leads to a noncolinear ferrimagnetic state. Consequently, a few degree of deviation of the M^{4c} from the easy (c) axis is reported, whereas, a deviation of up to 40 deg for M^{net} has been reported in zero applied magnetic field near compensation point [78]. Thus the noncolinearity of M^{net} leads to easy cone anisotropy state, whereas M^{4c} has approximately uniaxial easy axis state. Additionally, an increase in the Mn and Ru concentration enhances the noncolinearity due to a reduction of the exchange constants J^{ac} and J^{cc}.

Thus the noncolinearity of M^{net} accounts for the two-step magnetic hysteresis loop of figure 3.7.

3.4 Spin polarization of $\mathrm{Mn_yRu}_x\mathrm{Ga}$

PCAR is a very well establish experimental technique to measure the transport spin polarization of ferromagnetic and ferrimagnetic samples. The value of transport spin polarization provide a true measure of polarization of charge/spin carrier for spintronics applications.

PCAR spectra on the series of $\mathrm{Mn_yRu}_x\mathrm{Ga}$ samples were measured in a PPMS system, as discussed in section 3.2. Figure 3.8 and 3.9 show the measured spectra and corresponding m-BTK fits. The modified BTK model takes into account the proximity effect (Δ_1), the effective barrier strength (Z), the spin polarization (P) and the electronic temperature (T_e), while estimating the spectrum. All PCAR spectra were normalized using background data (normal conductance, G_N) collected after quenching the superconducting tip, Nb, above its critical temperature ($T_c \approx 9.2$K).

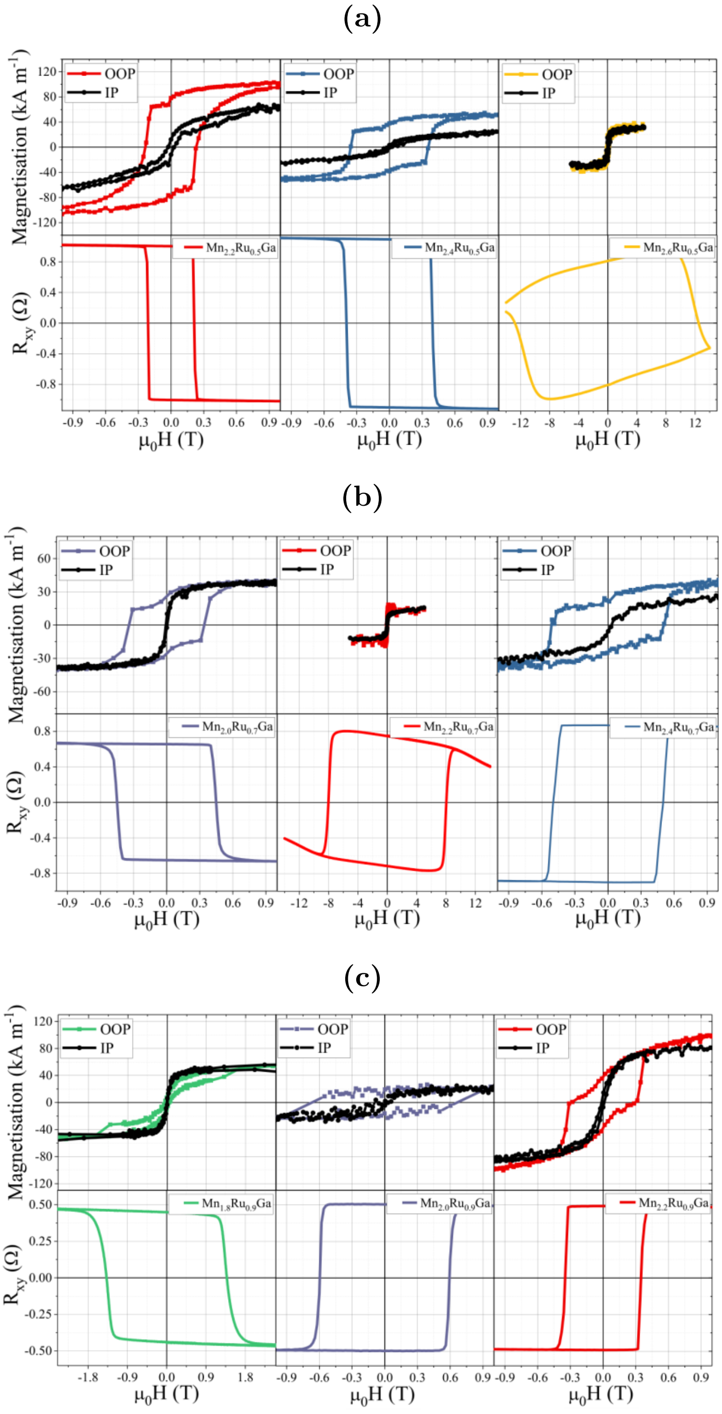

Figure 3.7: Magnetization and AHE measurements of Mn$_y$Ru$_x$Ga at 300 K(a) for x = 0.5, (b) x = 0.7 and (c) 0.9. OOP and IP magnetization curve has two states switching mechanism due to the presence of noncolinear magnetic states in Mn$_y$Ru$_x$Ga. M^{net} has a easy cone anisotropy state, were as M^{4c} has an approximately colinear easy-axis state. This work is also included in Siewierska's Ph.D. thesis [12].

Therefore, Δ_1, Z, P and T_e are the only fitting junction-specific parameters of the model. Additionally, the spectrum broadening, quadratic high-bias background correction have been taken into account in the fitting model.

The additional broadening in the measured data is due to the presence of the sample resistance, which is in the series with the contact resistance. Consequently, the actual bias voltage across the contact is less than the applied bias signal from the source. Therefore, it leads to an apparent broadening of the PCAR signal. The resistance of the sample may have bulk as well as surface contributions. For example, in the case of MRG, the presence of thin capping layer (AlO_x) can provide an additional resistance to the samples. Although, all efforts have been taken to punch through the thin AlO_x using sharp Nb tips, the complete elimination of the layer is a difficult choice to make, as desperate attempts may lead to destroying the tip[9].
The m-BTK model takes into account the superconducting proximity effect at the junction. The value of Δ_1 for all the measured sample lies between 1.3 meV to 1.5 meV , which is very close to the bulk superconducting gap of Nb, $\Delta_2 = 1.5$ meV. This suggest that order parameter of proximity effect decays very fast near the contact. A quick decay of order parameter near the junction is attributed to the large energy mismatch between two spin bands and/or the presence of significant spin-orbit coupling in MRG.
Another important parameter is the effective transport temperature of the electron, also known as electronic temperature T_e. In the case of all the measured PCAR spectra of MRG, this value lies between 4 K and 7 K, which is well above the measurement bath temperature ≈ 2 K. The possible reasons for such a high electronic temperature are several fold, such as transport in the tunneling regime (non-δ barrier) and joule heating at the junction. In the presence of any physical barrier (a thin capping layer in this case) or a Schottky barrier, transport is dictated by the higher energy electrons (also called hot electrons). Hence, its manifestation in the higher electronic temperature.
The δ-barrier strength parameter, Z, includes the effect of any non-conducting thin

---

[9] PCAR spectrum highly depends on the transport regime. For a large contact area, transport is in a completely diffusive limit where both energy and momentum information are lost, and hence the essence of PCAR measurement.

layer at the junction. Furthermore, the quadratic background of the spectra at high bias is attributed to the some existence of tunneling components and the presence of non-flat bands at the Fermi level. The corrections for these terms have been taken into account in the fitting model.

The resultant value of spin polarization (P) is shown in figure 3.10 along with the anomalous Hall angle (AHA). The value of the spin polarization decreases significantly as the Ru content in MRG increases, which is also in-line with the reduction of AHA by the same proportion. This is due to the fact that either s-like electrons from Ru reduce the band gap at the Fermi level, or the extra electrons originating from the Ru (2 electron per Ru atom) shift the Fermi level above the gap. A maximum value of $P \approx 63\%$ is obtained for $\mathrm{Mn_{2.4}Ru_{0.5}Ga}$, which is one of the highest experimentally reported values among Heusler alloys. The observed spin polarization of $\mathrm{Mn}_y\mathrm{Ru_{0.5}Ga}$ for Mn deficient alloys decreases from around 60 % to 51 % as the Mn concentration decreases from 2 to 1.6, which indicates the Fermi level shifts further away from the spin gap. The drop in the value of spin polarization is also correlated with AHA measurements. This is due to poor crystallinity and site-disorder mixing the spin states, which result in lower spin polarization. However, excess of Mn results ($2 \leq y \leq 2.4$) in slight increase on spin polarization due to the Fermi level shifting towards the spin gap. Furthermore, for very high Mn concentration ($y > 2.4$), the spin-polarization starts rolling down again. This may be due the spin band mixing for excess Mn concentration, which is caused by deviations from the single phase near cubic ($\mathrm{L_{21}}$) structure with higher Mn to Ga ratio. It is worth mentioning that the spin polarization measured using PCAR is difficult to match to the theoretical prediction ($P = 100\%$) due to finite experimental temperature, presence of spin-orbit coupling, spin scattering events and a difference between bulk and surface states. All of these are often ignored or over simplified while calculating/predicting the PCAR spectra.

Figure 3.10 also highlights a qualitative relation between spin polarization and anomalous Hall angle of MRG. AHE is attributed to spin-orbit coupling arising either due to intrinsic or extrinsic contributions. The extrinsic part is mainly due to local crystal field distortion produced by disorder present in the sample. The

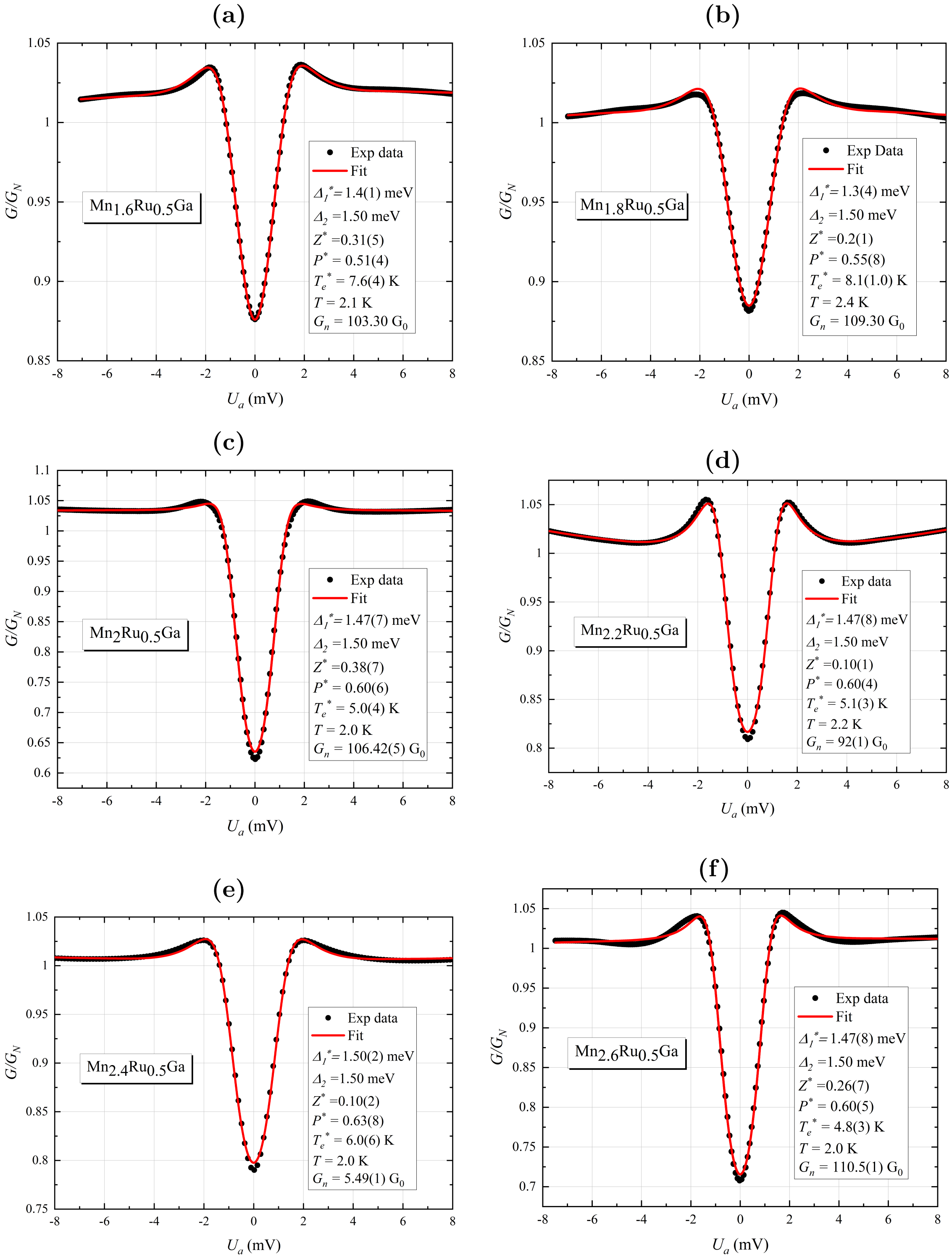

Figure 3.8: PCAR spectra of $Mn_yRu_{0.5}Ga$ along with the modified BTK fit. Parameters used in modified BTK model to fit the spectra are shown in the inset. The extracted parameters from the fit are labeled with asterisks. Each PCAR curve is normalized by the background data collected after quenching the the superconducting tip (Nb) above the critical temperature, $T > 10$ K.

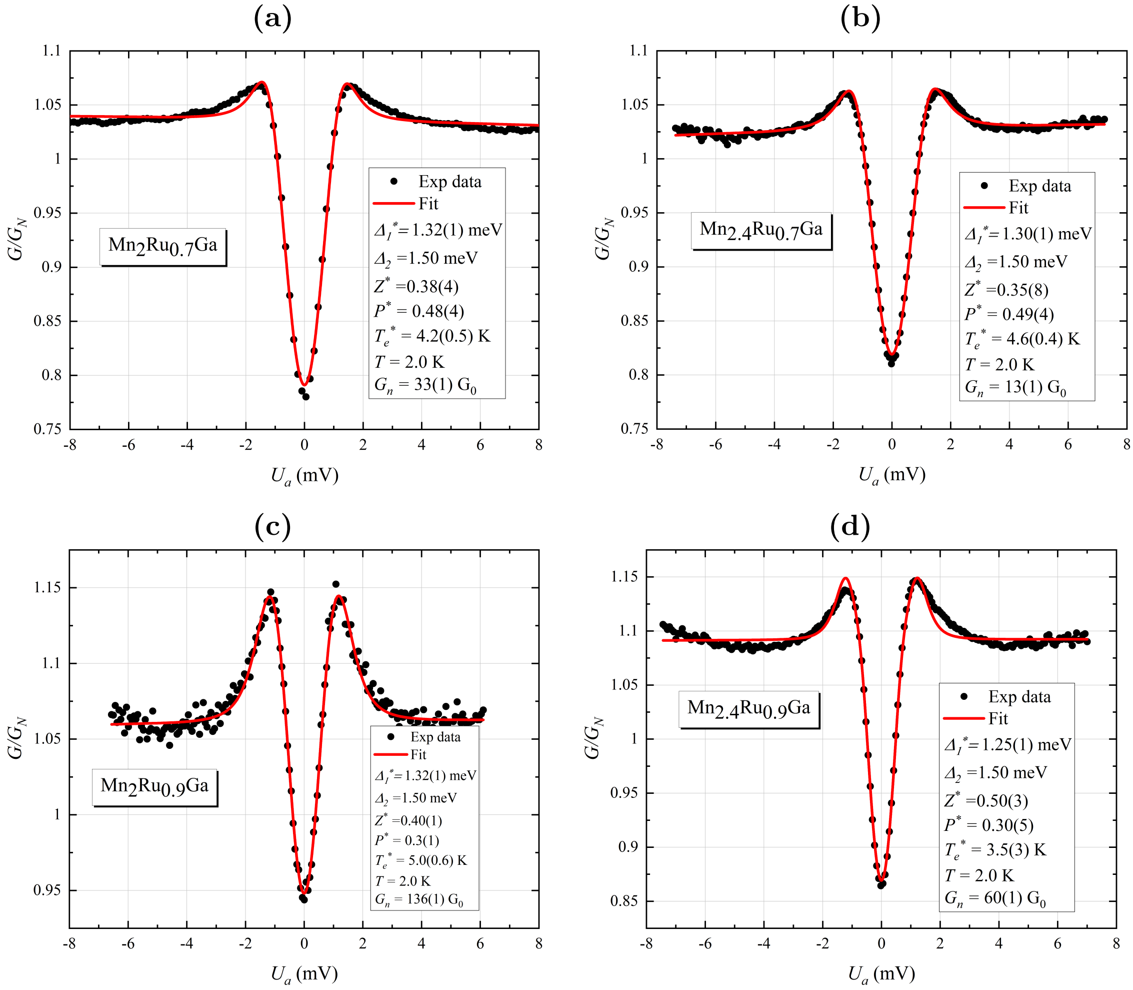

Figure 3.9: PCAR spectra of Mn_yRu_xGa along with the modified BTK fit. Top panel for $x = 0.7$ and bottom panel for $x = 0.9$. Parameters used in modified BTK model to fit the spectra are shown in the inset. The extracted parameters from the fit are labeled with asterisks. Each PCAR curve is normalized by the background data collected after quenching the the superconducting tip (Nb) above the critical temperature, $T > 10$ K.

locally distorted crystal field gives rise to two main scattering mechanism, namely side jump and skew scattering, in the transverse direction. On the other hand, the intrinsic contribution arises due to the Berry phase acquired by the Bloch function in the presence of non-trivial spin texture in the sample. Although, for the AHE requirement of spin-polarized carrier is not essential the effect gets amplified for the spin-polarized carrier. The high value of AHE ($\theta_H = 2\%$) is an order of magnitude higher than in conventional ferromagnetic samples. This may be due to a significant intrinsic scattering contribution in combination with the high-spin polarized carriers in MRG.

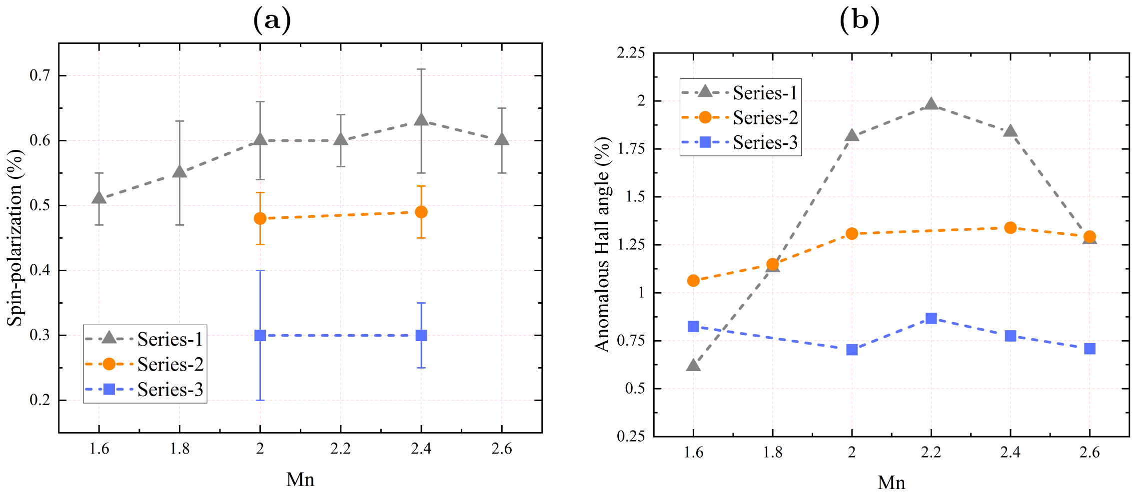

Figure 3.10: (a) Spin polarization as obtained from PCAR measurement vs Mn concentration for various Ru value, refer to table 3.1 for the sample details. (b) Anomalous Hall angle vs Mn concentration for various Ru values. A direct correlation can be seen between spin-polarization and anomalous Hall angle. A higher spin-polarization results to a higher Hall angle.

3.5 Conclusions

High quality $\mathrm{Mn_yRu}_x\mathrm{Ga}$ films have been deposited on MgO (001) substrate. The excess Mn mainly occupies the $4c$ and $4d$ and $4b$ sites, leading to a reduction in the density of vacancies. The full occupancy in $\mathrm{Mn_yRu}_x\mathrm{Ga}$ provides noncolinearity in the sublattices moment, due to a competing positive and negative exchange interaction between Mn^{4c}, Mn^{4d} and Mn^{4b}. The AHE and magnetization behavior of MRG can be fully understood under the established noncolinear magnetic state. It is also reported that compensation temperature (T_{comp}) of MRG can be obtained for a wide temperature range by selecting an appropriate stoichiometry. The presence of huge coercivity ($H_c > 14$ T) in the AHE at the compensation point highlights the existence of very high anisotropy field. Therefore, MTJ devices made with MRG will not require any antiferromagnetic layer to pin the magnetization direction. Spin polarization as high as 63% can be achieved by tuning the chemical composition of MRG. Finally, a qualitative relation between high spin polarization and very high anomalous Hall angle (θ_H) was also established. It is evident that MRG with high spin-polarization show high θ_H. Therefore, AHE measurement facilitates an alternative method to identify highly spin-polarized MRG samples.

4

Static magneto-transport study of $\mathrm{Mn_2Ru}_x\mathrm{Ga}$ thin film

4.1 Introduction

Utilizing $\mathrm{Mn_2Ru}_x\mathrm{Ga}$ (MRG) as an active layer in the spin-oscillator, sub-THz chip-to-chip communication can be achieved as its spin excitations lie in the required terahertz gap [80]. The sub-THz excitations of MRG are attributed to its low magnetic moment [22, 75], high uniaxial anisotropy field [76], and low Gilbert damping [80, 81]. Furthermore, the tunability of the anisotropy constant and the moment in MRG provides the freedom to alter the resonance frequencies of oscillator made with MRG [80]. Therefore, the determination of anisotropy constants of MRG thin-films is a prerequisite to studying their magnetization dynamics in the presence of external stimuli. Examining anisotropy and other magnetization dynamics, in a sample with vanishing magnetic moment, using magnetometry techniques (VSM, SQUID) is unobtainable due to lack of resolution and sensitivity. Moreover, for a sample with vanishingly small magnetic moment, (M), both the anisotropy field, ($H_a = 2K/M$), and coercive field, (H_c), normally diverge, hence measuring the magnetic anisotropy requires impractically large magnetic field ($H > 14$ T, in case of MRG). Usually, anisotropy is determined by applying external magnetic field at certain angle, (θ_H), to the magnetic easy axis and measuring corresponding change in physical properties, such as magnetization [82, 83, 84], anomalous Hall effect [85, 86], magneto-optical properties [87, 88, 89]. These recorded data are fitted conventionally by the torque balance method.

This chapter presents an analysis of magnetic anisotropy and quasi-static magnetization dynamics of MRG thin-film, a compensated ferrimagnetic half-metal with a tetragonal crystal structure [75], through electrical transport measurement techniques. MRG exhibits a strong uniaxial out-of-plane anisotropy and small but significant four-fold in-plane anisotropy arising from substrate-induced compressive strain. Moreover, MRG manifests a large anomalous Hall effect along with high magnetic anisotropy field and high Fermi-level spin polarization [22, 76], a combination which offers a direct probe to the anisotropy of MRG thin-film by electrical means. Manipulation of the magnetization vector, ($\mathbf{M}$), of MRG in a 3D space, in the presence of a magnetic field, facilitates the analysis of various anisotropy constants of the film. To describe the equilibrium or the dynamic response of the magnetisation vector in an applied or induced effective field, it is essential to consider the magnetic anisotropy of the sample. The equation of motion of magnetization, in general, is spatially non-uniform (described by a micromagnetic model) or, in the much simpler case, spatially uniform (described by a macrospin model). This work uses the anomalous Hall effect to investigate magnetic anisotropy in MRG within the macrospin model.

This chapter begins with the sample preparation and characterization techniques used for this study. After that, a theoretical understanding of the Preisach model is described (see section 4.3) in order to estimate the hysteresis of MRG. Section. 4.4, introduces the first order reversal curve (FORC) method, an experimental technique to verify the Preisach models. The validity of the macrospin model for MRG is established within FORC and Preisach models. In section 4.5, equivalence of FORCs and classical Preisach hysteresis (hysterons) model is identified. A detailed torque model to evaluate the anisotropy constants of MRG using AHE is discussed in section 4.6. Furthermore, complex static and quasi static magnetization dynamics of MRG is discussed in section 4.7, utilizing a combined hysterons and torque model. Finally conclusions are formulated in section 4.8.

4.2 Methodology

The epitaxial thin film of Mn_2Ru_xGa were grown using DC magnetron sputtering system, on 10×10 mm^2 MgO (001) substrates. The films were co-sputtered under an inert environment (Argon gas) from Mn_2Ga, and Ru targets onto the substrate maintained at 320 °C. Further details of film growth and characterization is described in chapter 3. Here we focus on the $x = 0.9$ stoichiometry and film thickness of approx 40 nm. The compensation temperature (T_{comp}) of the sample is $T_{\text{comp}}{\sim}375$ K, determined using SQUID magnetometer, which is well above the room temperature. The $x = 0.9$ is selected for the investigation as for this composition the compensation point is well above the room temperature. Due to high compensation point, room temperature coercivity field ($H_c \sim 0.40$ T) is small enough to study the detailed reliable quasi-static magnetization dynamics of Mn_2Ru_xGa at room temperature. Additionally, $Mn_2Ru_{0.9}Ga$ film has high crystalline quality and low roughness at the interfaces. The films were in-situ capped with ~ 3 nm of amorphous AlO_x, deposited at room temperature, in order to prevent the oxidation of film. The substrate induced compressive strain ($c/a \approx 1.02$), determined by standard X-ray crystallographic techniques, accommodates the out-of-plane microcrystalline anisotropy to the film. To study the transport properties, the films were patterned into a micron-sized (60×20 μm^2) Hall bars by means of UV photolithography and Ar-ion milling. A second stage of lithography and metal deposition were carried out to define the contacts pads, Ti (5 nm)/Au(50 nm), see Fig. 4.1. Electronic transport properties were measured in Quantum Design Physical Property Measurement System (PPMS) between $2\,\text{K} \leq T \leq 300\,\text{K}$ and $|\mu_0 H| \leq 14\,\text{T}$. The longitudinal and transverse voltages were measured using the lock-in demodulation technique at the first harmonic with low excitation frequency, typically $f_{AC} \sim$ 517 Hz, which is much smaller than the magnetic excitation frequencies of MRG. The angular dependence of the resistivity and Hall effect were measured on a rotating platform

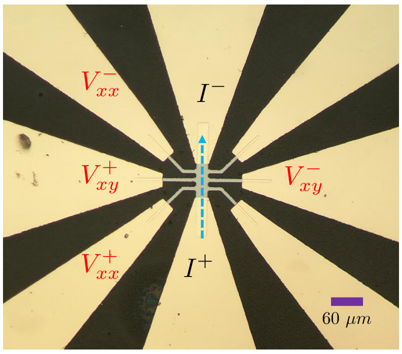

Figure 4.1: Photographically defined Hall bar used to measure magneto-transport study.

mounted on the PPMS probe, having an angular resolution of 0.01 deg. First order reversal curves (FORC) measurement were performed in a 1 T GMW electromagnet at room temperature with a field resolution of 5 mT.

4.3 Preisach (hysteron) model

This section discusses the approach used to model the switching of magnetization vector (magnetic hysteresis) using the classical Preisach (hysterons) model. Hysteresis modelling has been an active area of research for decades due to both physical and mathematical interest. The most famous example of hysteresis is the magnetic hysteresis of ferromagnetic materials. It is well known that the multiplicity of metastable states is the origin of hysteresis. Therefore, a micromagnetic model has to be considered for detailed hysteresis modeling. In 1935, Preisach [90] proposed a classical micromagnetic mathematical approach to describe the hysteretic effect. Preisach model uses a large number of interacting elementary magnetic entities (named hysterons) which have rectangular hysteresis loop, characterized by operator $R_{h,k}(x)$, where x is an arbitrary input variable such as an applied magnetic field , (figure 4.2a). The main idea is to replace a smooth hysteresis loop with a large numbers of elementary steps, where each step (hysteron) is parametrized by three values: 'on' condition, 'off' condition and the magnitude of the step. The hysteresis is the result of many such hysterons that switch fully at a discrete applied field.

The value of $R_{h,k}(x)$ depends on the applied field history. For example, if the applied field (x) begins from the positive saturation state ($x = \infty$), $R_{h,k}(x)$ starts at $R_{h,k}(\infty) = 1$. The value of $R_{h,k}(x)$ switches to -1 when the applied field crosses below the value h, a switch-off state, and $R_{h,k}(x)$ again reach the value $+1$ when the field value is above k, a switch-on state. In general, the switching fields h and k are not equal. The interaction field experienced by a hysteron is defined by $H_u = (h + k)/2$, which results in asymmetric hysteron (figure 4.2a). On the other hand, a hysteron with no interaction is symmetric in nature. Coercive field of hysteron is defined as $H_c = (h - k)/2$.

In a realistic sample, the hysteresis is a sum of a large number of hysterons and

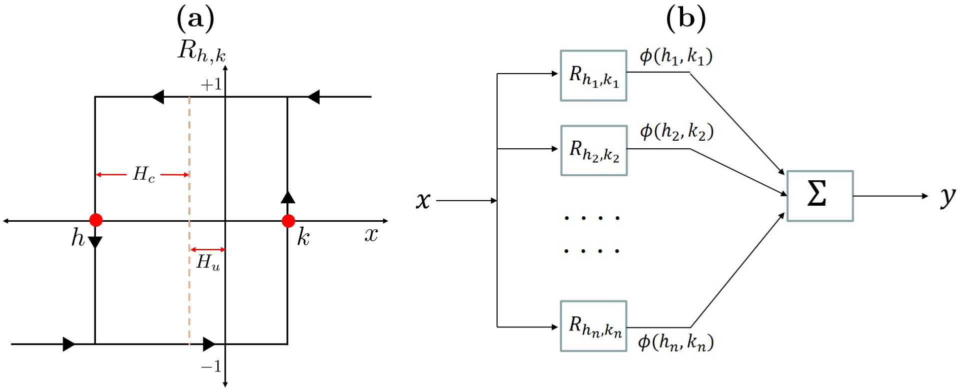

Figure 4.2: (a) An elementary hysteron with reversal fields of value h and k. (b) Preisach discrete model of hysteresis where a large number of hysterons are parallelly connected with corresponding weighing factor $\phi(h,k)$. Here, x is an arbitrary variable which in this case is an applied magnetic field and y is the resultant hysteresis output.

corresponding weighting factor $\phi(h,k)$, as depicted in figure 4.2b. Therefore, the resultant hysteresis curve can be expressed as:

$$y(x) = \sum_{i=1}^{N} \phi(h_i, k_i) R_{h_i,k_i}(x)\,, \tag{4.1}$$

where, $\phi(h,k)$ determines the weight of each hysteron. It is also known as hysteron weight or hysteron density function. In a continuum limit discrete model (equation 4.1) becomes:

$$y(x) = \iint_{k \geq h} \phi(h,k) R_{h,k}(x)\, \mathrm{d}h\, \mathrm{d}k\,, \tag{4.2}$$

where, x is an arbitrary variable which in this case is an applied magnetic field and y is the resultant hysteresis output. The most difficult part of the Preisach model is to uniquely defined the hysteron density function $\phi(h,k)$. However, for an ensemble of weakly interacting hysterons, the distribution function $\phi(h,k)$ is often described by a Gaussian or Voigt distribution [91, 92].

The geometrical interpretation of Preisach model can be understood with the help of the Preisach plane, given by:

$$P = \{(h, k | k \geqslant h)\}\,, \tag{4.3}$$

where (h, k) are the points in the Preisach plane, as shown in figure 4.3. Therefore, all hysterons can be represented in a lower half-square triangle, where each point on the plane describe the Preisach hysteron and their distribution [14]. On this plane symmetric hysterons lie along the diagonal $h = -k$, which describes the isolated single domain particles [93]. In case of $h \neq -k$ (asymmetric hysterons), hysterons are shifted by some finite values. The physical realization of such shift is referred to the interaction field H_u, which is attributed to the magnetostatic interactions and/or other long range interactions [94, 13].

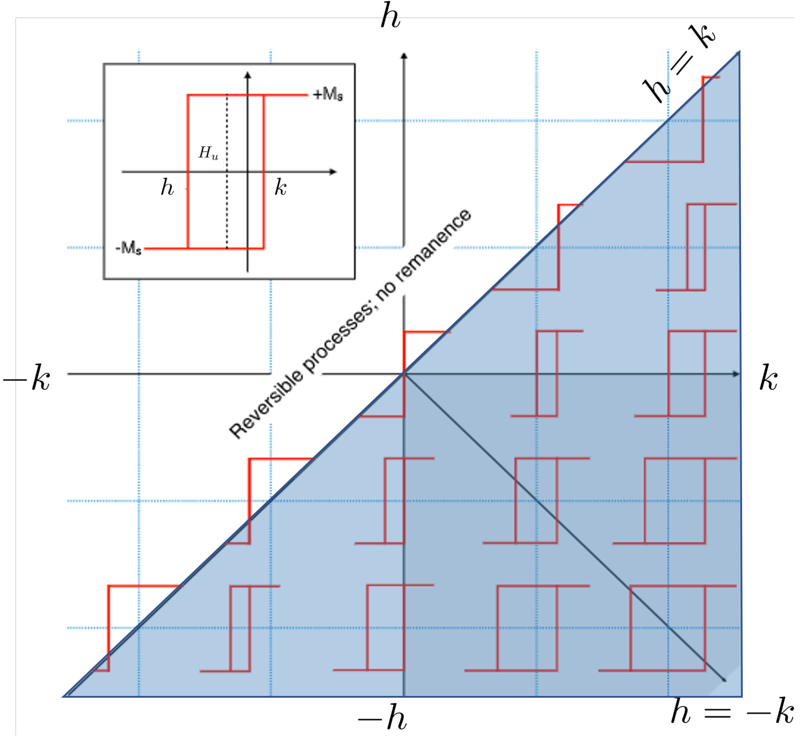

Figure 4.3: (Inset) A hysteron with switching fields h and k, interaction field H_u. (Main) A Preisach plane spanned lower half-square triangle. Each point on the plane corresponds to the Preisach hysteron and their distribution. Hysterons with no interaction (symmetric hysterons) lie along the diagonal $h = -k$, while hysterons with finite interaction (asymmetric hysterons) lie perpendicular to diagonal $h = -k$. The picture is after Church *et al.* and Fabian *et al.* [13, 14].

To determine the Preisach distribution function $\phi(h, k)$ of an arbitrary sample, consider that in the beginning, in a saturation field all hysterons are in the up position (+1) (figure 4.4a), and as the value of applied field is decreased to a reversal field (H_R) point at the major hysteresis loop, a fraction of hysterons begin to switch from up (+1) to down (-1), as shown in figure 4.4b. The resultant magnetization

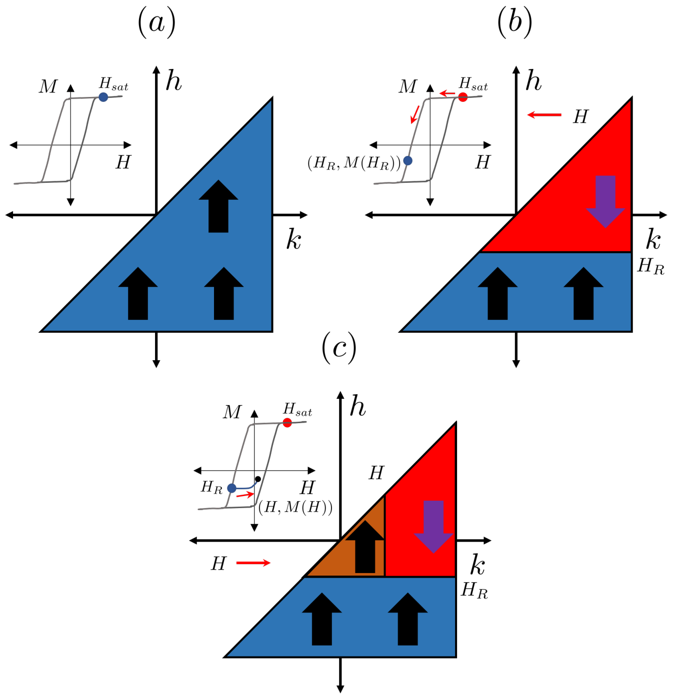

Figure 4.4: Geometrical representation of Preisach plane at various biasing stages. (a) When applied field $H \geq H_{sat}$, all the hysterons are in the up (+1) states, (b) at a reversal field H_R, a fraction of hysterons are in down (-1) states, (c) for the hysteresis curve at the minor curve, a fraction of down (-1) states again switched back to up state (+1).

(figure 4.4b) as a function of reversal field can be written as:

$$M(H_R) = \iint\limits_{S^+} \phi(h,k) R_{h,k}(H_R)\, \mathrm{d}h\, \mathrm{d}k + \iint\limits_{S^-} \phi(h,k) R_{h,k}(H_R)\, \mathrm{d}h\, \mathrm{d}k\,, \tag{4.4}$$

where, S^+ and S^- are up and down hysterons. Since, hysteron operator $R_{h,k}$ are aligned with either +1 or -1 values, magnetization equation can be simplified to:

$$M(H_R) = \iint\limits_{S^+} \phi(h,k)\, \mathrm{d}h\, \mathrm{d}k - \iint\limits_{S^-} \phi(h,k)\, \mathrm{d}h\, \mathrm{d}k\,. \tag{4.5}$$

Furthermore, magnetization in the minor loop (figure 4.4c) can be described as the function of applied field (H) and reversal field (H_R) as:

$$M(H,H_R) = \iint\limits_{S^+} \phi(h,k)\, \mathrm{d}h\, \mathrm{d}k - \iint\limits_{S^-} \phi(h,k)\, \mathrm{d}h\, \mathrm{d}k + \iint\limits_{S(H,H_R)} \phi(h,k)\, \mathrm{d}h\, \mathrm{d}k\,, \tag{4.6}$$

where the third integral is the area of additional small triangle as depicted in figure 4.4c. From equation 4.5 and equation 4.5:

$$M(H_R) - M(H, H_R) = -2 \iint\limits_{S(H,H_R)} \phi(h,k)\,\mathrm{d}h\,\mathrm{d}k\,. \tag{4.7}$$

Therefore, the distribution function can be given by:

$$\phi(H, H_R) = \frac{1}{2}\frac{\partial^2}{\partial H \partial H_R}[M(H_R) - M(H, H_R)]\,. \tag{4.8}$$

Since, $M(H_R)$ is only a function of H_R, hence:

$$\phi(H, H_R) = -\frac{1}{2}\frac{\partial^2}{\partial H \partial H_R}[M(H, H_R)]\,. \tag{4.9}$$

Equation 4.9 is first proposed by Mayergoys [95] to successfully obtain the Preisach distribution. Hence, knowing the the Preisach distribution from equation 4.9 and Preisach operator (hysteron), a physical analysis hysteresis phenomena can be realized, as per the equation 4.2. However, to use equation 4.9, the input signal (M) must be continuous and differentiable, which makes it difficult to implement in experimental data due to presence of noise in the sensors. Therefore, an alternative and efficient method is required under such circumstances. One possibilities is to assume that $\phi(H, H_R)$ follows a certain statistical distribution. The most popular choices are Gaussian function [96, 97, 98], Gauss-Lorentzian function [99], or log-normal distribution function [100], etc. The problem with this approach is the lack of justification about considering one particular distribution over other distribution functions [100]. Another method involves utilizing linear combination of a family of functions as a basis. The problem with this approach is that to obtain a Preisach distribution of a rather continuous output (M) requires a very large set of basis function and their coefficients [101], which quickly exhaust the computational abilities, even of modern computers.

Therefore, in order to successfully obtain the Preisach distribution, Mayergoyz proposed the first-order reversal curve (FORCs) method, a promising experiment technique, provided that the sample of interest satisfies the necessary and sufficient Mayergoyz conditions [102].

4.4 First order reversal curve (FORC) method

The most popular method to characterize a magnetic material is a measurement of its hysteresis (M-H) loop, called the main hysteresis loop (MHL). The MHL provides only the average properties such as saturation magnetization (M_s), remanence (M_r) and coercivity (H_c) of the sample. It fails to explain other characteristic properties such as interactions present on the microscopic level. More complex magnetization curves, such as higher order magnetization curves, which probe the interior of the MHL, are needed to provide further insight of magnetic interactions and other microscopic properties [103, 104]. Higher order reversal curves are obtained when applied field is swept from an initial point on the MHL, called the reversal point $M(H_R)$. One such higher order magnetization curve is obtained by first saturating the sample at high magnetic field and then allowing the field to decrease to a point on the descending branch (reversal point) of MHL before swiping the field in the negative direction. The resultant curves are called the first order reversal curves. This method can be extended to even higher order (second and third order) by considering higher number of reversal points. The analysis on this thesis is limited to the first order approximation.

In order to probe the interaction of hysterons, Mayergoyz [102] proposed a FORCs (first-order reversal curve) method, which is a promising experimental technique to evaluate the Preisach distribution. The FORC method is easy to achieve experimentally and highly reproducible as it begins by saturating the sample each time. The FORC method has been utilized to study various magnetic systems, such as permanent magnets [105, 106], geological samples [107, 108], nanowires [109, 110], etc. FORCs can distinguish between interacting and noninteracting single-domain (SD), pseudo single-domain (PSD) and multi-domain (MD) system [111, 107]. In fact, FORC method can be extended to any system which show hysteresis behaviour, for example in ferroelectric samples [112, 113].

The process of FORC measurement is shown in figure 4.5. Each FORC measurement begin by saturating the sample in a large enough positive field. Following saturation, the field value is changed to a reversal value (H_R) on the MHL (figure 4.5a). The applied field (H_A) is then swiped towards the positive value and magnetization

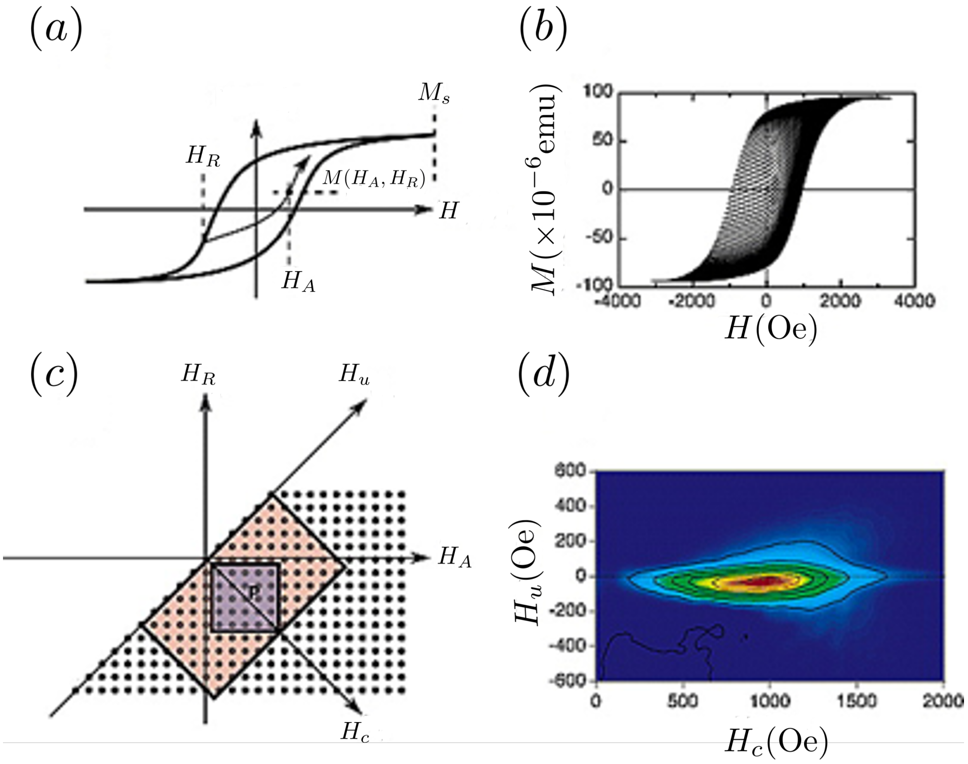

Figure 4.5: FORC method. (a) definition of FORCs, (b) A set of FORCs for a single crystal of clinopyroxene (after [15]), (c) grid of H_A and H_R used to measure magnetization $M(H_A, H_R)$, (similar to Preisach plane shown in figure 4.3), (d) contour plot derived for the figure 4.5b in the rotating co-ordinate system, H_c and H_u. The pictures are after Harrison *et al.* [16].

$M(H_A, H_R)$ as a function of increasing field is measured, until positive saturation is reached. In order to cover the entire area of MHL, a large number of FORCs are measured at various reversal field (H_R) (figure 4.5b). The values of H_A and H_R are chosen in such a way that it spanned in a regular grid. The FORC distribution is defined by taking the mixed second derivative of $M(H_A, H_R)$, as shown below:

$$\phi(H_A, H_R) = -\frac{1}{2}\frac{\partial^2}{\partial H_A \partial H_R}[M(H_A, H_R)]\,. \tag{4.10}$$

The equation 4.10 takes a form similar to the Preisach distribution function (equation 4.9). The contour plot of FORC distribution conveniently represented in a rotated co-ordinate system, (counterclock wise by 45°), where x-axis is expressed in switching field given by $H_c = (H_A - H_R)/2$ and y-axis is expressed in terms of interaction field $H_u = (H_A + H_R)/2$ (figure 4.5d).

Prior to evaluating second derivative (equation 4.10), smoothing of FORC curves is performed in order to remove the experimental noise. While, smoothing is vital to reduce the experimental noise, excess smoothing may leads to distortion of FORC distribution. Therefoe, to evaluate the FORC distribution, a weighted least square fit is performed on each grid point (say P) of $M(H_A, H_R)$ over the neighboring points around P. The number of local surrounding points are carefully decided upon, as per the data matrix density in order to evaluate the mix second derivative and at the same time avoid excess smoothing. In the most popular method, magnetization is fitted using second order polynomial equation:

$$M(H_A, H_R) = a_1 + a_2 H_A + a_3 H_A^2 + a_4 H_R + a_5 H_R^2 + a_6 H_A H_R \tag{4.11}$$

Therefore, the FORC distribution at the point P is equal to $-a_6/2$. The FORC diagram provides the insight of magnetic interaction within the SD, PSD and MD system (figure 4.6), which mimic like a finger print of magnetic system.

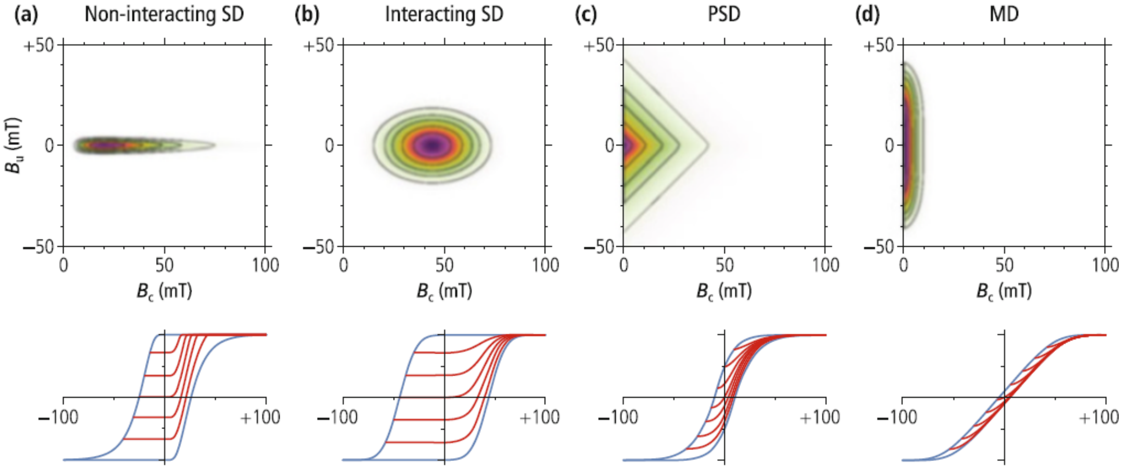

Figure 4.6: Simulated FORC distribution of magnetic sample. First row indicates FORC distribution. Second row indicate corresponding MHL and FORCs. (a) Non-interacting SD, central ridge along $B_u = 0$, (b) Interacting SD, distribution of interaction field is present, (c) PSD, triangular contours, (d) MD system with broad distribution of interaction field. The picture is after Franco and Dodrill [17].

The switching field distribution (SFD) of hysterons can be easily obtained by integrating FORC distribution function $\phi(H_c, H_u)$ over H_u:

$$\phi_{SFD}(H_c) = \int_{-\infty}^{\infty} \phi(H_c, H_u) \mathrm{d}H_u \,. \tag{4.12}$$

SFD defined by equation 4.12 indicates the intrinsic switching field distribution of particles, which is a valid and unique Preisach distribution (equation 4.2) if wiping-out and congruency properties are satisfied [102].

4.5 Hysteresis of $\mathbf{Mn_2Ru_xGa}$

Magnetization dynamics of MRG is elusive to probe using conventional magnetometer, VSM, SQUID, etc, techniques as it exhibit low magnetic moment. However, MRG display large anomalous Hall effect (AHE) and the transport properties are dictated by electrons from a band primarily contributed by Mn^{4c} sites. Consequently electrons are highly spin-polarized at the Fermi level. Therefore, AHE is predominantly proportional to the moment of Mn^{4c} sites. Since, moment of Mn^{4c} and Mn^{4a} are strongly coupled with antiferromagnetic interaction, AHE provides a tool to probe the magnetization dynamics.

A micromagnetic understanding is required to study the magnetization dynamics of a magnetic sample. However, a macrospin model can also be utilized in samples where the domains of highly textured films do not interact strongly. MRG grown on MgO substrate posses highly textured film quality, where the domain size is mainly determined by the structural defects. A typical domain size in MRG is of the order of 10s of micron [114] and the size of domains highly depends on the thin-film quality. In this section, an experimental evidence of non-interacting domain in MRG, in order to validate the macrospin approximation, is discussed using the FORC method. Furthermore, the static magnetic reversal mechanism of MRG is established under the Preisach model. Hysteresis curve of MRG measured at various temperatures are also analyzed under the Preisach model.

FORCs on MRG is measured on a patterned Hall bar using 1 T GMW electromagnet at room temperature with a field resolution of 5 mT. FORCs measurements begun with saturating the sample in a positive 'high enough' magnetic field. Then the field was decreased to a lower field value on MHL, called reversal field (H_R), and a $R_{xy}(H_A, H_R)$ was measured by sweeping the applied field H_A back to the saturation field. The resultant AHE resistance, $R_{xy}(H_A, H_R)$, is a minor curves inside the MHL (see figure 4.7a). This process is repeated for many evenly spaced values

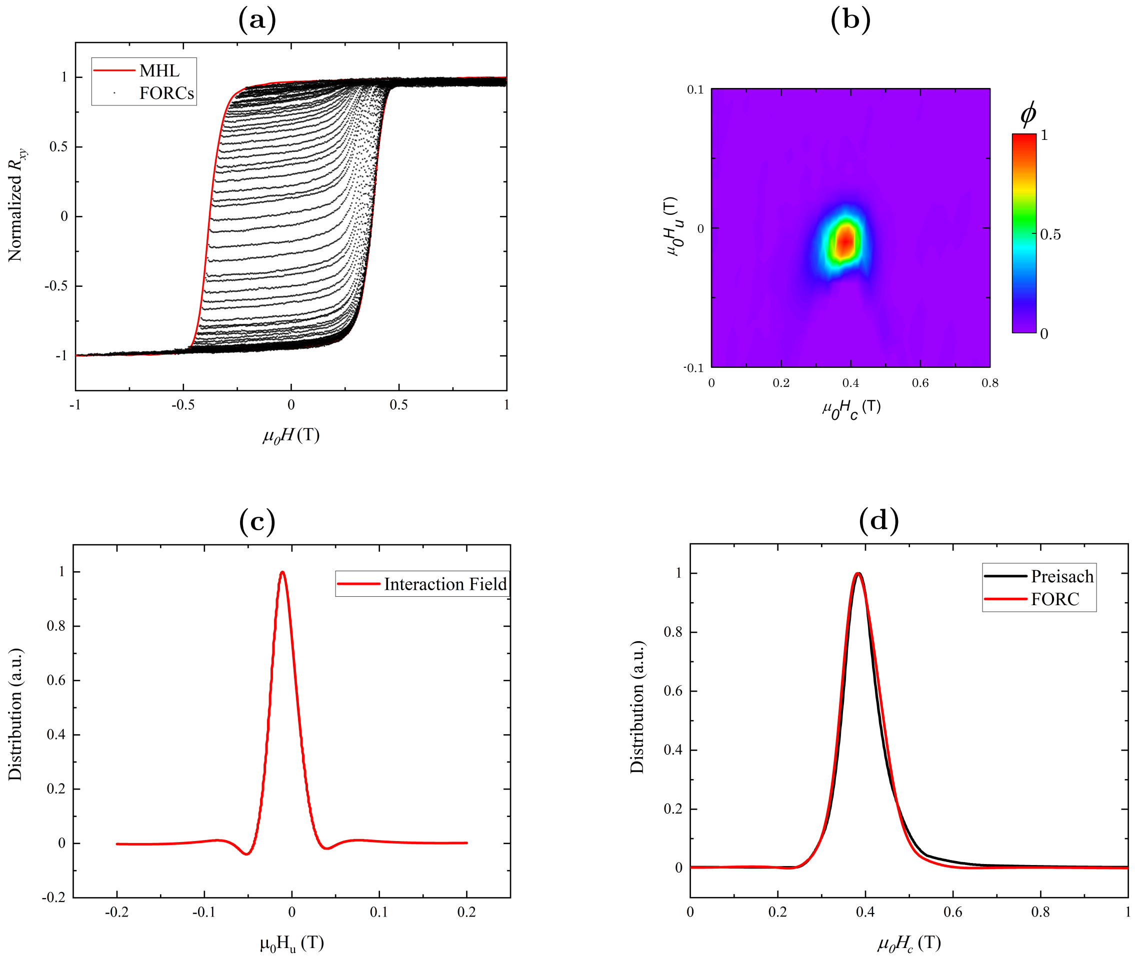

Figure 4.7: (a) FORCs measurement of MRG using AHE. The main hysteresis loop (MHL) is in red line whereas each minor magnetization curve (FORC) is shown in black dotted lines. Each FORC curve is obtained by sweeping the magnetic field from reversal point (H_R) to the saturation point. (b) FORC distribution of MRG is obtained by calculating the mixed second order derivative of curve (a). (c) distribution of interaction field H_u obtained from FORC distribution. It highlights the absence interacting hysterons in the MRG. (c) SFD obtained from FORC diagram (red line) and estimated PSD obtained under Preisach model (black line).

of H_A and H_R. The FORC distribution was obtained by the second order derivative (equation 4.10), defined by:

$$\phi(H_A, H_R) = -\frac{1}{2}\frac{\partial^2}{\partial H_A \partial H_R}[R_{xy}(H_A, H_R)]\,. \tag{4.13}$$

A Mathcad® program has been utilized to locally evaluate the partial derivative of $R_{xy}(H_A, H_R)$, as described in section 4.4. The resultant FORC diagram is shown in figure 4.7b. The central ridge is observed around $H_u = 0$ and $H_c = 0.387$ T. Figure 4.7c represents the local interaction field of MRG. A narrow distribution of

H_u with central point at $\mu_0 H_u = 0$ T highlights the absence of any interaction (dipolar, exchange, etc.) between the elementary units (hysterons). Therefore, in the absence of inter-particle interaction the over all system can be safely approximated under the Stoner–Wohlfarth (SW) model [115].

The local coercive field distribution of FORC diagram is shown in figure 4.7d with most probable coercive field (center point) at $H_c = 0.387$ T. A statistical analysis of coercive field distribution is carried out under the Preisach model. In this case, a pseudo-Voigt distribution is considered, defined as:

$$V(H_c, H_{c_0}, \Gamma) = \eta G(H_c, H_{c_0}, \Gamma) + (1-\eta) L(H_c, H_{c_0}, \Gamma)\,, \tag{4.14}$$

where, $G(H_c, H_{c_0}, \Gamma)$ and $L(H_c, H_{c_0}, \Gamma)$ are normalized Gaussian and Lorentzian function. Γ is the common FWHM and H_{c_0} is peak center. η $(0 \leq \eta \leq 1)$ is a weighing factor which shift the overall profile towards pure Gaussian or pure Lorentzian by shifting the factor from 1 to 0 respectively.

Here, the Gaussian part is defined as:

$$\begin{aligned} G(H_c, H_{c_0}, \sigma) &= \frac{1}{\sigma\sqrt{2\pi}} e^{-\frac{(H_c - H_{c_0})^2}{2\sigma^2}} \\ \sigma &= \frac{\Gamma}{2\sqrt{2\ln(2)}}\,, \end{aligned} \tag{4.15}$$

and Lorentzian part is given as:

$$L(H_c, H_{c_0}, \Gamma) = \frac{1}{\pi} \cdot \frac{\Gamma/2}{(H_c - H_{c_0})^2 + (\Gamma/2)^2}\,. \tag{4.16}$$

The coercive field distribution of FORC diagram can be fitted with equation 4.14. The long tail of coercivity distribution is attributed to the magnetic viscosity arising from the thermal fluctuations of metastable states. The magnetic viscosity in MRG is primarily due to rotation of magnetization vector as contribution from domain wall motion is highly restricted by the defects and disorder present within the film [114]. Thus, viscosity can be incorporated as a sum of exponentially decaying metastable states. Therefore, the Preisach distribution of coercive field (SFD) can be written as the convolution of viscosity term with the pseudo-Voigt function, i.e.:

$$D(H_c, H_{c_0}, \Gamma, \tau) = \int_{-\infty}^{\infty} V\left[(H_c - \xi), H_{c_0}, \Gamma\right] \frac{1}{\tau} \left[\exp\left(\frac{-\xi}{\tau}\right)\right] \mathrm{d}\xi \,, \tag{4.17}$$

where, τ is the magnetic viscosity parameter with the unit of magnetic field. A good agreement between experimentally obtained coercive field distribution and Preisach distribution is shown in figure 4.7d. Therefore, distribution described by equation 4.17 is a unique solution of Preisach model defined by equation 4.2. It should be noted that here Preisach distribution is normalized by amplitude in order to achieve a faster numerical convergence. Additionally, normalization performed using area under curve can also be realized. The physical significance of such normalization is that it directly signify the determinist switching of hysteron when integrated over all the input space. Therefore, aerial normalization is also performed later in this section.

After obtaining the required hysteron distribution a hysteresis curve of MRG can be easily obtained by integrating over the SFD (equation 4.2). Figure 4.8a highlights the agreement between the experimental AHE data and fit obtained under Preisach model. The model has been also extended to out of plane hysteresis measurement of MRG at various measurement temperatures. Figure 4.9 shows the matching hys-

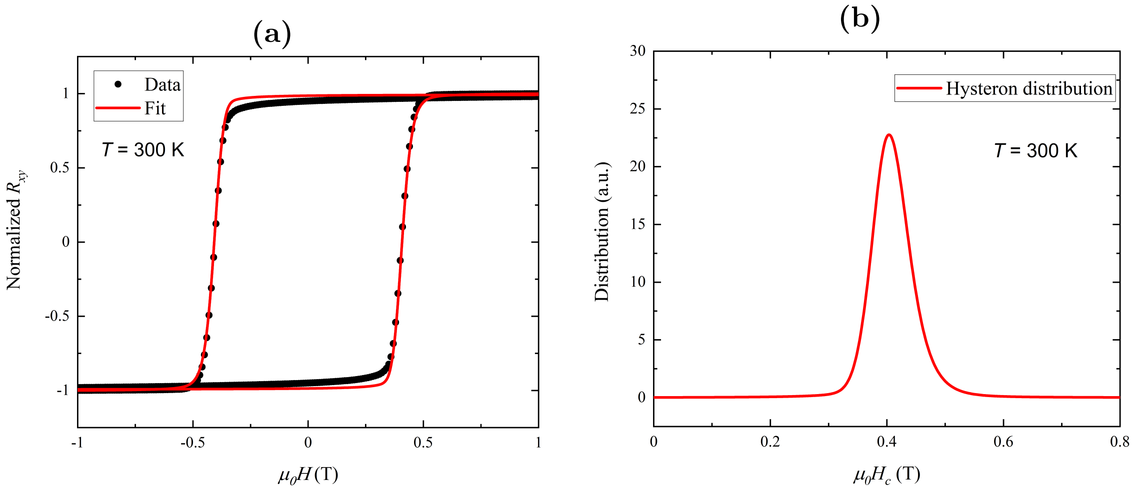

Figure 4.8: (a) AHE hysteresis data (black dot) and corresponding estimated Preisach hysteresis curve (red line) at 300 K. The Preisach hysteresis curve is obtained using equation 4.2 after experimentally obtaining the unique hysteron distribution using FORCs method, as shown in figure 4.7d. (b) Resultant hysteron distribution of the Preisach hysteresis model. It is equivalent to the distribution obtained under FORCs method (figure 4.7d).

teresis loops and corresponding Preisach distribution at 200 K, 100 K and 5 K. Thus

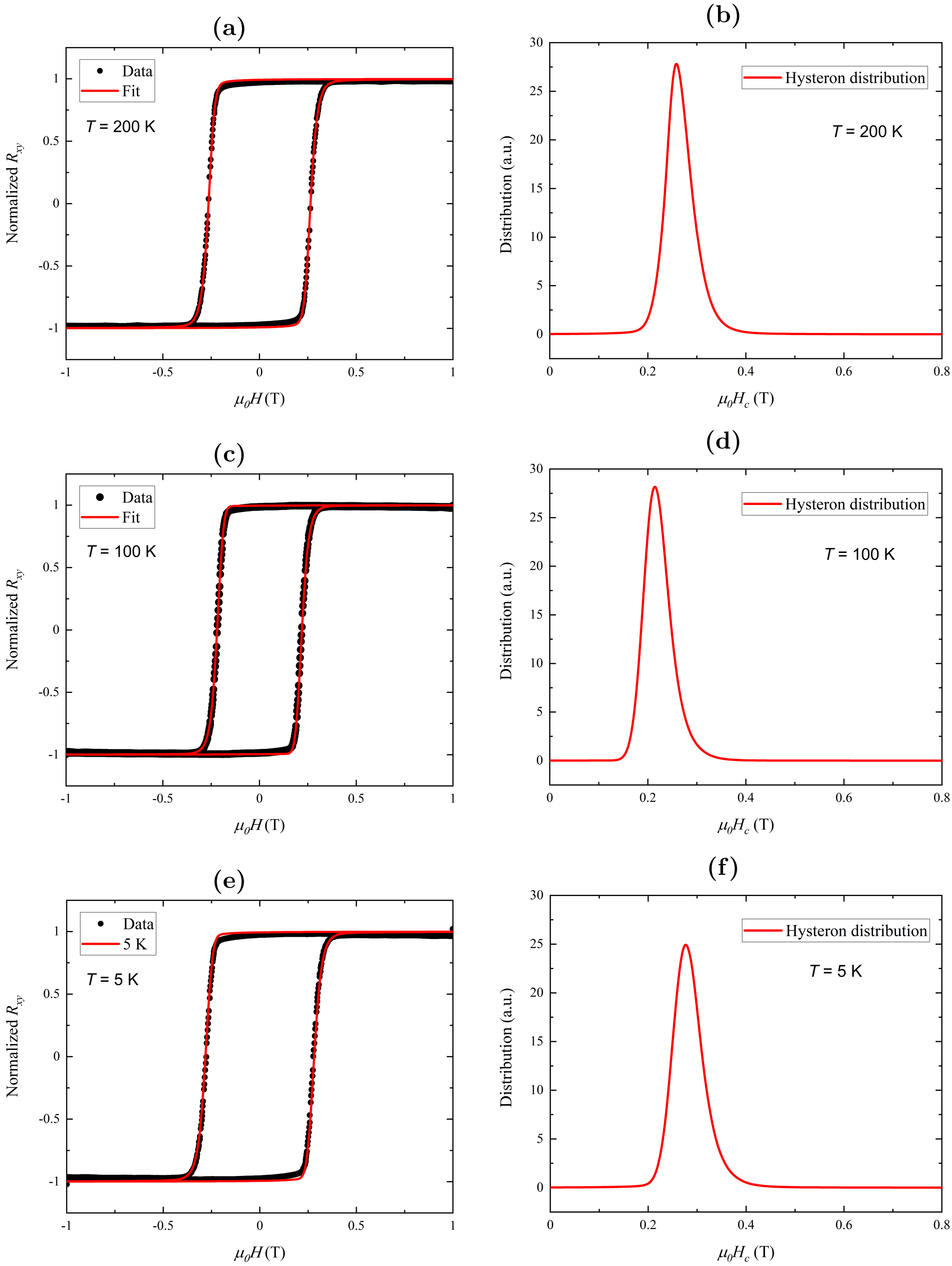

Figure 4.9: AHE hysteresis data and corresponding estimated Preisach curve in figure (a) at 200 K, (c) at 100 K and (e) 5 K. Estimated hysteron distribution in figure (b), (d) and (f).

modeling the hysteresis of MRG with only a few parameters (H_c, H_{c_0}, Γ and τ) has been achieved. A detailed summary of fitting parameters for various measurement temperatures are listed in table 4.1.

Table 4.1: Presiach fitting parameters as obtained by fitting the AHE data measured at various temperatures.

$\boldsymbol{T}$ (K)	$\boldsymbol{H_{c_0}}$ (T)	$\boldsymbol{\Gamma}$ (T)	$\boldsymbol{\eta}$ (T)	$\boldsymbol{\tau}$ (T)
300	0.387	0.059	0.783	0.023
275	0.33	0.047	0.807	0.023
250	0.297	0.056	0.788	0.02
200	0.246	0.036	0.656	0.021
175	0.228	0.037	0.865	0.023
150	0.212	0.027	0.969	0.026
100	0.199	0.032	0.915	0.024
70	0.197	0.095	0.905	0.022
60	0.198	0.027	0.948	0.023
40	0.206	0.034	0.776	0.024
20	0.226	0.038	0.798	0.022
5	0.26	0.094	0.933	0.025

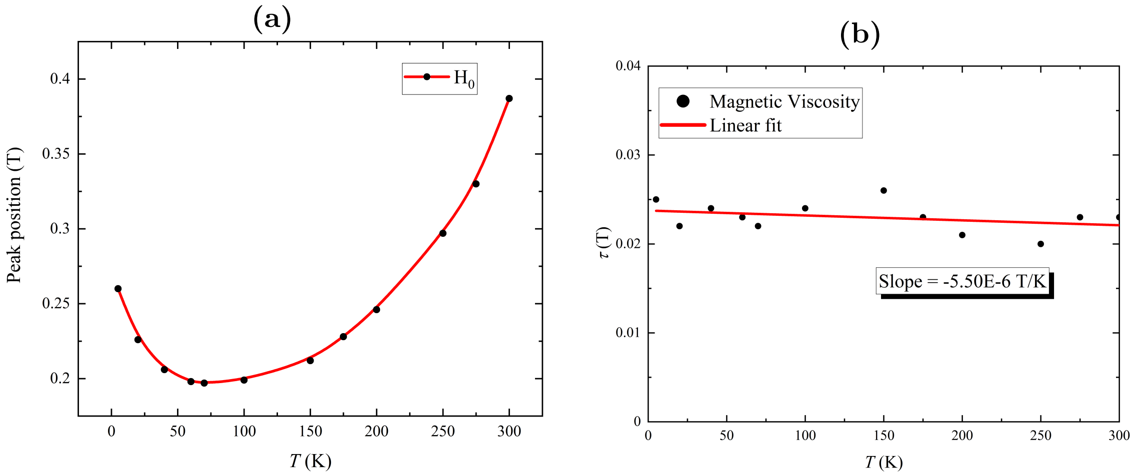

Figure 4.10: (a) Center-point (H_{c_0}) of Preisach distribution vs temperature. The value of H_{c_0} increases for both high and low temperatures. An increase in the former case is due to the temperature approaching the compensation temperature (T_{comp} = 375 K) whereas in the later case increase in the anisotropy constant at low temperature leads to increase in the value of central-point. (b) Viscosity parameter (τ) vs temperature. It suggests that viscosity is approximately independent in the measured temperature range. Therefore, domains for MRG are approximately frozen for wide temperature range.

Figure 4.10 shows the variation of center point (H_{c_0}) and magnetic viscosity (τ) as a function of temperature for hysteresis curves measured at different temperatures. Here, a very week dependency of magnetic viscosity parameter on temperature was observed. This is due to the fact that over all energy landscape of MRG is dominated by the anisotropy. Hence, any other weak thermodynamic fluctuations do not affect the static dynamics of magnetization vector. The variation of center point (H_{c_0}), which is most probable SFD of hysterons, hence the coercivity of sample, versus temperature has two separate regimes. At high temperature, coercive field increases due to diminishing net moment (approaching the compensation point, $T_{comp} = 375$ K) whereas at low temperature, the increase in the effective anisotropy dominates. Moreover, the first order viscosity parameter (τ) is approximately temperature independent, which suggest that domains for MRG are approximately frozen for wide temperature range. In fact, it is the frozen domains of MRG which greatly simplified the study of quasi-static dynamics of MRG under simplified Preisach model. In case of non-frozen domains, the overall magnetization dynamics becomes very computationally expensive method under Preisach model.

4.6 Torque model

Magnetization dynamics can be most easily examined within the macrospin approximation. In this approximation, spatial variation of magnetisation vector is frozen through out the equation of motion. The static and quasi-static magnetization dynamics of MRG can be approximated under the macrospin approximation due to lack of hysteron interaction, as shown in section 4.5. The torque model is based on the macrospin approximation where the equilibrium direction of the magnetization is evaluated by balancing the torque arising from effective anisotropy field, with the Zeeman torque. In the case of MRG, due to slightly distorted cubic crystal structure (tetragonal structure with $c/a < 0.02$), the balanced equation of torque can be easily obtained from the magnetic anisotropy free energy expression:

$$E = K_1 \sin^2(\theta_M) + K_2 \sin^4(\theta_M) + K_3 \sin^4(\theta_M) \cos(4\varphi_M) - \mu_0 \mathbf{H} \cdot \mathbf{M}\,, \tag{4.18}$$

where θ_M and φ_M are the polar and azimuthal angle of magnetization vector $\mathbf{M}$. K_1 and K_2 are the first and second order uniaxial out-of-plane anisotropy constants respectively. K_3 is the four fold in-plane anisotropy constant. The Zeeman term can be written as:

$$\mathbf{H} \cdot \mathbf{M} = HM \cos(\theta_M) \cos(\theta_H) + \sin(\theta_M) \sin(\theta_H) \cos(\varphi_M - \varphi_H)\,. \tag{4.19}$$

In case of MRG, in-plane anisotropy K_3 is at least an order of magnitude smaller than the out of plane anisotropy (K_1 and K_2). Hence, the azimuthal angle of magnetization vector always follows the azimuthal angle of applied magnetic field, i.e. $\varphi_M = \varphi_H$. Hence the effective energy surface for MRG can be written as:

$$E = K_1 \sin^2(\theta_M) + K_2 \sin^4(\theta_M) + K_3 \sin^4(\theta_M) \cos(4\varphi_M) - \mu_0 H M \cos(\theta_M - \theta_H)\,. \tag{4.20}$$

The equilibrium magnetization direction can be calculated by evaluating the extrema of equation 4.20 with respect of θ_M and φ_M. For example, the polar equilibrium position can be obtained by solving the following transcendental equation:

$$\frac{\partial E}{\partial \theta_M} = 2K_1 + (4K_2 + 4K_3 \cos(4\varphi_M)) \sin^2(\theta_M) - \frac{\mu_0 H M \sin(\theta_H - \theta_M)}{\sin(\theta_M) \cos(\theta_H)} = 0\,. \tag{4.21}$$

and,

$$\frac{\partial^2 E}{\partial \theta_M^2} > 0\,. \tag{4.22}$$

Here, we are using the anomalous Hall effect (AHE) to investigate the anisotropy constants which is only sensitive to the out of plane component of Mn^{4c} moment, i.e.:

$$\begin{aligned} V_{xy} &\propto |\mathbf{M}| \cos(\theta_M)\,, \\ \Longrightarrow \cos(\theta_M) &= \frac{V_{xy}}{V_{xy}^N} = v_z\,, \end{aligned} \tag{4.23}$$

where, V_{xy}^N is AHE voltage when magnetization ($\mathbf{M}$) lies along the easy axis (normal to the sample, $\theta_M = 0$) and v_z is the normalized AHE voltage. Therefore, the equilibrium condition of equation 4.21 reduced to:

$$\begin{aligned} \frac{2K_1}{M} + \left(\frac{4K_2}{M} + \frac{4K_3}{M} \cos(4\varphi_M)\right) (1 - v_z^2) \\ = \left(\frac{\mu_0 H \sin(\theta_H - \theta_M)}{v_z \sqrt{1 - v_z^2}}\right)\,. \end{aligned} \tag{4.24}$$

The energy landscape of MRG sample and trajectory of magnetization vector (as per equation 4.21 and 4.21) is shown in figure 4.11. To find out the values of K_1, K_2 and K_3, rotational scans in different geometrical configuration were performed in

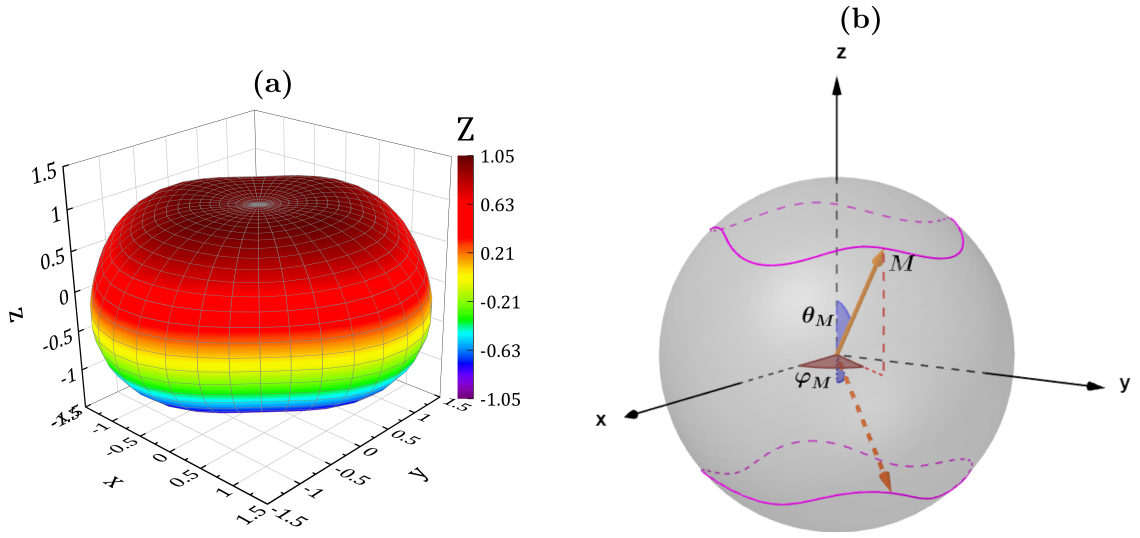

Figure 4.11: (a) Anisotropic energy landscape for tetragonal crystal system defined by equation 4.19. Here $K_1/M = 0.7$ T, $K_2/M = 0.3$ T and $K_3/M = 0.1$ T. (b) Trajectory of magnetic moment under such anisotropic energy landscape.

PPMS system (see section 4.2). Note that the recorded transverse resistance has five different contributions, namely: ordinary Hall effect (OHE), anomalous Hall effect (AHE), planner Hall effect (PHE), ordinary Nernst effect (ONE) and anomalous Nernst effect (ANE) as given by equation 4.25:

$$R_{xy} = R_{xy}^{OHE} + R_{xy}^{AHE} + R_{xy}^{PHE} + R_{xy}^{ONE} + R_{xy}^{ANE}\,. \tag{4.25}$$

In case of MRG, R_{xy}^{ONE} and R_{xy}^{ANE} were minimized by using a very small input bias current signal ($I_{RMS} = 50\,\mu\text{A}$) which ensures the absence of any significant thermal gradient within the sample under observation. Furthermore, to minimize the temperature gradient across the Hall bar, temperatures are stabilized in a Helium partial pressure ($P \sim 100$Torr) and sample was rotated very slowly, if needed. R_{xy}^{OHE} was extracted by measuring the slope of AHE at high magnetic fields ($\mu_0 H > 8$ T), as shown in figure 4.12. The Hall coefficient obtained for MRG, has the value $R_H = -4.405 \times 10^{-10}$ m^3 C^{-1} which is at least an order of magnitude higher than other ferromagnetic and ferrimagnetic samples. The higher value of the Hall coefficient is due to low carrier concentration at the Fermi level, as MRG is highly spin-polarized material, with only one spin-band which contributes at the Fermi level. R_{xy}^{PHE} was measured by rotating the magnetic field in the plane of sample. Figure 4.13 shows the anisotropic magneto-resistance (AMR) and PHE measured at

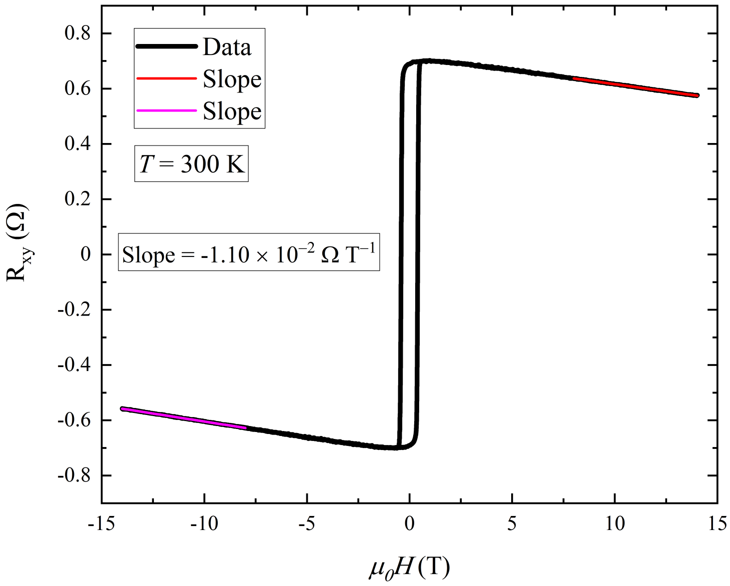

Figure 4.12: AHE measured on Hall bar at 300 K. The contribution of ordinary Hall effect is calculated by evaluating the slope of the data at high magnetic field ($|\mu_0 H| > 8$ T)

room temperature in the presence of a magnetic field of value 1.9 T. The observed

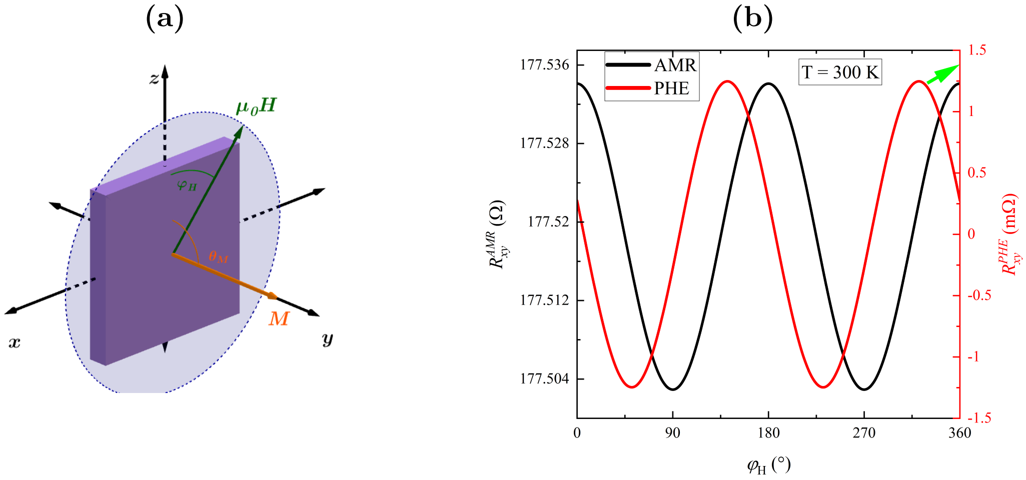

Figure 4.13: (a) AMR and PHE measurement geometry, a magnetic field $\mu_0 H = 1.9$ T is rotated in the plane of the sample xz-plane, (b) resultant AMR and PHE curve.

PHE is three orders of magnitude smaller than the recorded AHE, hence it can be safely ignored from equation 4.25. AMR ratio of MRG evaluated at 300 K is about 0.02 %, whereas PHE ratio has value of around 200 %. Therefore, the only dominant contribution in transverse Hall voltage remains the AHE.

In order to probe the out of plane anisotropy constants, measurement geometry shown in figure 4.14a is adopted. Here, the sample is rotated in such a manner that applied magnetic field effectively rotates in the yz-plane. Fig. 4.14b show the

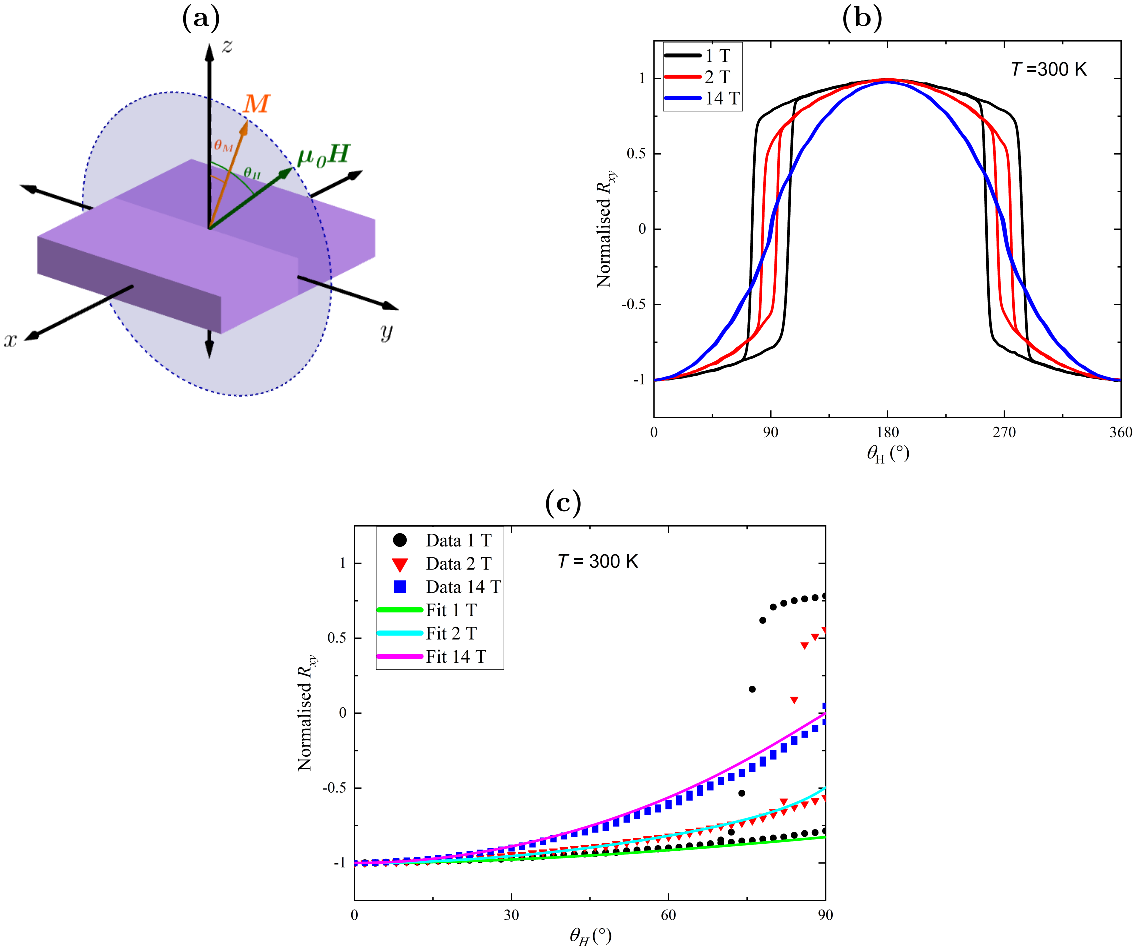

Figure 4.14: (a) Out of plane measurement geometry to investigate the anisotropy constants K_1 and K_2. (a) Magnetic field is rotated in the yz-plane, (b) resultant AHE data recorded for 1 T (black), 2 T (red) and 14 T (blue). (c) Data and corresponding torque modelled curves for the coherent rotation of magnetization vector. The resultant first and second order out-of-plane anisotropy constants of MRG are $K_1 = 4.0 \times 10^4$ J m^{-3} and $K_2 = 2.54 \times 10^4$ J m^{-3} respectively.

rotational AHE loop measured at $T = 300$ K, under constant applied magnetic field of values from 1 T, 2 T, and 14 T. The measured data shows two different regimes, first a continuous change in the Hall resistance (non-hysteretic segments), which is due to the smooth coherent rotation of magnetization vector against the anisotropy field, and secondly an abrupt change in Hall signal (hysteretic segments) due to switching of magnetization vector from out-of-plane to into the plane or vice-versa. The non-hysteretic part of the data can be fitted within torque model by solving the equations 4.21 and 4.22. It should be noted that anisotopy constants are independent of the applied external field (at least up to first order). Therefore, the non-hysteretic parts of the signals can be fitted with common fitting parameters.

The equilibrium position of magnetization vector under the influence of external magnetic field is numerically obtained by solving equations 4.21 and 4.22. The solutions are obtained under the conjugate gradients algorithm, using simultaneous fitting of all data. The same is performed with the optimized Leveberg-Marquard algorithm. Figure 4.14c represents the data recorded with the corresponding best fits. It is clear that all the data are in a good agreement to the model with the anisotropy constants of value, $\frac{K_1}{M} = 0.655\,\mathrm{T}$ and $\frac{K_2}{M} = 0.416\,\mathrm{T}$, here M is the magnitude of saturation magnetization vector. The saturation magnetization of the sample obtained form SQUID measurement is $61\,\mathrm{kA\,m^{-1}}$. Therefore $K_1 = 4.0 \times 10^4$ J m^{-3} and $K_2 = 2.54 \times 10^4$ J m^{-3} is the first and second order out-of-plane anisotropy constants of MRG. It should be noted that in this measurement geometry, AHE is insensitive to the in-plane anisotropy due to the absence of azimuthal rotation of magnetization vector. The in-plane anisotropy constant (K_3) can be investigated in a measurement geometry, where the azimuthal direction of magnetization is varied. In order to probe the in-plane anisotropy, AHE is recorded in the measurement geometry shown in figure 4.15a. Here, the sample is rotated in such a manner that the applied magnetic field effectively rotates in the xz-plane. The magnetic energy landscape, plotted using equation 4.20, reveals the four-fold oscillation of polar position (θ_M) of magnetization vector as a function of φ_M (see figure 4.11). Therefore, the inplane anisotropy allows the AHE signal to oscillate as a function of the azimuthal angle (φ_M) of the magnetization vector. Figure 4.15b and 4.15c show the scans collected at 300 K when a constant magnetic field of 1 T and 1.5 T were respectively applied in the plane of sample. Here the unequal amplitude of oscillation is due to a small offset ($\sim$ 5 deg) of the sample from the xz-plane. Consequently, sample wobbling in the course of rotation leads to an additional term effecting the magnetization vector position θ_M. The equilibrium position of magnetization vector under the influence of external magnetic field is again numerically obtained by solving equations 4.21 and 4.22. The solutions are obtained under the conjugate gradient algorithm and the wobbling contribution has been also taken into consideration under Rodrigues' rotation formula. The extracted value of inplane anisotropy constant is $\frac{K_3}{M} = 0.057\,\mathrm{T}$, or $K_3 = 3.48 \times 10^3$ J m^{-3}, which is an order of magnitude smaller than out of plane anisotropy constants K_1 and K_2. It should be noted that as the

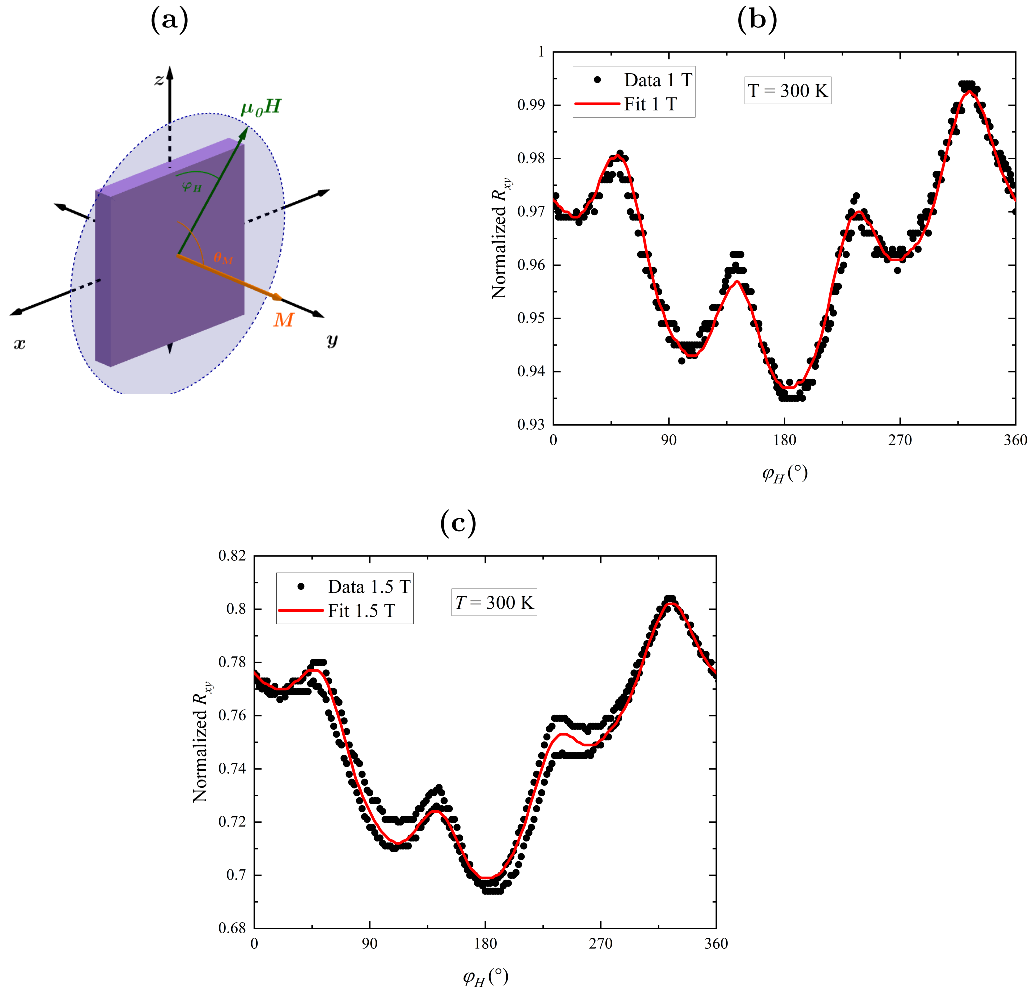

Figure 4.15: (a) Inplane measurement geometry to investigate the anisotropy constants K_3. (a) Magnetic field is rotated in the xz-plane, (b) resultant AHE data recorded for 1 T and corresponding estimated fit under torque model. The presence of unequal amplitude of oscillation is due to small offset ($\sim$ 5 deg) of the sample from the xz-plane, which gives rise to sample wobbling. The estimated in-plane anisotropy constant is $K_3 = 3.48 \times 10^3$ J m^{-3}, which is an order of magnitude smaller than out of plane anisotropy constants K_1 and K_2. (c) AHE data and modeled curve for 1.5 T after inserting the K_1, K_2 and K_3 values. An excellent agreement is observed with effectively no free parameters.

field strength increases, the hysteresis of AHE become evident (compare figure 4.15b and 4.15b). This is due to the fact that at high enough magnetic field, wobbling of sample leads to partial switching of the magnetization vector on the sample's z-axis.

4.7 Combined Preisach and torque model

4.7.1 In-plane field hysteresis loop

A pure hysteresis and a pure rotation mechanisms of magnetization vector are discussed in section 4.5 and 4.6 respectively. The complex quasi-static magnetization dynamics can be obtained by combing torque and Preisach model.

In order to study such dynamics, AHE was measured in the measurement geometry shown in figure 4.16a. Here, the magnetic field was swept in the plane of sample (along z-axis) from ±14 T. The recorded AHE signal has a hysteric behavior as

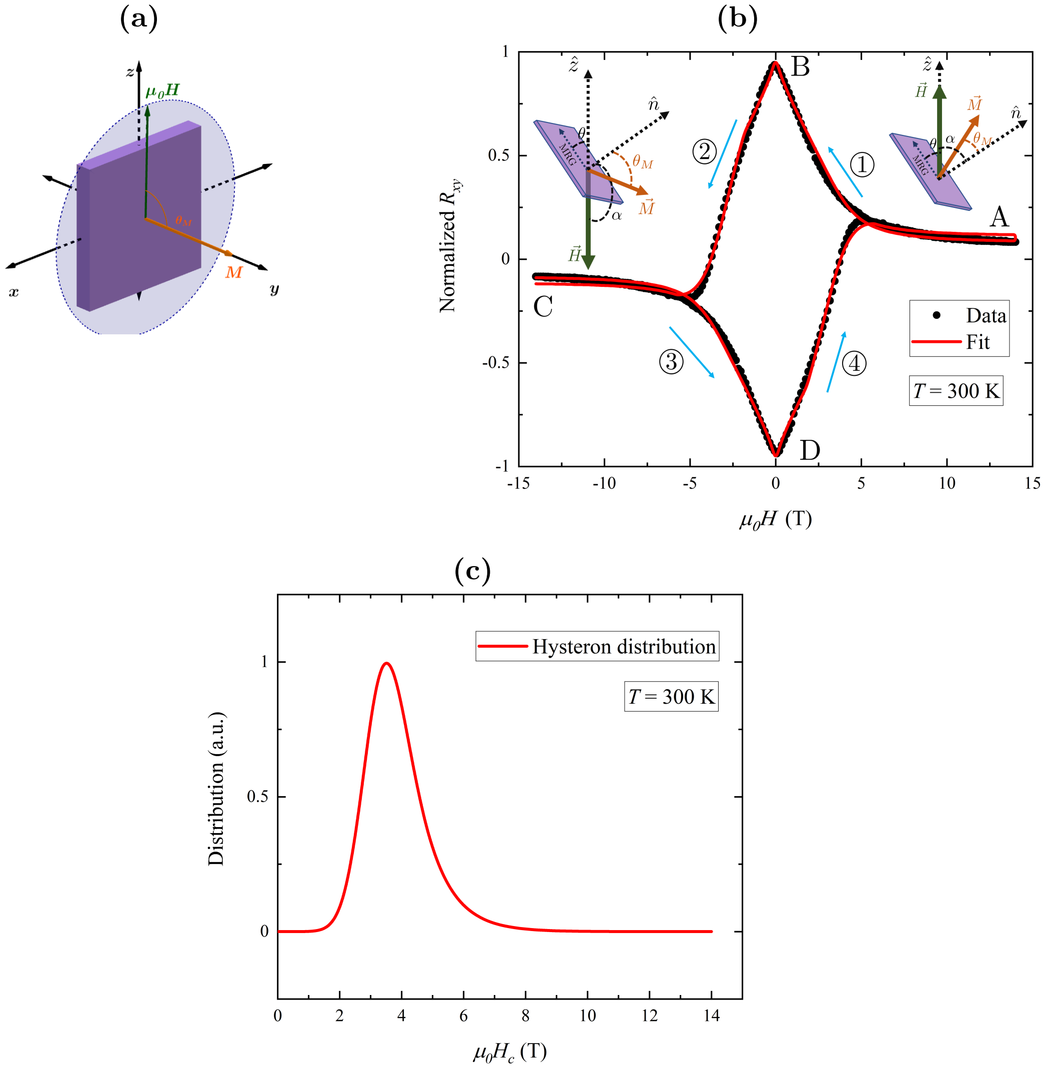

Figure 4.16: (a) In-plane field sweep measurement geometry. (a) Magnetic field is the swiped alsong the z- axis, (b) resultant AHE data recorded for and corresponding estimated fit. Insets highlight the effect of sample offset on resultant curve, see main texts for detailed discussion. (c) Preisach distribution correspond to the combined torque and Preisach model.

shown in figure 4.16b. Due to a small offset (θ) of sample while mounting it on the rotatory stage of the PPMS, the applied magnetic field is not exactly in the plane of sample (see inset of figure 4.16b). The offset of around $\theta \sim 5$ deg, is present and the exact offset value can be evaluated by fitting the data, as discussed later. Consequently, the AHE signal has two different regimes: (i) when magnetic field makes an acute angle with normal to the sample, ($\theta_H < 90$ deg), a coherent rotation of magnetization vector is observed, and (ii) when magnetic field makes an obtuse angle with normal, ($\theta_H > 90$ deg), the switching of magnetic vector occurs when the field projection exceeds the coercive field. Note that coercive field in this scenario is scaled as:

$$H_c = \frac{H_{c_n}}{\cos(\theta_H)} \,, \tag{4.26}$$

here H_{c_n} is the coercivity of MRG sample when magnetic field is applied along the normal direction of the sample ($\theta_H = 0$).

A complete trajectory of magnetization vector (**M**) is described in figure 4.16b. After saturating the sample at 14 T, point **A**, field is reduced to the value of 0 T. Since in this case the angle between the magnetic field (**H**) and the normal vector to the sample, ($\hat{n}$), is less the 90 deg, **M** coherently rotates. Therefore, AHE traces the path-① from the point **A** to point **B**. After that, magnetic field is swept to the value of −14 T from a point **B** to **C** along the path-②. In this case the angle between **H** and $\hat{n}$ is more than 90 deg, hence **M** goes under both rotation and switching at the field strength according to the equation 4.26. A path along ③ results from the coherent rotation of **M**, and the path along ④ again arises due to a combination of rotation and switching of **M**.

AHE curve of figure 4.16b can be defined as:

$$R_{xy} = R_{xy}^{TM} \cdot R_{xy}^{PM} \tag{4.27}$$

where, R_{xy}^{TM} and R_{xy}^{PM} are the contribution from torque and Preisach model respectively. The numerical solution of equation 4.27 is obtained with optimized Leveberg-Marquard algorithm. The values of the anisotropy constants ($K_1/M = 0.655$ T and $K_2/M = 0.416$ T), as obtained in section 4.6, are used while finding the solution of equation 4.27. The resultant estimated curve, along with the data, is shown in figure 4.16b, indicating a very good agreement with the data. Figure 4.16c shows the resultant hysteron distribution. The value of the centre point of distribution (H_{c_0}) is 3.875 T. From equation 4.26 the field angle (θ_H) of value 84.27 deg is obtained, where, $H_{c_n} = 0.387\,\mathrm{T}$ (see section 4.5). Therefore, θ_H obtained from the fitting function is 85.03 deg, also indicating a very close match.

4.7.2 Effective anisotropy approach

Section 4.7.1 describes the fitting of the data shown in figure 4.16b using equation 4.27 under the Leveberg-Marquard algorithm. This method is computationally intensive, as it involves finding a global minima of a rather non-trivial energy surface described by equation 4.27, 4.20, and 4.17.

Therefore, in this section, an alternative approach is discussed to fit such data, where anisotropy constants K_1 and K_2 are replaced with an effective out-of-plane anisotropy field H_{eff}. The equilibrium position of magnetization vector $\mathbf{M}$ can be obtained by balancing the torques acting on it, given by:

$$\mathbf{M} \times \mu_0 \mathbf{H_{eff}} = \mathbf{M} \times \mu_0 \mathbf{H}\,, \tag{4.28}$$

where, $\mathbf{H}$ is the applied external magnetic field. It is evident that finding solution of equation 4.28 is less cumbersome than solving equation 4.21. Figure 4.17 shows AHE data and corresponding fitting curve, where an excellent agreement between data and model is achieved. An effective anisotropy field value of $H_{eff} = 1.458\,\mathrm{T}$ is obtained after fitting the data. While estimating the fitted curve all other parameters corresponding to Preisach model are kept constant as obtained by table 4.1. The analytical value of effective anisotropy field can then be obtained by equating the anisotropy free energy and Zeeman energy. The anisotrpy energy for a tetragonal system can be written as:

$$\begin{aligned} F &= K_1 \sin^2(\theta) + K_2 \sin^4(\theta) \\ &= K_1 + K_2 - (K_1 + 2K_2)\cos^2(\theta) + K_2 \cos^4(\theta)\,. \end{aligned} \tag{4.29}$$

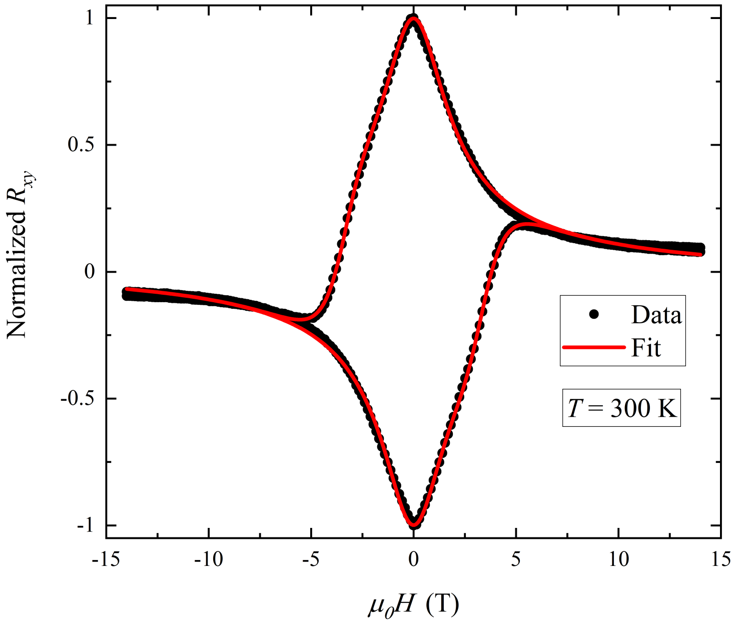

Figure 4.17: AHE data (black dot)when field is swiped in the plane of sample. The estimated fit (red line) using combined Preisach and torque model. An effective out of plane magnetic field approach is utilized in the calculation.

The first two term of equation 4.29, K_1 and K_2 are constants, which provide an offset to the energy equation. Since, the equation of motion of magnetization vector is independent of offset terms, equation 4.29 can be written as:

$$\begin{aligned} F &\approx -(K_1 + 2K_2)\cos^2(\theta) + K_2\cos^4(\theta) \\ &\approx \left[-(K_1 + 2K_2)\cos(\theta) + K_2\cos^3(\theta)\right]\cos(\theta)\,. \end{aligned} \tag{4.30}$$

Now, the Zeeman free energy is given by:

$$\begin{aligned} G &= -\frac{1}{2}\mathbf{M}\cdot\mathbf{B_{eff}} \\ &= -\frac{1}{2}MB_{eff}\cos(\theta)\,, \end{aligned} \tag{4.31}$$

where, the factor of 1/2 arises from taking into account all surrounding magnetic moments. Therefore, the effective magnetic field can be obtained by equating equation 4.31 and 4.30, as shown below:

$$B_{eff} = \frac{2}{M}\left[-(K_1 + 2K_2)\cos(\theta) - K_2\cos^3(\theta)\right]\,. \tag{4.32}$$

Therefore, B_{eff} depends on the θ position of the moment. The mean value of effective field can be written as:

$$\overline{B_{eff}} = \frac{1}{\theta_f - \theta_i} \cdot \int_{\theta_i}^{\theta_f} B_{eff}(\theta) \mathrm{d}\theta \,, \tag{4.33}$$

where, θ_i and θ_f are the initial and final position of magnetization. After plugging the initial and final position of moment (see figure 4.17) into the equation 4.33, mean effective anisotropy field of value 1.467 T is obtained. This value is very close to value obtained (H_{eff} = 1.458 T) within the effective anisotropy approach, as described above. Therefore, a discrepancy of less than 0.6 % between B_{eff} obtained under analytical calculation and the fitting model highlights the success of effective anisotropy approach in investigating the complex magnetic dynamics in the system.

4.7.3 Out-of-plane rotational hysteresis loop

The effective anisotropy model, discussed in section 4.7.2, can be utilized to describe other complex magnetization dynamics, where both the rotation and abrupt switching mechanisms are involved.

In this attempt, AHE data is recorded in a measurement geometry shown in figure 4.18a. Here, a constant applied magnetic field is rotated in the yz-plane. The resultant AHE data measured at 1 T, 2 T and 14 T are shown in figure 4.18. In these case, Zeeman torque on the magnetization vector competes against both out-of-plane anisotropy and applied magnetic field. For a magnetic field of value smaller or comparable to the strength of the anisotropy field, hysteretic phenomena are clearly observed, as shown in figure 4.18b and 4.18c. However, as the strength of magnetic field increases, the equilibrium position of the magnetization vector begins to be dominate by the Zeeman term. In other words, the moment follows the magnetic field orientation. Consequently, the observed AHE data roughly indicates a cosine behaviour. A similar AHE signal at 14 T is shown in figure 4.18d, where an abrupt switching of the magnetization is observed around the angle of 96 deg, consequently an abrupt change in the Hall signal is also observed. Since, the strength of applied magnetic field is much larger than the effective out-of-plane anisotropy field (B_{eff} =1.458 T), the hysteretic behaviour diminishes.

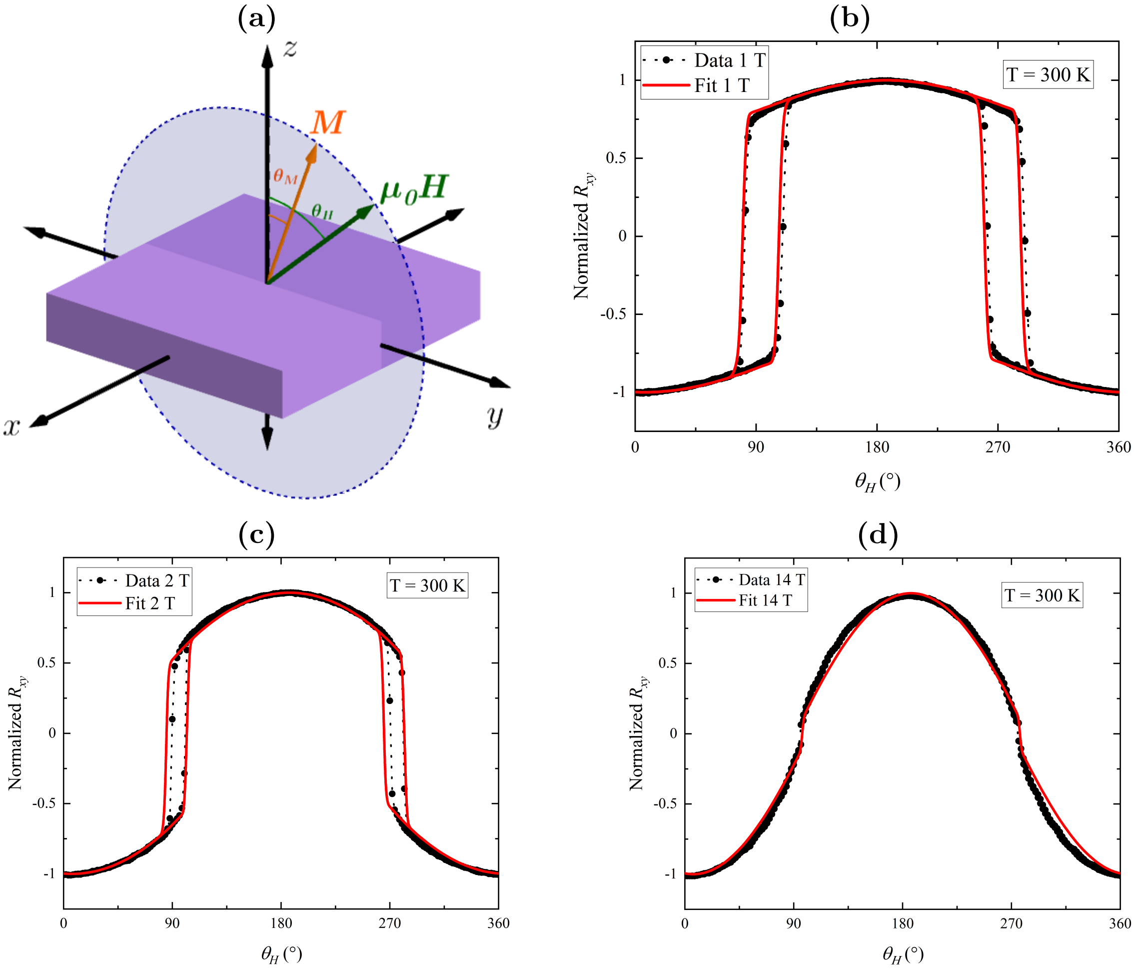

Figure 4.18: (a) Measurement geometry utilized to investigate complex magnetization dynamics. Here the field is uniformly rotated in the yz-plane (b) Rational AHE curve for the 1 T field, black point is the recorded AHE data and red line is the calculated curve from combined Preisach and torque model. (c) AHE data at 2 T and matching calculated curve (red line), (d) Data and calculated curve at 14 T.

In figure 4.18, the red line is the calculated AHE signal under the combined Preisach and torque model. Note that, all the curves are obtained by fixing the values of all the parameters, such as B_{eff}, Presiach distribution and magnetic viscosity coefficient as evaluated in the previous sections. It is evident that all calculated curves show an excellent agreement with the recorded data.

4.8 Conclusions

In this chapter, a comprehensive method is proposed to determine the anisotropy constants of a low-magnetic-moment sample, MRG thin-film, by means of AHE. Out of plane anisotropy constants of value $K_1 = 4.0 \times 10^4$ J m^{-3} ($K_1/M = 0.655$ T) and

$K_2 = 2.54 \times 10^4$ J m^{-3} ($K_2/M = 0.416\,\mathrm{T}$) and in-plane anisotropy constant of value, $K_3 = 3.48 \times 10^3$ J m^{-3} ($K_3/M = 0.057\,\mathrm{T}$) are deduced by fitting the anomalous Hall voltage curve with torque model under the macrospin approximation. First order reversal curve (FORC) and classical Preisach hysteresis (hysterons) model has been successfully implemented to describe the hysteresis behaviour of MRG. In addition, a number of complex quasi-static magnetization dynamics dependencies were successfully estimated with virtually no free parameters, utilizing a combined Preisach and torque model. An excellent agreement between the observed data and calculated model values is realized in all cases. Therefore, the proposed method can be extended to study both linear and non-linear quasi-static dynamics of magnetization vectors in an external field and/or current induced effective fields caused by spin-orbit torque or spin-transfer torque.

5

Spin-orbit torques in a single layer of $\mathrm{Mn_2Ru}_x\mathrm{Ga}$

5.1 Introduction

Modern day information technologies rely on controlling and storing bits ("0s" and "1s") temporarily or permanently. In the state of nanoscale magnets, a popular methods have also emerged in the last couple of decades where manipulation of number of spin provides alternative approaches to taping the richness of information technologies [116]. For example, magnetic tapes and hard discs still dominate the secondary nonvolatile memory in the market due to their low cost and high capacity. However, these nonvolatile memory unit are very slow (≈10 ms) as compared to main memory unit (≪100 ns), such as dynamic random access memory (DRAM). To mitigate this issue, several alternative high-speed nonvolatile memory systems such as flash memory, phase change memory, magnetic race track memory and magnetoresistive random access memory (MRAM), have been extensively pursued.

The magnetic-based memory often requires the use of bulk and cumbersome magnetic coils, which is energy intensive and non-scaleable. In 1996, Berger and Slonczewski proposed a spin-transfer torque (STT) technique to control the magnetization by electrical means [44, 45]. In STT, transfer of spin angular momentum between two noncollinear magnetic systems controls the magnetic bits of MRAM, thus such memory is named STT-MRAM [117]. STT-RAM has the potential to achieve speed of less than 1 ns read/write operation. The STT is often realized in a MTJ structure, where the two magnetic layers are separated by a very thin (~ 2 nm) insulating layer. Here, the switching efficiency is low and requires a very high write current density ($j > 10^{11}\mathrm{Am}^{-2}$) to effectively perform the task. Due to the high write current requirement, the MTJ structure remains non-durable and degradation of thin insulating layer possess a real challenge to implement it effectively.

As an alternative to STT-MRAM, a new type of current-induced torque have been proposed where spin-orbit torque (SOT) plays the central role, known as SOT-MRAM [118, 119]. The SOT provides a better and potentially more efficient writing scheme. SOT is generated through spin-orbit coupling in a bulk material or in heterostructures, where an electric field generates nonequilibrium orbital occupation through spin Hall effect [46], Rashba-Edelstein effect [120], and orbital Hall effect [121]. SOT-based devices have the typical features of low power consumption, higher speed, nonvolatility and an excellent compatibility with current CMOS technologies. More interestingly, SOT-based devices usually have separate read and write path, which avoids exposing the ultra thin tunnel barrier to undesired high writing current densities, thus enhancing the reliability and endurance of device. Furthermore, SOT-based devices require only bilayer or even a single layer to realize, in contrast to STT-MTJ, where high quality hetrojunctions are essential. Thus SOT-based devices are relatively easy to design and fabricate. They have numerous application in various modern technologies, such as MRAM, race-track memory, nano-oscillator, and neuromorphic computing.

SOT is more commonly studied for ferromagnetic (FM)/heavy metal (HM) bilayers, where FM layers are often Co, CoFeB, NiFe, etc. while Pt, Ta, W and other heavy metals are used as HM. In these FM/HM bilayers, SOT is generated through two main mechanism namely spin-Hall effect and interfacial Rashba-Edelstein effect (see chapter-1 for more details). In addition, SOT in single layer can be also realized through Rashba-Edelstein effect (REE) if crystal lacks inversion symmetry, such as in (Ga,Mn)As [122] and NiMnSb [123]. The REE has an advantage over other current-induced effects as the generated torque is local, hence it is generally independent of local disorder. It is a bulk effect and hence does not requite special heterostructures to realize.

Železnỳ et al. [124, 125] predicted that the REE effect can also occurs in antiferromagnets with appropriate symmetry, where bulk SOT generates staggered current-induced spin-polarization and hence staggered effective field on each sublattice. This was observed in Mn_2Au [126] and CuMnAs [127], where spin-sublattices occupy inversion related lattice sites. Although, antiferromagnets have advantage over ferromagnets due to their vanishing net magnetic moment and high-frequency dynamics, the electrical manipulation of antiferromagnetic states requires very high current density, $j > 10^{11}\,\mathrm{Am^{-2}}$, even to switch only fraction of antiferromagnetic domains [128, 129].

Interestingly, ferrimagnets combine the advantages of ferromagnets and antiferromagnets, hence provide a greater flexibility for spin-based devices. Similar to antiferromagnets, ferrimagnets show high-frequency dynamics and possibility to acquire zero net magnetic moments by compensating the sublattices magnetic moment through stoichiometry adjustment, such as in rare earth transition metal (RE-TM) alloy CoTb [130], GdFeCo [131] and Heusler alloy Mn_2Ru_xGa [22]. Unlike antiferromagnets, where probing the magnetic state is difficult, ferrimagnets exhibit finite magnetotransport properties, similar to conventional ferromagnets, hence allowing them to be probed easily. In addition, electrons at the Fermi level in ferrimagnets may have close to 100% spin polarization, as observed in Mn_2Ru_xGa. A detail understanding of spin polarization of Mn_2Ru_xGa is exposed in chapter 3. Moreover, it is known that the critical current, I_c, for stable magnetic resonance frequency of oscillation is given by, $I_c \propto \alpha f$, where α is the coefficient of magnetic damping and f is the frequency of oscillation. Ferrimagnets with a band gap at one of the spin sub-band have lower magnetic damping due to the absence of spin dependent scattering from one of the conduction bands (electrons). Thus threshold currents I_c in ferrimagnets are much smaller [132, 133, 134].

Compensated ferrimagnetic materials, like Mn_2Ru_xGa (MRG), perhaps have all the required properties to implement in various spin-based application such as in spin-oscillators, SOT-MRAM , etc. MRG thin-films crystallize in inverse XA structure, space group $F\bar{4}3m$ (see figure 5.1a) with symmetry reduced to $I\bar{4}m2$ due to a substrate induced tetragonal distortion. Moreover, the conduction and hence transport properties are dominated by electrons from Mn^{4c} sites. Thus the symmetry for all the transport properties is reduced to $\bar{4}2m$ corresponding to Mn^{4c} in a tetragonal environment. MRG lacks inversion symmetry, hence an intrinsic spin-orbit torque can also be realized. Lenne et al. [18] have established the presence of both field-like (reactive) and anti-damping-like (dissipative) like torques in a single layer of MRG. Presence of both types of torque in MRG is encouraging as the previous findings suggest the presence of only field-like torque in bulk CuMnAS [127] and $\mathrm{Mn_2Au}$ [126].

SOT field in MRG for the reduce point group $\bar{4}3m$ and $\bar{4}2m$ can be expressed in the form;

$$\mathbf{H}_{\mathrm{sot}} = x_{fl}\begin{pmatrix}1 & 0 & 0\\ 0 & -1 & 0\\ 0 & 0 & 0\end{pmatrix}\cdot\mathbf{E} + x_{dl}\begin{pmatrix}0 & m_z & m_y\\ m_z & 0 & m_x\\ m_y & m_x & 0\end{pmatrix}\cdot\mathbf{E}\,, \tag{5.1}$$

where, $\mathbf{H_{sot}}$ is the current induced effective SOT field in the unit of T and the $\mathbf{E}$ is the bias electric field. x_{fl} and x_{dl} are the coefficient for field-like, independent of magnetization, and damping-like respectively. Thus if $\mathbf{E}$ is along (010), then $\mathbf{H_{sot}}$ can be written as;

$$\mathbf{H}_{\mathrm{sot}} = m_z x_{dl}\mathrm{e}_{\mathbf{x}} - x_{fl}\mathrm{e}_{\mathbf{y}} + m_x x_{dl}\mathrm{e}_{\mathbf{z}}\,, \tag{5.2}$$

where m_i are the component of unit magnetization vector $\mathbf{m}$ along the unit vector e_i. Here, unit of h_{fl}, h_{fl} and $\mathbf{H_{sot}}$ are in $\mathrm{TA^{-1}m^2}$, which is also equivalent to Henry (H). Figure 5.1b shows the schematic of resultant torques acting on magnetization vector. In a linear-regime, where the change in magnetization angle $\Delta\theta_M$ is small, harmonic anomalous Hall voltages measurements allow us to quantify the h_{fl} and h_{dl}.

Lenne et al. [18] have quantified the h_{fl} and h_{dl} in a single layer ($\approx 30\,\mathrm{nm}$) MRG, through harmonic Hall measurements. Figure 5.2a shows the measured third harmonics in the Hall voltage (V_{xy}^{3w}), when magnetic fields are rotated in the plane of sample. An estimated V_{xy}^{3w} curve, as per the equation 5.2, is also shown in figure 5.2b. Here, the applied current had value $j \approx 1 \times 10^{10}$ $\mathrm{Am^{-2}}$ and both first and third harmonics signals were recorded to minimized the thermal contribution[1] to the signal. It can be seen from figure 5.2 that all the features of the data such as two deep minima at high magnetic field, $\mu_0 H_x = \pm 2\,\mathrm{T}$, the four-fold peaks arising from four-fold in-plan isotropy of MRG, and a shallow minimum at very low magnetic

---

[1] Anomalous Nernst effect has same symmetry of 2ω.

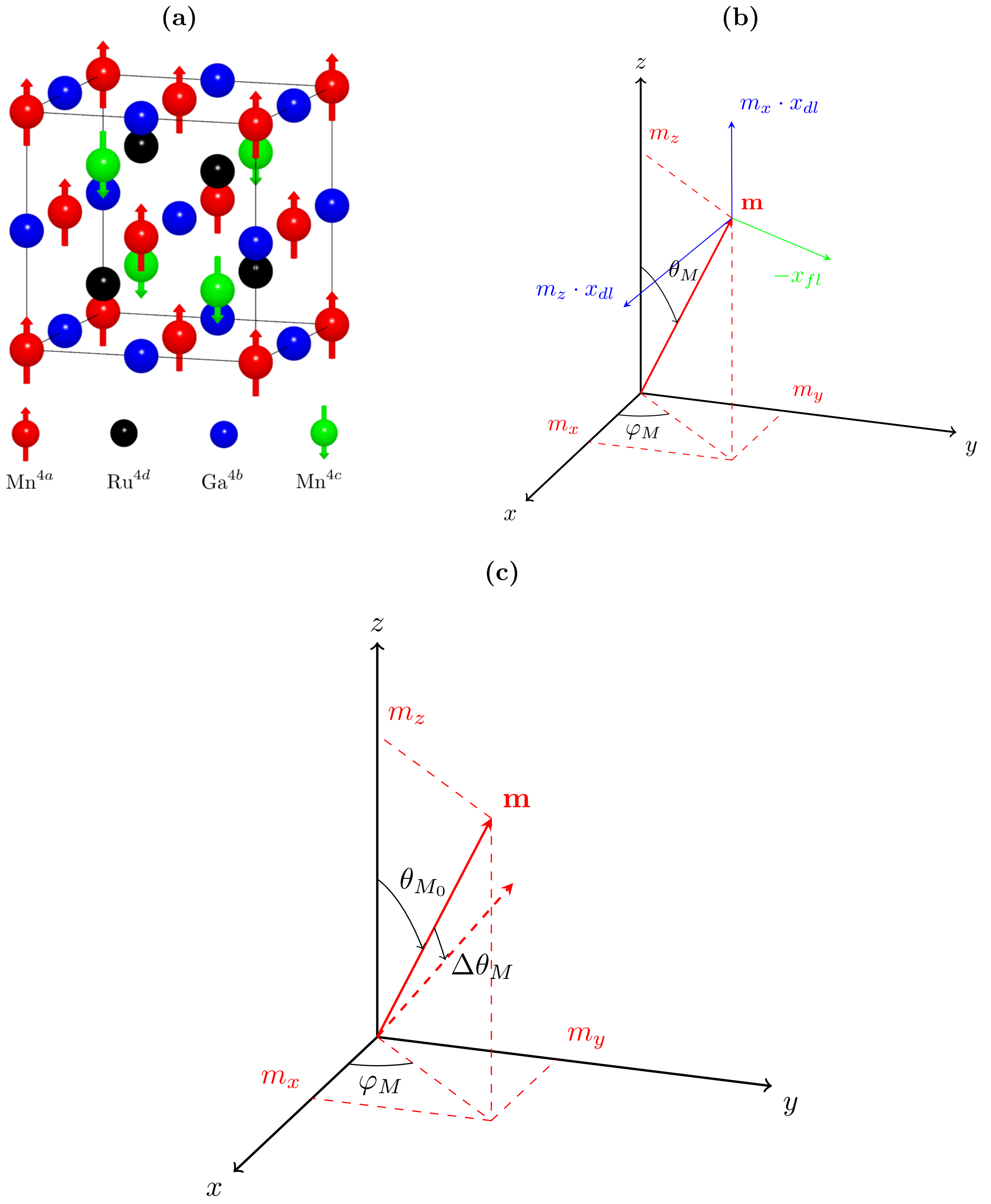

Figure 5.1: (a) Crystal structure of MRG, where Mn^{4c} site has $\bar{4}3m$ group symmetry. (b) An illustration of co-ordinate system for the magnetization vector **m** along with the current induced torques acting on it when current is biased along [010], (c) An illustration of change in magnetization vector angle $\Delta\theta_M$ from the equilibrium position θ_{M_0} when current induced SOTs act. In the case of a linear regime, $\Delta\theta_M$ is very small.

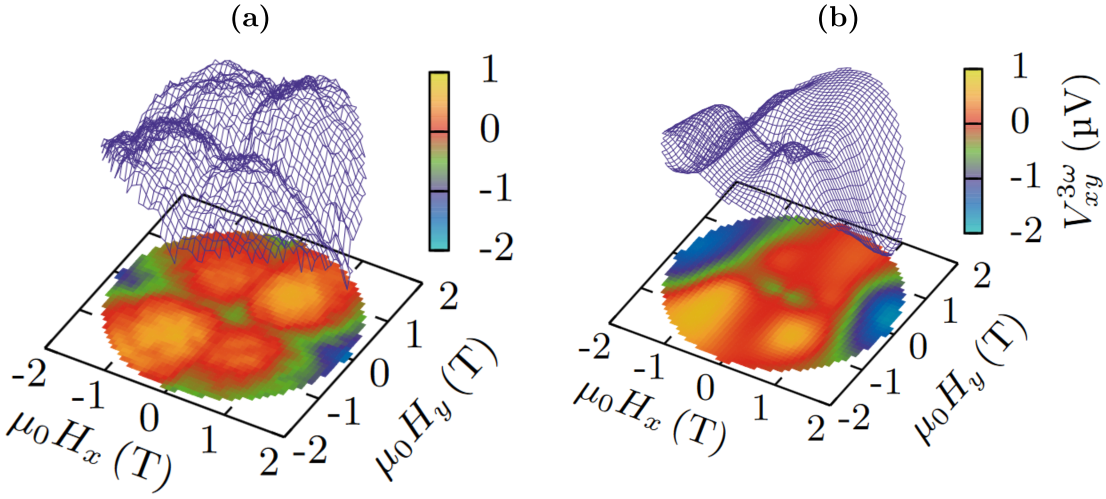

Figure 5.2: (a) Surface and corresponding projection plot of data obtained for anomalous Hall voltage in third harmonics, $V_{xy}^{3\omega}$. Fields are rotated in the plane of sample while bias current, $j \leq 1 \times 10^{10}\,\mathrm{Am^{-2}}$, is kept constant (b) Estimated $V_{xy}^{3\omega}$ as per the equation 5.2, in a linear regime. It is evident that estimated curve matches the data very closely. The picture is after Lenne *et al.* [18].

field closely matches with the estimated curve. The coefficients corresponding to the computed plot are; $x_{fl} = -15 \times 10^{-13}\,\mathrm{TA^{-1}m^2}$ and $x_{dl} = 50 \times 10^{-13}\,\mathrm{TA^{-1}m^2}$. The obtained effective SOT fields in MRG are at least an order of magnitude higher than the effective field usually obtained for FM/HM bilayers. Furthermore, in FM/HM the SOT scales inversely with the thickness of FM layer and hence it quickly diminishes beyond a few nm. On the other hand, the SOT realized in MRG is a bulk property (as obtained in 30 nm) and can be scaled up, provided the current density remains the same. SOT in MRG acts on Mn^{4c} lattice, which has finite moment at the total magnetic compensation point, therefore, SOT in MRG permits it to be implemented in various magnetoresistive applications even in the vanishing net moment scenario.

SOT in MRG was previously performed in a linear regime, where the applied current density was kept small enough, $j \leq 1 \times 10^{10}\,\mathrm{Am^{-2}}$. The advantage of working in the linear regime is that one can derive an approximate analytical solution[2] for the Hall voltage in its various harmonics, utilizing the symmetry of sample (see equation 5.1 and 5.2), which provides a root to quantify the current induced SOT parameters. Since linear regime has additional other competitive effects (such as

---

[2] In case of small $\Delta\theta_M$ the Taylor expansion about the equilibrium position θ_{M_0} can be reduced to linear or up to quadratic terms. However, for a non-linear case this is no longer valid.

Nernst effect, planner Hall effect) which has same symmetry of SOT, this method may leads to spurious quantification of SOT. Moreover, the presence of defects, disorders and distribution of crystalline order leads to a non-trivial transfer SOT tensor (see equation 5.1) which simply can not be linearized. Also, in case of high bias current density, the linear assumption no longer valid.“ Therefore, in this chapter, an alternative phenomenological approach will be presented, where the effective SOT field is evaluated in terms of an effective in-plane field.

5.2 Methodology

Mn_2Ru_xGa thin-films, with $x = 0.7$, were grown on MgO (001) single crystal substrate using the DC-magnetron sputtering technique. The films were prepared by co-sputtering from Mn_2Ga and Ru targets, while maintaining the substrate temperature at 350 °C. The desirable Ru content in Mn_2Ru_xGa were achieved by altering the power delivered to Mn_2Ga target and keeping the power to Ru target constant. After the deposition of MRG, a thin protective layer of AlO_x (~ 2 nm) was deposited to prevent any further oxidation of the active layer. The standard X-ray crystallographic techniques were used to investigate the crystalline order, thickness, density and roughness of the films. More details on sample preparation and characterization are shown in section 3.2. The growth mode of MRG is coalescing-island-like with a high degree of in-plane order. The epitaxial relation of growth is MRG [001] || MgO [001] and MRG [110] || MgO [100]. Due to nature of growth technique used, MRG [100] and MRG [010] directions are essentially equivalent. The deposited film has thickness of 30 nm and a roughness of ≤ 0.7 nm. For the electrical analysis of sample, a number of Hall bars, with varying dimensions, were fabricated on the blanket film using standard photolithography and Ar-ion etching techniques. The contact pads were established with a lift-off process after depositing Ti/Au contacts. The resultant Hall bar has an active length along MgO [110], hence along MRG [100] or [010]. Harmonic measurements of the anomalous Hall effect (AHE) were performed using SR830 lock-in amplifiers in a PPMS system, with a field upto ± 14 T. The samples were rotated in a constant magnetic field using the high resolution sample rotator option. Corrections and calibrations of amplitude and phase of the lock-ins were carefully performed by analysing the amplitude and frequency response of a standard resistor.

5.3 Spin-orbit torque in a high current limit

The presence of high current-induced field, (H_{SOT}), in the low current density limit (linear limit) [18] suggest that a high H_{SOT} should also be observable in high current density (non-linear) limit. A non-linear regime is realized when $\Delta\theta_M$ is large (see figure 5.1c). In order to investigate the non-linear regime, harmonic Hall measurements (V_{xy}) were performed at 310 K. The central idea to evaluate the SOT field is to determine the transfer function which relates the induced effective field and current, as described by Železnŷ et al. [125, 124]. In the linear regime, the transfer function can be evaluated by the symmetry of the sample, on the contrary in the non-linear regime a full tensor SOT relation can not be established. In order to determine the contribution of the non-linear SOT, here, a phenomenological approach is considered. The central idea behind the approach is to normalize the SOT induced change in the magnetization angle, θ_M, with independently measured magnetization dynamics of MRG in presence of external magnetic field. Thus, it allows us to establish the equivalence relation between current and external field-induced perturbation.

In order to realize such relation, measurements begin with measuring AHE in the first and third harmonics, and the first order contribution of SOT, V_{xy}^{SOT}, is corrected by considering the Fourier coefficient of the AHE signal, given by;

$$V_{xy}^{SOT} = V_{xy}^{\omega} + 3V_{xy}^{3\omega}\,, \tag{5.3}$$

where, V_{xy}^{ω} and $V_{xy}^{3\omega}$ are the AHE signal recorded in first and third harmonics.

The experiments were performed on a Hall bar, where the transverse and longitudinal voltage on the first and third harmonics are collected simultaneously using lock-in demodulation techniques. The measurements begin with saturating the sample in a high magnetic field perpendicular to the plane so that all magnetic states are aligned along the easy axis. After that, a magnetic field of 0.4 T is rotated in the plane of the sample (see figure 5.3a). AHE signals are collected for various

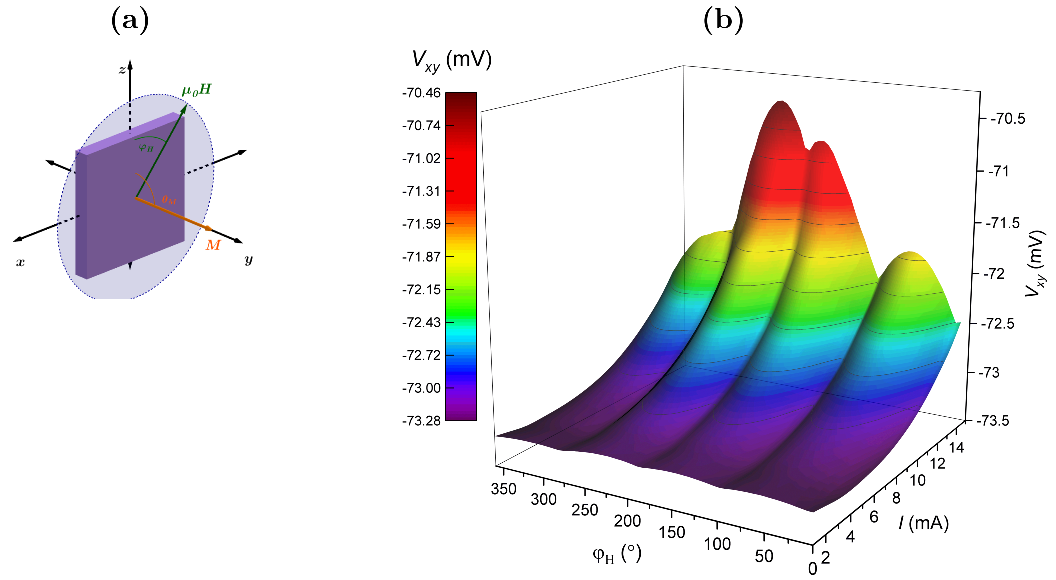

Figure 5.3: (a) A measurement geometry for AHE, where field is rotated in the plane of sample (xz-plane), (b) Resultant AHE data for different values of applied current ranging from 1 mA to 14 mA. The four fold in the signal is mainly attributed to the in-plane anisotropy of the Mn_2Ru_xGa while the high non-linear peak a the high current density is the result of SOT.

field angles, φ_H, at different bias currents, followed by correction as per the equation 5.3. The applied current had value from 1 mA to 14 mA, which corresponds to a current density of 0.2×10^{10} Am^{-2} to 2.5×10^{10} Am^{-2}. Figure 5.3b shows the corrected AHE data as a function of φ_H and current (I). For a small applied current (1 mA $\leq I \leq$ 8 mA), the contribution of non-linear SOT is subtle. In this current range the four fold anisotropy of MRG dictates the AHE signal. However, in the higher current limit (8 mA $\leq I \leq$ 14 mA), a non-linear contribution in AHE begin to appear. For the high value of current the effective SOT field, which is along the z-direction, (see figure 5.1b), modulates the four fold anisotropy dominated signal with two fold out-of-plane signal. SOT field depends on the magnetization direction (θ_M and φ_M), where, the signal peaked at around 180 deg. To established that the peak of the signal is attributed to current induced phenomena only, AHE were recorded for both clockwise and anti-clockwise field rotation, as shown in figure 5.4. The presence of peaks at different field angle, φ_H, indicate the hysteretic properties of the magnetization under the current-induced field. However, the induced effect at high currents have contributions from both SOT and thermal effects. Since, SOT from induced spin-polarization effect is mainly dominated by the polar position,

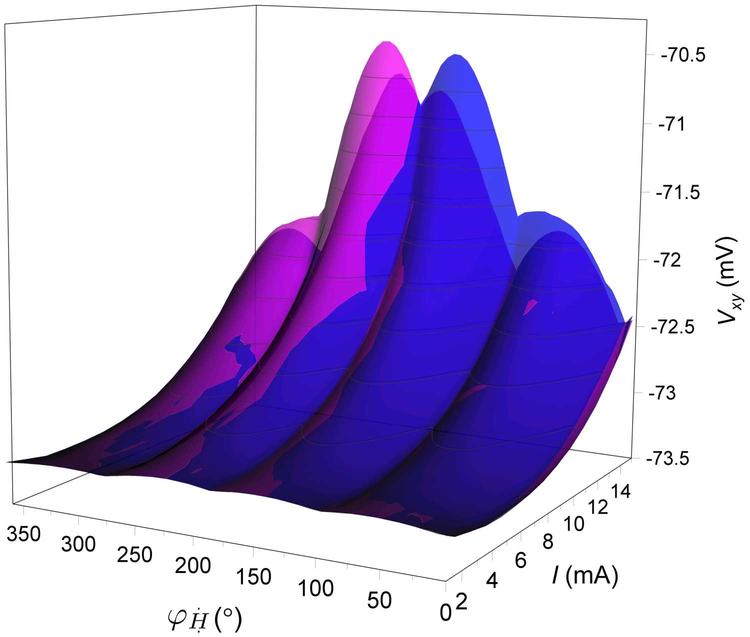

Figure 5.4: AHE measurements when field is rotated clockwise (magenta) and anti-clockwise (blue) direction. Since, the maximum for clockwise and anti-clockwise rotated AHE curve happens at two different angle, it indicated the presence of current induced hysterics phenomena. As any thermally induced effect is rotationally symmetric, the hysteresis must be a current induced effective field phenomena.

(θ_M), and azimuthal angle (φ_M)[3], of magnetization vector, any φ_H independent contribution is mainly the thermally induced phenomena. Hence, thermal contribution can be subtracted by considering the AHE at an angle, φ_H far from the 180 deg position, where SOT effect is dominating, as shown in figure 5.5.

Figure 5.6 show the signal after removal of the thermally induced contributions. The remaining non-linearity in the signal is attributed mainly to the SOT. It should be noted that by subtracting the φ_H independent part, we removed the second order contribution of SOT field which depends on the φ_M as well. Here, we ignore the second order correction of SOT in φ_M as it is assumed to be small.

To quantify the SOT field of figure 5.6 a phenomenological approach was established where the SOT field is normalized in terms of an in-plane effective field. In order to evaluate the relation, magnetic field of ± 14 T were swept in the plane of sample, such that the relation between magnetization angle (θ_M) and in-plane field can be established. Note that, θ_M can be directly obtained using normalized AHE signal, v_z, as shown by equation 3.1. The resultant hysteresis loop is shown in

---

[3] In case of MRG $\varphi_M \approx \varphi_H$ due to ralatively weak in-plane anisotropy, as shown in section 4.6.

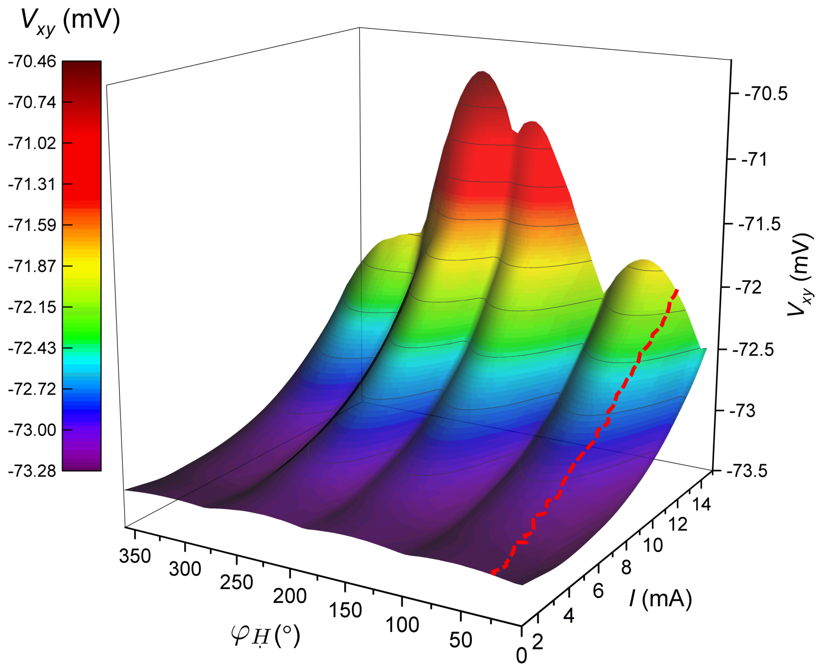

Figure 5.5: AHE data where the thermal contribution is highlighted along a small angle φ_H =30 deg with a red dashed line. The thermal effect is evaluated and subtracted as discussed in the main text.

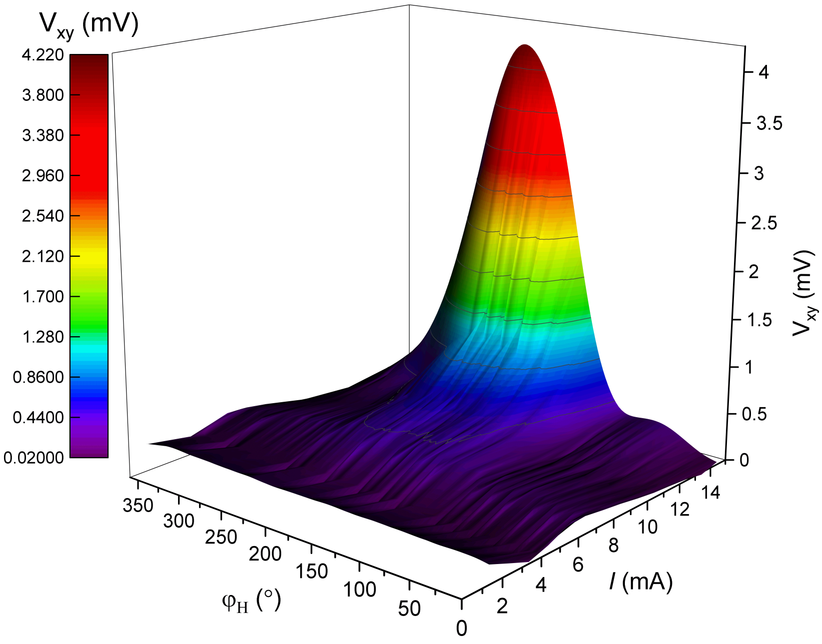

Figure 5.6: AHE data after subtracting the thermal contribution. Here, a presence of non-linearity is primarily due to current induced SOT.

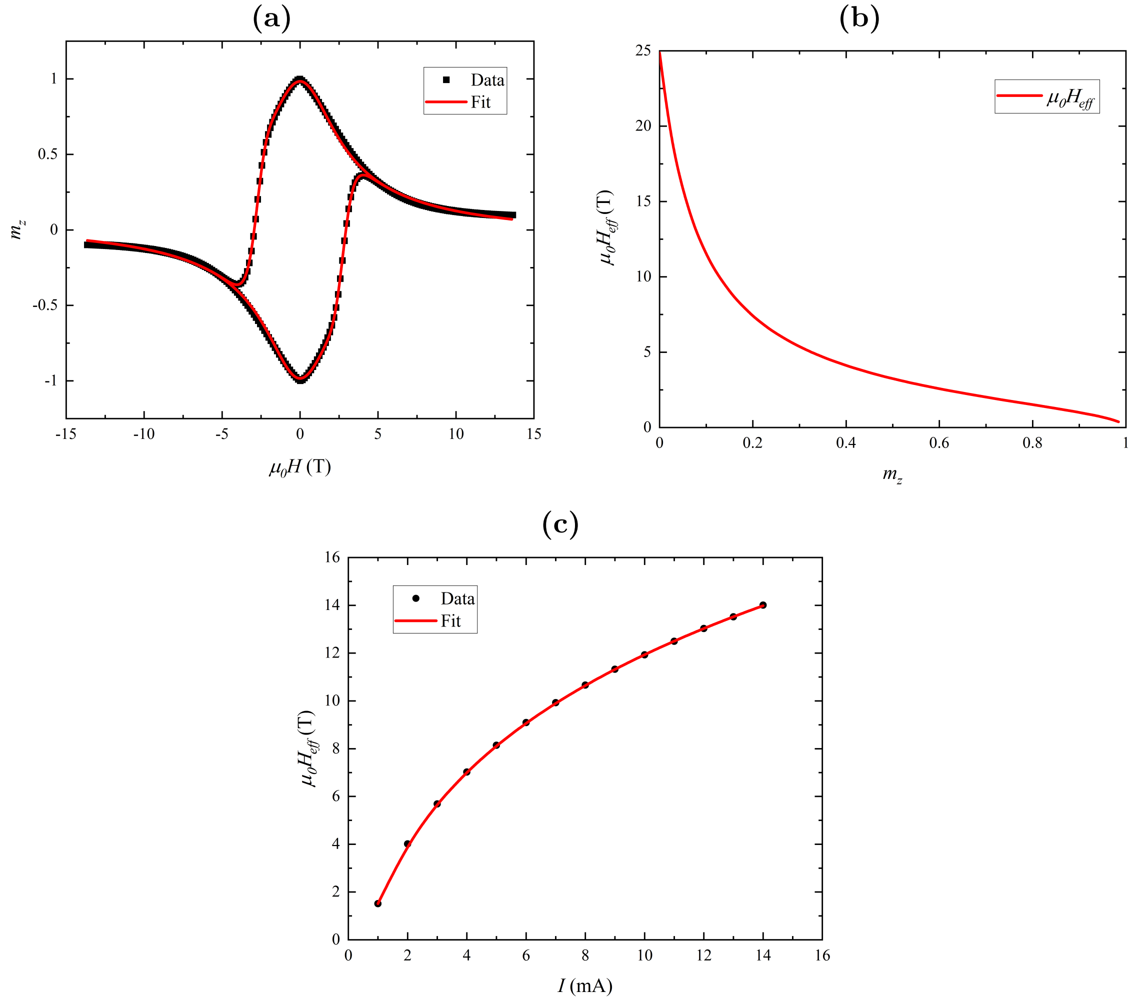

Figure 5.7: A phenomenological approach to quantify the SOT. (a) In-plane field swept to establish the relation between magnetization vector and effective in-pane magnetic field. The fit is obtained under combined torque and Preisach model. (b) Relation established between effective in-plane field and magnetization direction by inverting he model, (c) An estimated thermally driven effective field.

figure 5.7a. The hysteresis data is then fitted with a combined torque and Preisach model, as discussed in section 4.7. An excellent agreement between data and fit is obtained, as shown in figure 5.7a. Therefore, the relation between magnetization angle θ_M and effective in-plane field were established by taking the numerical inversion of combined torque and Preisach model. Figure 5.7b shows the relation between effective in-plane field and magnetization direction, as derived from v_z. Furthermore, the φ_H independent, (thermally induced), contribution, as discussed for figure 5.6, can also be calibrated with this inversion relation. The relation between thermally induced effective field and current is shown in figure 5.7c. A monotonically increasing thermal driven effective field with increasing current suggest a typical thermal

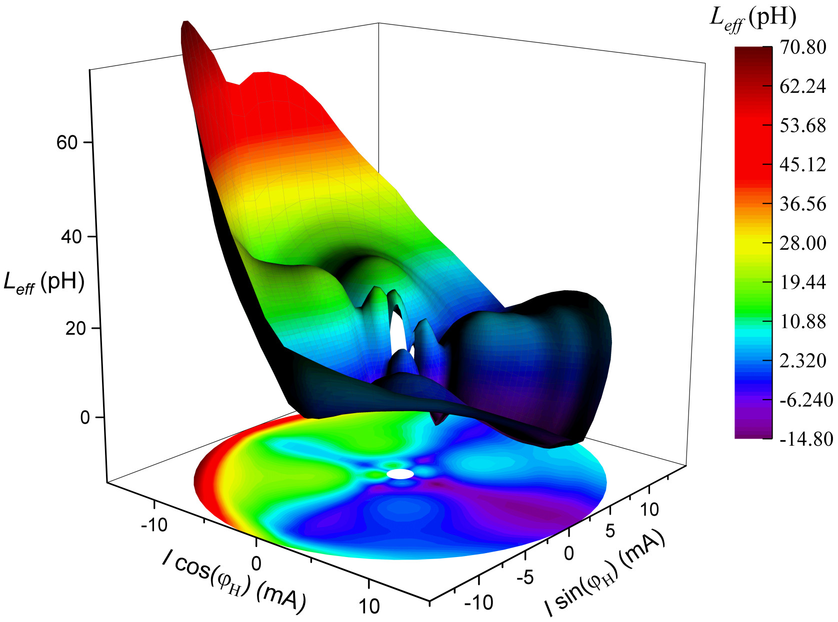

Figure 5.8: A surface and corresponding projection plot for high-current-density effective induction L_{eff} as a function of the bias current and the angle, φ_H. The applied magnetic field has value of 0.4 T. The effective inductance reaches 75 pH, for a current density of $j = 2.5 \times 10^{10}$ A m^{-2}.

gradient produced across a microstructure when most of the heat dissipate along the substrate.

Finally, after subtracting the calibrated φ_H-independent effective field, the resultant SOT contribution is shown in figure 5.8. Here the effective fields are give in term of inductance, pH $= 1 \times 10^{12}$ TA^{-1}m^2. A current of value 14 mA ($j = 2.5 \times 10^{10}$ Am^{-2}) produces an effective inductance of value $L_{eff} \approx 75$ pH around φ_H =180 deg. This is equivalent to an effective in-plane field of strength 1.9 T! A previously reported SOT in MRG under linear-regime have value of $x_{fl} = -15 \times 10^{-13}$ TA^{-1}m^2 (-1.5 pH) and $x_{dl} = 50 \times 10^{-13}$ TA^{-1}m^2 (5 pH), see page 102. Thus effective SOT obtained here in a non-liner regime is at least 15 times stronger and more than two orders of magnitude higher then SOT attained in FM/HM bilayers. This high field has enough strength to magnetically switch $\approx 2\%$ of the sample, as evident from the combined torque and Preisach model.

To further understand if sustained oscillation is obtainable, we consider a standard device structure of 500 nm thickness and 20 µm active length. Such device has an inductance value of around 0.1 pH. Since, the current induced inductance, 75 pH, goes well beyond 0.1 pH, a self oscillation in such device could be attainable though

SOT. The resonance frequency is determined by the larger of the two inductances, i.e. the inductance due to SOT, which pushes the resonance frequency above 0.75 THz [76].

5.4 Conclusions

In summary, an alternative phenomenological method is presented to quantify the current induced SOT in MRG under effective in-plane field. This method spotlights an approach to study the SOT and magnetization dynamics in MRG under non-linear regime. We report that current-induced spin orbit torque in the non-linear regime reaches record values in single-layers of the compensated, half-metallic ferrimagnet $\mathrm{Mn_2Ru_xGa}$. The obtained value is at least 15 times stronger than values previously reported within the linear regime. Moreover, the effective SOT is well in excess of those obtained in bilayer structures. We also deduce that with such a high SOT induced inductance, a sustained magnetic oscillation in MRG is within reach. A crude estimate for such a Hall-bar device suggests that oscillation beyond 0.75 THz is achievable. Therefore, MRG based SOT-oscillators could be a cheap, compact, and tunable alternative for generating and detecting in the THz gap. It will certainly help to claim this new realm of information technologies for magnetics.

6

Conclusions and outlook

6.1 Conclusions

We argue that Mn_2Ru_xGa (MRG) can be projected to become a functional device material in high-frequency magnetics - a prototypical compensated ferrimagnetic half-metal (CFHM), an alternative to zero moment antiferromagnetic half-metal (ZMAHM). As a CFHM, it shows various fascinating properties, common to ZMAHMs, such as the presence of vanishingly small magnetic moment and high-frequency magnetisation dynamics, beside half-metallicity and sizable magneto-transport properties (large anomalous Hall coefficient), which are absent in ZMAHMs. This thesis has clarified some of the key device-relevant parameters of MRG, using precise measurements and interpretation of its structural, magnetic and transport properties. The methodologies deployed include the study of spin-polarization of MRG using PCAR spectroscopy, torque determination using the spontaneous Hall effect, and quasi-static field- and current-induced (SOT) magnetization dynamics. All of these are used to build a coherent picture of this remarkable material and define the envelope of its possible deployment in devices.

One of the crucial properties of MRG is its high spin polarization at Fermi level. Spin-polarization, in this system, depends on various parameters, including stoichiometry and crystal quality. In this line of thought, an investigation of the spin polarization of Mn_yRu_xGa is presented in chapter 3, with various Ru ($x = 0.5, 0.7, \text{and}\, 0.9$) and Mn ($1.6 \leq y \leq 2.4$) content. Spin polarization as high as $\approx 63\%$ was observed for the optimal composition of $Mn_{2.2}Ru_{0.7}Ga$. This high value of polarization begins to drop with both increasing Ru content and decreasing Mn content within $\mathrm{Mn_yRu}_x\mathrm{Ga}$. We attribute the former to an enhanced contribution of the s-like bands near the Fermi level, in addition to a shift of the Fermi level, due to the pair of electrons, contributed from each Ru atom. A degradation of crystal quality with lower Mn content in $\mathrm{Mn}_y\mathrm{Ru}_{0.5}\mathrm{Ga}$ is here associated the increase in site-disorder and spin-mixing, which then accounts for the quick drop in spin-polarization. A key take-away message is also the presence of a large anomalous Hall angle (AHA $\approx 2\%$) in $\mathrm{Mn_yRu}_x\mathrm{Ga}$. The here-stablished strong correlation between the spontaneous Hall angle and the degree of spin-polarization, justifies an approach to material optimization, where one can be used as a proxy for the other, thus substantially lowering the time and cost needed for device blanket material optimization in this system.

The presence of substrate-induced tetragonal distortion and vanishing small moment in MRG leads to a strong out-of-plane magnetic anisotropy. While this fact was already known at the start of this thesis work, as the detailed knowledge of the rather complicated anisotropy profile of MRG is a prerequisite for the interpretation and quantification of its various other properties properties, particular focus of this work has been to establish a robust methodology for its determination. Probing anisotropy here by the standard torque of magnetometry methods is either challenging or impossible due to the material's low magnetic moment and unavailability in bulk crystalline form. In chapter 4, we have firmly established the utility of a comprehensive method for the determination of anisotropy constants, using the far more sensitive in thin films AHE measurements. Here the torque and Preisach model have been deployed, within a macrospin model, to experimentally evaluate the different anisotropy constants of the samples. The primary out-of-plane anisotropy constant $K_1 = 4.0 \times 10^4$ Jm^{-3} ($K_1/M = 0.655\,\mathrm{T}$), $K_2 = 2.54 \times 10^4$ Jm^{-3} ($K_2/M = 0.416\,\mathrm{T}$) and a weak in-plane anisotropy constant $K_3 = 3.48 \times 10^3$ Jm^{-3} ($K_3/M = 0.057\,\mathrm{T}$) are all determined from an overdetermined set of measurements on a MRG ($\mathrm{Mn_{2.2}Ru_{0.7}Ga}$) thin film (patterned into a micron-sized Hall bar). Yet more remarkably, a wide range of complex quasi-static dynamic evolutions were successfully modelled and closely compared with experimental observations, using a combined torque and Preisach model with virtually no free parameters. The high fidelity and predictive power of this new model allows for the direct feeding of parameters into more sophisticated effective Hamiltonian models, integrated via Monte-Carlo and micromagnetic approaches, providing access to the device-relevant close-to-resonance dynamics of the system.

Finally, in chapter 5, we report for the first time, a record current-induced spin-orbit torque (SOT) in a single layer of MRG (i.e. a sample without any heavy metals) within the non-linear regime. The effective SOT fields reach values as high as 75×10^{-12} $\mathrm{TA^{-1}m^2}$ (75 pH) at a current density of $j = 2.5 \times 10^{10}$ $\mathrm{Am^2}$. The obtained value of SOT is, remarkably, one order of magnitude higher than the one previously reported for SOT in MRG, in the liner regime (low current density), but also well in excess of those reported in the literature for arbitrary FM/HM bilayers.

6.2 Outlook

The research on CFHMs, in particular on MRG, elucidates their interesting properties for both in terms of physical understanding and from an applications' point of view. MRG has demonstrated a combination of several fascinating properties as a prototype CFHM and a candidate for application in various spin-based devices. Although there is still a long way to go, before a spintronics device with an MRG active layer becomes part of our everyday life, here, I propose following future directions of research, which may be beneficial not only for the further refinement of the properties of MRG, but also, in general, for an arbitrary CFHM.

The spin-polarization of MRG has reached as high as 63% by tuning its composition. This is one of the highest reported spin-polarization values in Heusler alloy. Therefore, a spin-valve (TMR, GMR) made with MRG should show a very high magnetoresistance ratio. A previous attempt to realize high-TMR ratio in MRG/MgO/CoFeB structures did not result in a very high TMR ratio, ($\approx 40\%$ at 10 K) [79], due to poor tunnel barrier quality, owing to poor growth condition and diffusion of Mn and B into MgO. However, we have recently optimized the RF-sputtering conditions, so that excellent MgO can now be grown on MRG directly, utilizing the fact that lattice mismatch between MRG [100] and MgO [110] is less than 1%. We had already demonstrated that the coercivity of MRG can also be easily tuned in a wide field range, form fraction of Tesla to more that 14 T at the compensation point. Therefore, a MTJ structure could be realized, with both the free and pinned layers made of only MRG. This way it also simplifies the fabrication process, where an MTJ can be made in just 3-4 layers, thus eliminating cumbersome extra layer requirements (antiferromagnetic layers, diffusion barrier, etc.) used in conventional MTJ structures.

More insight into the correlation between spin-polarization and anomalous Hall effect in MRG can be reached by measuring PCAR at various temperatures, particularly near the compensation temperature. However, forcing magnetic compensation below the superconducting critical temperature of Nb ($T_c = 9.2\,\mathrm{K}$) in MRG cannot be easily realized. Therefore, a PCAR study with an appropriate high temperature superconductor may provide further insight into this more fundamental question. The successful application of macrospin combined torque-and-Preisach model to MRG and the determination of the anisotropy constants and the interpretation of the complex quasi-static dynamics, suggests that it can be extended to other potential CFHMs, such as Mn_3Al, $Mn_{1.5}V_{0.5}FeAl$, etc. It will be also intersecting to investigate non-collinear CFHM systems under this model, in order to provide at least a crude estimate for the degree of non-collinearity. Moreover, the proposed simplified effective model approach should be applicable to a wide range of magnetic systems, such as ferrimagnets and sperimagnets, provided that the distributions of interacting hysterons and switching fields are uniquely defined. These distributions can be experimentally determined, with the first order reversal curves (FORCs) method if a system fulfill congruence and wiping-out properties, a necessary and sufficient condition, much as originally suggested by Mayergoyz [95, 102].

As far as research on SOT is concerned, the demonstration of high SOT in MRG suggests that a sustained antiferromagnetic oscillation can be realized in a current in-plane spin-oscillator made with MRG or related material. In this direction, realizing a current controlled spin-oscillator independently or in conjunction with MRG-based MTJs will provide a root to generate a terahertz oscillators and detectors, which are compact integrable and cheap. The last tantalizing future prospect I would like to mention is the possibility to realize measurements of the SOT-induced dynamics, using stroboscopic pulsed laser techniques. Whether SOT can be made useful on the ps timescale and below remains an open question.

A

List of publications

1. **Ajay Jha**, Simon Lenne, Gwenaël Atcheson, Karsten Rode. J. M. D. Coey, Plamen Stamenov, *"Static and low excitation magnetization dynamics in compensated ferrimagnetic half-metal."* (in preparation)

2. K. E, Siewierska, G. Atcheson, **Ajay Jha**, K. Esien, R. Smith, S. Lenne, N. Teichert, et al. *"Magnetic order and magneto-transport in half-metallic ferrimagnetic* Mn_yRu_xGa *thin films."* Physical Review B 104, no. 6 (2021): 064414.

3. Yangkun He, Gerhard H. Fecher, Chenguang Fu, Yu Pan, Kaustuv Manna, Johannes Kroder, **Ajay Jha**, et al. *"A new highly anisotropic Rh-based Heusler compound for magnetic recording."* Advanced Materials 32, no. 45 (2020): 2004331.

4. Rui Zhang, Zsolt Gercsi, M. Venkatesan, **Ajay Jha**, Plamen Stamenov, and J. M. D. Coey. *"Spin liquids and spin glasses in Mn-based alloys with the cubic A13 (β-Mn) structure."* Journal of Magnetism and Magnetic Materials 501 (2020): 166429.

5. Simon Lenne, Yong-Chang Lau, **Ajay Jha**, Gwenaël Atcheson, Roberto E. Troncoso, Arne Brataas, J. M. D. Coey, Plamen Stamenov, Karsten Rode. *"Giant spin-orbit torque in a single ferrimagnetic metal layer." arXiv preprint arXiv:1903.04432* (2019).

References

[1] J. M. D. Coey, *Magnetism and magnetic materials.* Cambridge university press, 2010. (Cited on pages xiii and 4.)

[2] M. Julliere, “Tunneling between ferromagnetic films,” *Physics letters A*, vol. 54, no. 3, pp. 225–226, 1975. (Cited on pages xiv, 13, 14, and 47.)

[3] J. S. Moodera, L. R. Kinder, T. M. Wong, and R. Meservey, “Large magnetoresistance at room temperature in ferromagnetic thin film tunnel junctions,” *Physical review letters*, vol. 74, no. 16, p. 3273, 1995. (Cited on pages xiv, 13, 14, and 47.)

[4] S. Yuasa, T. Nagahama, A. Fukushima, Y. Suzuki, and K. Ando, “Giant room-temperature magnetoresistance in single-crystal Fe/MgO/Fe magnetic tunnel junctions,” *Nature materials*, vol. 3, no. 12, pp. 868–871, 2004. (Cited on pages xv, 13, and 15.)

[5] W. Butler, X.-G. Zhang, T. Schulthess, and J. MacLaren, “Spin-dependent tunneling conductance of Fe—MgO—Fe sandwiches,” *Physical Review B*, vol. 63, no. 5, p. 054416, 2001. (Cited on pages xv, 14, and 15.)

[6] R. Soulen, J. Byers, M. Osofsky, B. Nadgorny, T. Ambrose, S. Cheng, P. R. Broussard, C. Tanaka, J. Nowak, J. Moodera, *et al.*, “Measuring the spin polarization of a metal with a superconducting point contact,” *science*, vol. 282, no. 5386, pp. 85–88, 1998. (Cited on pages xv and 19.)

[7] A. Brataas, A. D. Kent, and H. Ohno, "Current-induced torques in magnetic materials," *Nature materials*, vol. 11, no. 5, pp. 372–381, 2012. (Cited on pages xv and 21.)

[8] D. C. Ralph and M. D. Stiles, "Spin transfer torques," *Journal of Magnetism and Magnetic Materials*, vol. 320, no. 7, pp. 1190–1216, 2008. (Cited on pages xv and 21.)

[9] R. Ramaswamy, J. M. Lee, K. Cai, and H. Yang, "Recent advances in spin-orbit torques: Moving towards device applications," *Applied Physics Reviews*, vol. 5, no. 3, p. 031107, 2018. (Cited on pages xvi and 22.)

[10] D. Betto, N. Thiyagarajah, Y.-C. Lau, C. Piamonteze, M.-A. Arrio, P. Stamenov, J. Coey, and K. Rode, "Site-specific magnetism of half-metallic $\mathrm{Mn_2Ru}_x\mathrm{Ga}$ thin films determined by X-ray absorption spectroscopy," *Physical Review B*, vol. 91, no. 9, p. 094410, 2015. (Cited on pages xvi, 24, and 54.)

[11] M. Buchner, K. Höfler, B. Henne, V. Ney, and A. Ney, "Tutorial: Basic principles, limits of detection, and pitfalls of highly sensitive SQUID magnetometry for nanomagnetism and spintronics," *Journal of Applied Physics*, vol. 124, no. 16, p. 161101, 2018. (Cited on pages xvii and 43.)

[12] K. E. Siewierska, *Development and Characterisation of a Zero-Moment Half-Metal.* PhD thesis, University of Dublin, 2020. (Cited on pages xviii, xix, 53, and 58.)

[13] N. S. Church, K. Fabian, and S. A. McEnroe, "Nonlinear Preisach maps: Detecting and characterizing separate remanent magnetic fractions in complex natural samples," *Journal of Geophysical Research: Solid Earth*, vol. 121, no. 12, pp. 8373–8395, 2016. (Cited on pages xx and 70.)

[14] K. Fabian and T. von Dobeneck, "Isothermal magnetization of samples with stable Preisach function: A survey of hysteresis, remanence, and rock magnetic parameters," *Journal of Geophysical Research: Solid Earth*, vol. 102, no. B8, pp. 17659–17677, 1997. (Cited on pages xx and 70.)

[15] J. M. Feinberg, G. R. Scott, P. R. Renne, and H.-R. Wenk, "Exsolved magnetite inclusions in silicates: Features determining their remanence behavior," *Geology*, vol. 33, no. 6, pp. 513–516, 2005. (Cited on pages xx and 74.)

[16] R. J. Harrison and J. M. Feinberg, "FORCinel: An improved algorithm for calculating first-order reversal curve distributions using locally weighted regression smoothing," *Geochemistry, Geophysics, Geosystems*, vol. 9, no. 5, 2008. (Cited on pages xx and 74.)

[17] V. Franco and B. Dodrill, "Magnetic Measurement Techniques for Materials Characterization," 2021. (Cited on pages xxi and 75.)

[18] S. Lenne, Y.-C. Lau, A. Jha, G. P. Atcheson, R. E. Troncoso, A. Brataas, M. Hayashi, J. Coey, P. Stamenov, and K. Rode, "Giant spin-orbit torque in a single ferrimagnetic metal layer," *arXiv preprint arXiv:1903.04432*, 2019. (Cited on pages xxiv, 51, 100, 102, and 104.)

[19] C. Graves, A. Reid, T. Wang, B. Wu, S. De Jong, K. Vahaplar, I. Radu, D. Bernstein, M. Messerschmidt, L. Müller, *et al.*, "Nanoscale spin reversal by non-local angular momentum transfer following ultrafast laser excitation in ferrimagnetic GdFeCo," *Nature materials*, vol. 12, no. 4, pp. 293–298, 2013. (Cited on page 4.)

[20] S. Alebrand, M. Gottwald, M. Hehn, D. Steil, M. Cinchetti, D. Lacour, E. E. Fullerton, M. Aeschlimann, and S. Mangin, "Light-induced magnetization reversal of high-anisotropy TbCo alloy films," *Applied Physics Letters*, vol. 101, no. 16, p. 162408, 2012. (Cited on page 4.)

[21] M. Ohkoshi, H. Kobayashi, T. Katayama, M. Hirano, and T. Tsushima, "Spin reorientation in $DyCo_5$," *Physica B+C*, vol. 86, pp. 195–196, 1977. (Cited on page 4.)

[22] H. Kurt, K. Rode, P. Stamenov, M. Venkatesan, Y. C. Lau, E. Fonda, and J. M. Coey, "Cubic Mn_2Ga Thin films: Crossing the spin gap with ruthenium," *Physical Review Letters*, vol. 112, no. 2, pp. 2–6, 2014. (Cited on pages 4, 23, 48, 65, 66, and 99.)

[23] R. Stinshoff, G. H. Fecher, S. Chadov, A. K. Nayak, B. Balke, S. Ouardi, T. Nakamura, and C. Felser, “Half-metallic compensated ferrimagnetism with a tunable compensation point over a wide temperature range in the Mn-Fe-V-Al Heusler system,” *AIP Advances*, vol. 7, no. 10, p. 105009, 2017. (Cited on page 4.)

[24] M. E. Jamer, Y. J. Wang, G. M. Stephen, I. J. McDonald, A. J. Grutter, G. E. Sterbinsky, D. A. Arena, J. A. Borchers, B. J. Kirby, L. H. Lewis, *et al.*, “Compensated ferrimagnetism in the zero-moment heusler alloy Mn_3Al,” *Physical Review Applied*, vol. 7, no. 6, p. 064036, 2017. (Cited on page 4.)

[25] E. R. Callen and H. B. Callen, “Static magnetoelastic coupling in cubic crystals,” *Physical Review*, vol. 129, no. 2, p. 578, 1963. (Cited on page 10.)

[26] G. A. Prinz, “Magnetoelectronics,” *Science*, vol. 282, no. 5394, pp. 1660–1663, 1998. (Cited on page 10.)

[27] D. D. Awschalom and J. M. Kikkawa, “Electron spin and optical coherence in semiconductors,” *Physics Today*, vol. 52, no. 6, pp. 33–38, 1999. (Cited on page 10.)

[28] S. D. Sarma, J. Fabian, X. Hu, and I. Žutić, “Spintronics: electron spin coherence, entanglement, and transport,” *Superlattices and microstructures*, vol. 27, no. 5-6, pp. 289–295, 2000. (Cited on page 10.)

[29] G. Binasch, P. Grünberg, F. Saurenbach, and W. Zinn, “Enhanced magnetoresistance in layered magnetic structures with antiferromagnetic interlayer exchange,” *Physical review B*, vol. 39, no. 7, p. 4828, 1989. (Cited on page 11.)

[30] M. N. Baibich, J. M. Broto, A. Fert, F. N. Van Dau, F. Petroff, P. Etienne, G. Creuzet, A. Friederich, and J. Chazelas, “Giant magnetoresistance of (001) Fe/(001) Cr magnetic superlattices,” *Physical review letters*, vol. 61, no. 21, p. 2472, 1988. (Cited on page 11.)

[31] M. A. Ruderman and C. Kittel, “Indirect exchange coupling of nuclear magnetic moments by conduction electrons,” *Physical Review*, vol. 96, no. 1, p. 99, 1954. (Cited on page 12.)

[32] S. Parkin, N. More, and K. Roche, "Oscillations in exchange coupling and magnetoresistance in metallic superlattice structures: Co/Ru, Co/Cr, and Fe/Cr," *Physical review letters*, vol. 64, no. 19, p. 2304, 1990. (Cited on page 12.)

[33] S. S. Parkin, "Systematic variation of the strength and oscillation period of indirect magnetic exchange coupling through the 3d, 4d, and 5d transition metals," *Physical Review Letters*, vol. 67, no. 25, p. 3598, 1991. (Cited on page 12.)

[34] J. Sato, M. Oogane, H. Naganuma, and Y. Ando, "Large magnetoresistance effect in epitaxial $Co_2Fe_{0.4}Mn_{0.6}Si/Ag/Co_2Fe_{0.4}Mn_{0.6}Si$ devices," *Applied Physics Express*, vol. 4, no. 11, p. 113005, 2011. (Cited on page 13.)

[35] T. Miyazaki and N. Tezuka, "Giant magnetic tunneling effect in $Fe/Al_2O_3/Fe$ junction," *Journal of magnetism and magnetic materials*, vol. 139, no. 3, pp. L231–L234, 1995. (Cited on page 13.)

[36] S. S. Parkin, C. Kaiser, A. Panchula, P. M. Rice, B. Hughes, M. Samant, and S.-H. Yang, "Giant tunnelling magnetoresistance at room temperature with MgO (100) tunnel barriers," *Nature materials*, vol. 3, no. 12, pp. 862–867, 2004. (Cited on page 13.)

[37] S. Ikeda, J. Hayakawa, Y. Ashizawa, Y. Lee, K. Miura, H. Hasegawa, M. Tsunoda, F. Matsukura, and H. Ohno, "Tunnel magnetoresistance of 604% at 300 K by suppression of Ta diffusion in CoFeB/MgO/CoFeB pseudo-spin-valves annealed at high temperature," *Applied Physics Letters*, vol. 93, no. 8, p. 082508, 2008. (Cited on page 13.)

[38] E. Hall, "On a new action of the magnet on electric currents," *American Journal of Mathematics*, vol. 2, no. 3, pp. 287–292, 1879. (Cited on page 14.)

[39] E. H. Hall, "On the Rotational Coefficient in nickel and cobalt," *The London, Edinburgh, and Dublin Philosophical Magazine and Journal of Science*, vol. 12, no. 74, pp. 157–172, 1881. (Cited on page 14.)

[40] R. Karplus and J. Luttinger, "Hall effect in ferromagnetics," *Physical Review*, vol. 95, no. 5, p. 1154, 1954. (Cited on page 16.)

[41] Y. Yao, L. Kleinman, A. MacDonald, J. Sinova, T. Jungwirth, D.-s. Wang, E. Wang, and Q. Niu, "First principles calculation of anomalous Hall conductivity in ferromagnetic bcc Fe," *Physical review letters*, vol. 92, no. 3, p. 037204, 2004. (Cited on page 16.)

[42] A. Andreev, "The thermal conductivity of the intermediate state in superconductors," *Sov. Phys. JETP*, vol. 46, no. 5, pp. 1823–1828, 1964. (Cited on page 17.)

[43] G. Blonder, M. Tinkham, and T. Klapwijk, "Transition from metallic to tunneling regimes in superconducting microconstrictions: Excess current, charge imbalance, and supercurrent conversion," *Physical Review B*, vol. 25, no. 7, p. 4515, 1982. (Cited on page 17.)

[44] J. C. Slonczewski, "Current-driven excitation of magnetic multilayers," *Journal of Magnetism and Magnetic Materials*, vol. 159, no. 1-2, pp. L1–L7, 1996. (Cited on pages 20, 47, and 97.)

[45] L. Berger, "Emission of spin waves by a magnetic multilayer traversed by a current," *Physical Review B*, vol. 54, no. 13, p. 9353, 1996. (Cited on pages 20, 47, and 97.)

[46] J. Hirsch, "Spin Hall effect," *Physical review letters*, vol. 83, no. 9, p. 1834, 1999. (Cited on pages 22 and 98.)

[47] S. Zhang, "Spin Hall effect in the presence of spin diffusion," *Physical review letters*, vol. 85, no. 2, p. 393, 2000. (Cited on page 22.)

[48] Y. A. Bychkov and E. I. Rashba, "Oscillatory effects and the magnetic susceptibility of carriers in inversion layers," *Journal of physics C: Solid state physics*, vol. 17, no. 33, p. 6039, 1984. (Cited on page 22.)

[49] H. Van Leuken and R. De Groot, "Half-metallic antiferromagnets," *Physical review letters*, vol. 74, no. 7, p. 1171, 1995. (Cited on pages 23 and 48.)

[50] M. Žic, K. Rode, N. Thiyagarajah, Y. C. Lau, D. Betto, J. M. Coey, S. Sanvito, K. J. O'Shea, C. A. Ferguson, D. A. Maclaren, and T. Archer, "Designing a fully compensated half-metallic ferrimagnet," *Physical Review B*, vol. 93, no. 14, pp. 1–5, 2016. (Cited on pages 23 and 49.)

[51] R. Chwang, B. Smith, and C. Crowell, "Contact size effects on the Van der Pauw method for resistivity and Hall coefficient measurement," *Solid-State Electronics*, vol. 17, no. 12, pp. 1217–1227, 1974. (Cited on page 39.)

[52] A. Ramadan, R. Gould, and A. Ashour, "On the Van der Pauw method of resistivity measurements," *Thin solid films*, vol. 239, no. 2, pp. 272–275, 1994. (Cited on page 39.)

[53] M. N. Baibich, J. M. Broto, A. Fert, F. N. Van Dau, F. Petroff, P. Etienne, G. Creuzet, A. Friederich, and J. Chazelas, "Giant magnetoresistance of (001) Fe/(001) Cr magnetic superlattices," *Physical review letters*, vol. 61, no. 21, p. 2472, 1988. (Cited on page 47.)

[54] G. Binasch, P. Grünberg, F. Saurenbach, and W. Zinn, "Enhanced magnetoresistance in layered magnetic structures with antiferromagnetic interlayer exchange," *Physical review B*, vol. 39, no. 7, p. 4828, 1989. (Cited on page 47.)

[55] S. Tehrani, E. Chen, M. Durlam, M. DeHerrera, J. Slaughter, J. Shi, and G. Kerszykowski, "High density submicron magnetoresistive random access memory," *Journal of Applied Physics*, vol. 85, no. 8, pp. 5822–5827, 1999. (Cited on page 47.)

[56] Y. Huai, F. Albert, P. Nguyen, M. Pakala, and T. Valet, "Observation of spin-transfer switching in deep submicron-sized and low-resistance magnetic tunnel junctions," *Applied Physics Letters*, vol. 84, no. 16, pp. 3118–3120, 2004. (Cited on page 47.)

[57] I. M. Miron, K. Garello, G. Gaudin, P.-J. Zermatten, M. V. Costache, S. Auffret, S. Bandiera, B. Rodmacq, A. Schuhl, and P. Gambardella, "Perpendicular switching of a single ferromagnetic layer induced by in-plane current injection," *Nature*, vol. 476, no. 7359, pp. 189–193, 2011. (Cited on page 47.)

[58] L. Liu, C.-F. Pai, Y. Li, H. Tseng, D. Ralph, and R. Buhrman, “Spin-torque switching with the giant spin Hall effect of tantalum,” *Science*, vol. 336, no. 6081, pp. 555–558, 2012. (Cited on page 47.)

[59] J. C. Slater, “The ferromagnetism of nickel,” *Physical Review*, vol. 49, no. 7, p. 537, 1936. (Cited on page 47.)

[60] L. Pauling, “The nature of the chemical bond. II. The one-electron bond and the three-electron bond,” *Journal of the American Chemical Society*, vol. 53, no. 9, pp. 3225–3237, 1931. (Cited on page 47.)

[61] K. Özdoğan and I. Galanakis, “Effect of order on the half-metallic gap in Heusler compounds,” 2011. (Cited on page 47.)

[62] P. Mavropoulos, I. Galanakis, V. Popescu, and P. Dederichs, “The influence of spin–orbit coupling on the band gap of Heusler alloys,” *Journal of Physics: Condensed Matter*, vol. 16, no. 48, p. S5759, 2004. (Cited on page 47.)

[63] M. Katsnelson, V. Y. Irkhin, L. Chioncel, A. Lichtenstein, and R. A. de Groot, “Half-metallic ferromagnets: From band structure to many-body effects,” *Reviews of Modern Physics*, vol. 80, no. 2, p. 315, 2008. (Cited on page 47.)

[64] I. Tutic, J. Herran, B. Staten, P. Gray, T. R. Paudel, A. Sokolov, E. Y. Tsymbal, and P. V. Lukashev, “Effects of pressure and strain on spin polarization of IrMnSb,” *Journal of Physics: Condensed Matter*, vol. 29, no. 7, p. 075801, 2016. (Cited on page 48.)

[65] S. Ishida, S. Akazawa, Y. Kubo, and J. Ishida, “Band theory of Co_2MnSn, Co_2TiSn and Co_2TiAl,” *Journal of Physics F: Metal Physics*, vol. 12, no. 6, p. 1111, 1982. (Cited on page 48.)

[66] J. Kübler, “First principle theory of metallic magnetism,” *Physica B+ C*, vol. 127, no. 1-3, pp. 257–263, 1984. (Cited on page 48.)

[67] K.-I. Kobayashi, T. Kimura, H. Sawada, K. Terakura, and Y. Tokura, “Room-temperature magnetoresistance in an oxide material with an ordered double-perovskite structure,” *Nature*, vol. 395, no. 6703, pp. 677–680, 1998. (Cited on page 48.)

[68] A. Yanase and K. Siratori, “Band structure in the high temperature phase of Fe_3O_4,” *Journal of the Physical Society of Japan*, vol. 53, no. 1, pp. 312–317, 1984. (Cited on page 48.)

[69] Y. Ji, G. Strijkers, F. Yang, C. Chien, J. Byers, A. Anguelouch, G. Xiao, and A. Gupta, “Determination of the spin polarization of half-metallic CrO_2 by point contact Andreev reflection,” *Physical Review Letters*, vol. 86, no. 24, p. 5585, 2001. (Cited on page 48.)

[70] R. Cheng, B. Xu, C. Borca, A. Sokolov, C.-S. Yang, L. Yuan, S.-H. Liou, B. Doudin, and P. A. Dowben, “Characterization of the native Cr_2O_3 oxide surface of CrO_2,” *Applied Physics Letters*, vol. 79, no. 19, pp. 3122–3124, 2001. (Cited on page 48.)

[71] J. Coey and M. Venkatesan, “Half-metallic ferromagnetism: Example of CrO_2,” *Journal of Applied Physics*, vol. 91, no. 10, pp. 8345–8350, 2002. (Cited on page 48.)

[72] X. Hu, “Half-metallic antiferromagnet as a prospective material for spintronics,” 2012. (Cited on page 48.)

[73] W. E. Pickett, “Spin-density-functional-based search for half-metallic antiferromagnets,” *Physical review B*, vol. 57, no. 17, p. 10613, 1998. (Cited on page 48.)

[74] V. Pardo and W. E. Pickett, “Compensated magnetism by design in double perovskite oxides,” *Physical Review B*, vol. 80, no. 5, p. 054415, 2009. (Cited on page 48.)

[75] D. Betto, K. Rode, N. Thiyagarajah, Y. C. Lau, K. Borisov, G. Atcheson, M. Ic, T. Archer, P. Stamenov, and J. M. Coey, “The zero-moment half metal: How could it change spin electronics?,” *AIP Advances*, vol. 6, no. 5, 2016. (Cited on pages 51, 65, and 66.)

[76] C. Fowley, K. Rode, Y.-C. Lau, N. Thiyagarajah, D. Betto, K. Borisov, G. Atcheson, E. Kampert, Z. Wang, Y. Yuan, S. Zhou, J. Lindner, P. Stamenov, J. M. D. Coey, and A. M. Deac, “Magnetocrystalline anisotropy and

exchange probed by high-field anomalous Hall effect in fully compensated half-metallic $\mathrm{Mn_2Ru_xGa}$ thin films," *Phys. Rev. B*, vol. 98, p. 220406, Dec 2018. (Cited on pages 51, 54, 55, 65, 66, and 110.)

[77] C. Banerjee, N. Teichert, K. Siewierska, Z. Gercsi, G. Atcheson, P. Stamenov, K. Rode, J. Coey, and J. Besbas, "Single pulse all-optical toggle switching of magnetization without gadolinium in the ferrimagnet $\mathrm{Mn_2Ru_xGa}$," *Nature communications*, vol. 11, no. 1, pp. 1–6, 2020. (Cited on page 51.)

[78] K. Siewierska, G. Atcheson, A. Jha, K. Esien, R. Smith, S. Lenne, N. Teichert, J. O'Brien, J. Coey, P. Stamenov, *et al.*, "Magnetic order and magnetotransport in half-metallic ferrimagnetic $\mathrm{Mn_yRu_xGa}$ thin films," *Physical Review B*, vol. 104, no. 6, p. 064414, 2021. (Cited on pages 52 and 57.)

[79] K. Borisov, D. Betto, Y.-C. Lau, C. Fowley, A. Titova, N. Thiyagarajah, G. Atcheson, J. Lindner, A. Deac, J. Coey, *et al.*, "Tunnelling magnetoresistance of the half-metallic compensated ferrimagnet $\mathrm{Mn_2Ru_xGa}$," *Applied Physics Letters*, vol. 108, no. 19, p. 192407, 2016. (Cited on pages 54 and 113.)

[80] R. E. Troncoso, K. Rode, P. Stamenov, J. M. D. Coey, and A. Brataas, "Antiferromagnetic single-layer spin-orbit torque oscillators," *Physical Review B*, vol. 99, no. 5, p. 054433, 2019. (Cited on page 65.)

[81] N. Awari, S. Kovalev, C. Fowley, K. Rode, R. A. Gallardo, Y. C. Lau, D. Betto, N. Thiyagarajah, B. Green, O. Yildirim, J. Lindner, J. Fassbender, J. M. Coey, A. M. Deac, and M. Gensch, "Narrow-band tunable terahertz emission from ferrimagnetic $\mathrm{Mn_{3-x}Ga}$ thin films," *Applied Physics Letters*, vol. 109, no. 3, 2016. (Cited on page 65.)

[82] X. Fan, D. Xue, C. Jiang, Y. Gong, and J. Li, "An approach for researching uniaxial anisotropy magnet: Rotational magnetization," *Journal of Applied Physics*, vol. 102, no. 12, p. 123901, 2007. (Cited on page 65.)

[83] Y. Endo, O. Kitakami, S. Okamoto, and Y. Shimada, "Determination of first and second magnetic anisotropy constants of magnetic recording media," *Applied Physics Letters*, vol. 77, no. 11, pp. 1689–1691, 2000. (Cited on page 65.)

[84] E. A. Jagla, "Hysteresis loops of magnetic thin films with perpendicular anisotropy," *Physical Review B*, vol. 72, no. 9, p. 094406, 2005. (Cited on page 65.)

[85] K. Okamoto, "A new method for analysis of magnetic anisotropy in films using the spontaneous Hall effect," *Journal of magnetism and magnetic materials*, vol. 35, no. 1-3, pp. 353–355, 1983. (Cited on page 65.)

[86] H. Sato, M. Pathak, D. Mazumdar, X. Zhang, G. Mankey, P. LeClair, and A. Gupta, "Anomalous Hall effect behavior in (100) and (110) CrO_2 thin films," *Journal of Applied Physics*, vol. 109, no. 10, p. 103907, 2011. (Cited on page 65.)

[87] G. Suran, M. Naili, H. Niedoba, F. Machizaud, O. Acher, and D. Pain, "Magnetic and structural properties of Co-rich CoFeZr amorphous thin films," *Journal of magnetism and magnetic materials*, vol. 192, no. 3, pp. 443–457, 1999. (Cited on page 65.)

[88] D. Berling, S. Zabrocki, R. Stephan, G. Garreau, J. Bubendorff, A. Mehdaoui, D. Bolmont, P. Wetzel, C. Pirri, and G. Gewinner, "Accurate measurement of the in-plane magnetic anisotropy energy function E_a (θ) in ultrathin films by magneto-optics," *Journal of magnetism and magnetic materials*, vol. 297, no. 2, pp. 118–140, 2006. (Cited on page 65.)

[89] R. Cowburn, A. Ercole, S. Gray, and J. Bland, "A new technique for measuring magnetic anisotropies in thin and ultrathin films by magneto-optics," *Journal of applied physics*, vol. 81, no. 10, pp. 6879–6883, 1997. (Cited on page 65.)

[90] F. Preisach, "Über die magnetische Nachwirkung," *Zeitschrift für physik*, vol. 94, no. 5-6, pp. 277–302, 1935. (Cited on page 68.)

[91] C. Pike, "First-order reversal-curve diagrams and reversible magnetization," *Physical Review B*, vol. 68, no. 10, p. 104424, 2003. (Cited on page 69.)

[92] T. Sorop, C. Untiedt, F. Luis, M. Kröll, M. Raşa, and L. De Jongh, "Magnetization reversal of ferromagnetic nanowires studied by magnetic force mi-

croscopy," *Physical Review B*, vol. 67, no. 1, p. 014402, 2003. (Cited on page 69.)

[93] A. P. Roberts, T. P. Almeida, N. S. Church, R. J. Harrison, D. Heslop, Y. Li, J. Li, A. R. Muxworthy, W. Williams, and X. Zhao, "Resolving the origin of pseudo-single domain magnetic behavior," *Journal of Geophysical Research: Solid Earth*, vol. 122, no. 12, pp. 9534–9558, 2017. (Cited on page 70.)

[94] F. Groß, S. E. Ilse, G. Schütz, J. Gräfe, and E. Goering, "Interpreting first-order reversal curves beyond the Preisach model: An experimental permalloy microarray investigation," *Physical Review B*, vol. 99, no. 6, p. 064401, 2019. (Cited on page 70.)

[95] I. D. Mayergoyz and G. Friedman, "Generalized Preisach model of hysteresis," *IEEE transactions on Magnetics*, vol. 24, no. 1, pp. 212–217, 1988. (Cited on pages 72 and 114.)

[96] E. Della Torre, "Magnetization calculation of fine particles," *IEEE Transactions on Magnetics*, vol. 22, no. 5, pp. 484–489, 1986. (Cited on page 72.)

[97] Y. D. Yan and E. D. Torre, "Particle interaction in numerical micromagnetic modeling," *Journal of applied physics*, vol. 67, no. 9, pp. 5370–5372, 1990. (Cited on page 72.)

[98] G. Kádár, E. Kisdi-Koszo, L. Kiss, L. Potocky, M. Zatroch, and E. Della Torre, "Bilinear product Preisach modeling of magnetic hysteresis curves," *IEEE Transactions on Magnetics*, vol. 25, no. 5, pp. 3931–3933, 1989. (Cited on page 72.)

[99] J. Fuzi, "Analytical approximation of Preisach distribution functions," *IEEE transactions on magnetics*, vol. 39, no. 3, pp. 1357–1360, 2003. (Cited on page 72.)

[100] O. Henze and W. M. Rucker, "Identification procedures of Preisach model," *IEEE Transactions on magnetics*, vol. 38, no. 2, pp. 833–836, 2002. (Cited on page 72.)

[101] W. S. Galinaitis, D. S. Joseph, and R. C. Rogers, “Parameter identification for Preisach models of hysteresis,” in *International Design Engineering Technical Conferences and Computers and Information in Engineering Conference*, vol. 80289, pp. 1409–1417, American Society of Mechanical Engineers, 2001. (Cited on page 72.)

[102] I. Mayergoyz, “Mathematical models of hysteresis,” *IEEE Transactions on magnetics*, vol. 22, no. 5, pp. 603–608, 1986. (Cited on pages 72, 73, 76, and 114.)

[103] G. Bertotti, *Hysteresis in magnetism: for physicists, materials scientists, and engineers.* Gulf Professional Publishing, 1998. (Cited on page 73.)

[104] I. D. Mayergoyz, *Mathematical models of hysteresis and their applications.* Academic Press, 2003. (Cited on page 73.)

[105] H. Chiriac, N. Lupu, L. Stoleriu, P. Postolache, and A. Stancu, “Experimental and micromagnetic first-order reversal curves analysis in NdFeB-based bulk “exchange spring”-type permanent magnets,” *Journal of magnetism and magnetic materials*, vol. 316, no. 2, pp. 177–180, 2007. (Cited on page 73.)

[106] P.-A. Chen, C.-Y. Yang, S.-J. Chang, M.-H. Lee, N.-K. Tang, S.-C. Yen, and Y.-C. Tseng, “Soft and hard natures of $Nd_2Fe_{14}B$ permanent magnet explored by first-order-reversal-curves,” *Journal of magnetism and magnetic materials*, vol. 370, pp. 45–53, 2014. (Cited on page 73.)

[107] A. P. Roberts, C. R. Pike, and K. L. Verosub, “First-order reversal curve diagrams: A new tool for characterizing the magnetic properties of natural samples,” *Journal of Geophysical Research: Solid Earth*, vol. 105, no. B12, pp. 28461–28475, 2000. (Cited on page 73.)

[108] A. R. Muxworthy and A. P. Roberts, “First-order reversal curve (FORC) diagrams,” 2007. (Cited on page 73.)

[109] F. Béron, L. Clime, M. Ciureanu, D. Ménard, R. W. Cochrane, and A. Yelon, “First-order reversal curves diagrams of ferromagnetic soft nanowire arrays,”

IEEE transactions on magnetics, vol. 42, no. 10, pp. 3060–3062, 2006. (Cited on page 73.)

[110] F. Béron, L.-P. Carignan, D. Ménard, and A. Yelon, “Magnetic behavior of Ni/Cu multilayer nanowire arrays studied by first-order reversal curve diagrams,” *IEEE Transactions on Magnetics*, vol. 44, no. 11, pp. 2745–2748, 2008. (Cited on page 73.)

[111] C. R. Pike, A. P. Roberts, and K. L. Verosub, “Characterizing interactions in fine magnetic particle systems using first order reversal curves,” *Journal of Applied Physics*, vol. 85, no. 9, pp. 6660–6667, 1999. (Cited on page 73.)

[112] A. Stancu, D. Ricinschi, L. Mitoseriu, P. Postolache, and M. Okuyama, “First-order reversal curves diagrams for the characterization of ferroelectric switching,” *Applied Physics Letters*, vol. 83, no. 18, pp. 3767–3769, 2003. (Cited on page 73.)

[113] J.-G. Ramírez, A. Sharoni, Y. Dubi, M. Gómez, and I. K. Schuller, “First-order reversal curve measurements of the metal-insulator transition in VO_2: Signatures of persistent metallic domains,” *Physical Review B*, vol. 79, no. 23, p. 235110, 2009. (Cited on page 73.)

[114] N. Teichert, G. Atcheson, K. Siewierska, M. N. Sanz-Ortiz, M. Venkatesan, K. Rode, S. Felton, P. Stamenov, and J. Coey, “Magnetic reversal and pinning in a perpendicular zero-moment half-metal,” *Physical Review Materials*, vol. 5, no. 3, p. 034408, 2021. (Cited on pages 76 and 78.)

[115] E. C. Stoner and E. Wohlfarth, “A mechanism of magnetic hysteresis in heterogeneous alloys,” *Philosophical Transactions of the Royal Society of London. Series A, Mathematical and Physical Sciences*, vol. 240, no. 826, pp. 599–642, 1948. (Cited on page 78.)

[116] S. Wolf, D. Awschalom, R. Buhrman, J. Daughton, v. S. von Molnár, M. Roukes, A. Y. Chtchelkanova, and D. Treger, “Spintronics: a spin-based electronics vision for the future,” *science*, vol. 294, no. 5546, pp. 1488–1495, 2001. (Cited on page 97.)

[117] A. D. Kent and D. C. Worledge, “A new spin on magnetic memories,” *Nature nanotechnology*, vol. 10, no. 3, pp. 187–191, 2015. (Cited on page 97.)

[118] A. Manchon, J. Železnỳ, I. M. Miron, T. Jungwirth, J. Sinova, A. Thiaville, K. Garello, and P. Gambardella, “Current-induced spin-orbit torques in ferromagnetic and antiferromagnetic systems,” *Reviews of Modern Physics*, vol. 91, no. 3, p. 035004, 2019. (Cited on page 98.)

[119] M. Cubukcu, O. Boulle, N. Mikuszeit, C. Hamelin, T. Brächer, N. Lamard, M.-C. Cyrille, L. Buda-Prejbeanu, K. Garello, I. M. Miron, *et al.*, “Ultra-fast perpendicular spin–orbit torque MRAM,” *IEEE Transactions on Magnetics*, vol. 54, no. 4, pp. 1–4, 2018. (Cited on page 98.)

[120] V. M. Edelstein, “Spin polarization of conduction electrons induced by electric current in two-dimensional asymmetric electron systems,” *Solid State Communications*, vol. 73, no. 3, pp. 233–235, 1990. (Cited on page 98.)

[121] K. Ando, S. Takahashi, K. Harii, K. Sasage, J. Ieda, S. Maekawa, and E. Saitoh, “Electric manipulation of spin relaxation using the spin Hall effect,” *Physical review letters*, vol. 101, no. 3, p. 036601, 2008. (Cited on page 98.)

[122] A. Chernyshov, M. Overby, X. Liu, J. K. Furdyna, Y. Lyanda-Geller, and L. P. Rokhinson, “Evidence for reversible control of magnetization in a ferromagnetic material by means of spin-orbit magnetic field,” *Nature Physics*, vol. 5, no. 9, pp. 656–659, 2009. (Cited on page 98.)

[123] C. Ciccarelli, L. Anderson, V. Tshitoyan, A. Ferguson, F. Gerhard, C. Gould, L. Molenkamp, J. Gayles, J. Železnỳ, L. Šmejkal, *et al.*, “Room-temperature spin–orbit torque in NiMnSb,” *Nature physics*, vol. 12, no. 9, pp. 855–860, 2016. (Cited on page 98.)

[124] J. Železnỳ, H. Gao, K. Vỳbornỳ, J. Zemen, J. Mašek, A. Manchon, J. Wunderlich, J. Sinova, and T. Jungwirth, “Relativistic Néel-order fields induced by electrical current in antiferromagnets,” *Physical review letters*, vol. 113, no. 15, p. 157201, 2014. (Cited on pages 98 and 104.)

[125] J. Železnỳ, H. Gao, A. Manchon, F. Freimuth, Y. Mokrousov, J. Zemen, J. Mašek, J. Sinova, and T. Jungwirth, "Spin-orbit torques in locally and globally noncentrosymmetric crystals: Antiferromagnets and ferromagnets," *Physical Review B*, vol. 95, no. 1, p. 014403, 2017. (Cited on pages 98 and 104.)

[126] S. Y. Bodnar, L. Šmejkal, I. Turek, T. Jungwirth, O. Gomonay, J. Sinova, A. Sapozhnik, H.-J. Elmers, M. Kläui, and M. Jourdan, "Writing and reading antiferromagnetic Mn_2Au by Néel spin-orbit torques and large anisotropic magnetoresistance," *Nature communications*, vol. 9, no. 1, pp. 1–7, 2018. (Cited on pages 99 and 100.)

[127] P. Wadley, B. Howells, J. Železnỳ, C. Andrews, V. Hills, R. P. Campion, V. Novák, K. Olejník, F. Maccherozzi, S. Dhesi, *et al.*, "Electrical switching of an antiferromagnet," *Science*, vol. 351, no. 6273, pp. 587–590, 2016. (Cited on pages 99 and 100.)

[128] M. Grzybowski, P. Wadley, K. Edmonds, R. Beardsley, V. Hills, R. Campion, B. Gallagher, J. S. Chauhan, V. Novak, T. Jungwirth, *et al.*, "Imaging current-induced switching of antiferromagnetic domains in CuMnAs," *Physical review letters*, vol. 118, no. 5, p. 057701, 2017. (Cited on page 99.)

[129] S. Y. Bodnar, M. Filianina, S. Bommanaboyena, T. Forrest, F. Maccherozzi, A. Sapozhnik, Y. Skourski, M. Kläui, and M. Jourdan, "Imaging of current induced Néel vector switching in antiferromagnetic Mn_2Au," *Physical Review B*, vol. 99, no. 14, p. 140409, 2019. (Cited on page 99.)

[130] K. Buschow, "Magnetic properties of amorphous rare-earth-cobalt alloys," *Journal of Applied Physics*, vol. 51, no. 5, pp. 2795–2798, 1980. (Cited on page 99.)

[131] N. Roschewsky, T. Matsumura, S. Cheema, F. Hellman, T. Kato, S. Iwata, and S. Salahuddin, "Spin-orbit torques in ferrimagnetic GdFeCo alloys," *Applied Physics Letters*, vol. 109, no. 11, p. 112403, 2016. (Cited on page 99.)

[132] S. Mizukami, D. Watanabe, M. Oogane, Y. Ando, Y. Miura, M. Shirai, and T. Miyazaki, "Low damping constant for Co_2FeAl Heusler alloy films and its

correlation with density of states," *Journal of Applied Physics*, vol. 105, no. 7, p. 07D306, 2009. (Cited on page 99.)

[133] D.-H. Kim, T. Okuno, S. K. Kim, S.-H. Oh, T. Nishimura, Y. Hirata, Y. Futakawa, H. Yoshikawa, A. Tsukamoto, Y. Tserkovnyak, *et al.*, "Low magnetic damping of ferrimagnetic GdFeCo alloys," *Physical review letters*, vol. 122, no. 12, p. 127203, 2019. (Cited on page 99.)

[134] T. Kubota, S. Tsunegi, M. Oogane, S. Mizukami, T. Miyazaki, H. Naganuma, and Y. Ando, "Half-metallicity and Gilbert damping constant in $Co_2Fe_xMn_{1-x}Si$ Heusler alloys depending on the film composition," *Applied Physics Letters*, vol. 94, no. 12, p. 122504, 2009. (Cited on page 99.)